Biophysical Symptoms of Cellular Stress

Doctoral thesis

Sakshi Sareen

Institute of Physical Chemistry, Polish Academy of Sciences

Department of Condensed Soft Matter,

Supervisor: **Prof. Robert Holyst**

Auxiliary supervisor: **Dr. Karina Kwapiszewska**

March, 2025

This work was supported by

the National science centre, Poland, within the grant *OPUS UMO-2019/33/B/ST4/00557*

And by the polish national agency for academic exchange,

and Genetics division, Department of Medicine at Brigham and Women's Hospital and Harvard Medical School.

Publications

1. Sareen, S., Zgorzelska, A., Kwapiszewska, K., & Holyst, R. (2024). Starvation induces diffusion hindrance at nanoscale in mammalian cells. *Nanoscale*, 0–14. https://doi.org/10.1039/D4NR03620D. ***Published.***

2. Sareen, S., Wiśniewska, A., Kwapiszewska, K., & Hołyst, R. (2023). Comment on "Fluorimetric sensing of ATP in water by an imidazolium hydrazone based sensor" by S. Farshbaf and P. Anzenbacher Jr., *Chem. Commun.* , 2019, **55** , 1770. *Chemical Communications*, *59*(35), 5293–5295. https://doi.org/10.1039/D3CC00175J. ***Published.***

3. Sareen, S., Asztemborska A., Nicinski, K., Kwapiszewska, K., & Holyst, R. (2025). Autofluorescence response in cancer cells during cell death. *RedoxBiology*. *Under preparation.*

4. Sareen, S., Cann, P., Kwapiszewska, Sherwood, R., & Holyst, R. (2025). Changes in biophysical properties of CRISPR edited cancer cells. *Under preparation.*

Other Publications

5. Sareen, S., Kijewska, A., Kwapiszewska, K., & Holyst, R. (2023). Nanoviscosity: a physical marker in starvation-induced cancer cells. *Single Molecule Spectroscopy and Superresolution Imaging XVI* (p. 18). SPIE. https://doi.org/10.1117/12.2649844. ***Published.***

Acknowledgments

कर्मण्येवाधिकारस्ते मा फलेषु कदाचन।
मा कर्मफलहेतुर्भूर्मा ते सङ्गोऽस्त्वकर्मणि।

- भगवद गीता

I owe a huge thanks to so many wonderful people who have stood by me through this rollercoaster of scientific rigor and discovery.

My sincere thanks goes to **Prof. Robert Hołyst** for being my scientific mentor and guide throughout multiple projects.

I am immensely grateful to **Dr. Karina Kwapiszewska**, whose availability for insightful discussions and troubleshooting has been a lifeline. But most importantly, her constant presence kept me grounded and sane throughout this journey.

My gratitude goes out to **Prof. Richard Sherwood**, for accepting me as a visiting scholar in his lab in Boston and for teaching me the valuable art of gene editing.

This thesis would not be complete without the never ending support of my family – my mother **Monika Sareen**, my father **Raman Kumar Sareen** and my brother **Aman Sareen**.

I would also like to acknowledge my friends for all those late night pep talks, laughter and emotional support – **Srishty Sharma**, **Shreyas Kandhai Vasantham**, **Faria Khan**, **Ahmad Makkawi**, **Patrick Cann**, **Karthika Kappalakandy Valapil** and **Debjita Mukherjee**.

I thank all the members of group **Soft Matter, Team 10**, for creating a cordial working environment.

Lastly, I am truly grateful for the opportunity to work alongside such talented and curious groups of people. This experience has been inspiring and life-shaping.

Abstract

The intracellular molecular organisation is of utmost importance for a eukaryotic cell to stay alive. This organisation leads to the formation of a complex fluid called cell cytoplasm, where major biochemical processes occur. This drives functions like cell growth, division, and movement. Stress causes disturbances in the intracellular organisation. Cell survival during stress relies on changes in physical and biological properties. These changes in the complex, crowded fluid reveal important information about regulating major cellular processes and their role in cell survival. Limited information is available on biophysical processes during cellular stress. Fluorescence-based methods such as Fluorescence correlation spectroscopy (FCS) and Fluorescence lifetime imaging (FLIM) are excellent at measuring the diffusion dynamics, molecular interactions, and fluorescence lifetimes of solutes in low concentrations (<1 μM) and small volumes (<1 μl), making them ideal analytical tools for this study.

Stress affects every organism on the planet in different forms. Whether it's nutrient limitations, changes in oxidation/reduction states, increases in cytotoxic molecules, or changes in water content. The ways are unlimited. I picked two stress factors that affect all the organisms, irrespective of their size or complexity – cellular starvation and mitochondrial stress. I studied the effects of external stress on the biophysical properties of cancer cells. This thesis will describe a crucial survival technique employed by every living species on the planet – Stress-responsive behaviour.

In the **cellular starvation** chapter, I identify trends in intracellular molecular crowding and water efflux from cell cytoplasm and nucleus during prolonged starvation. FCS measurements reveal the effects of molecular crowding on green fluorescent protein (GFP) and define the changes in movement by measuring its diffusion coefficients. Without this intracellular motion/transport of molecules from one place to another, cells can't function. The chapter highlights some key points, such as compartmentalised cellular response to starvation stress, explicitly focusing on alterations in diffusion coefficients and energy conservation mechanisms. As an extension of these results, the effects of gene knockout of an anion channel are explored on diffusion of GFP and cell volume homeostasis in HeLa knockout cells. The gene knockout was created using CRISPR-CAS9 gene editing tools, and FCS was used to study intracellular diffusion.

In the **cellular autofluorescence** chapter, cell response to “induced cell death” via mitochondrial stress is measured. Measuring these changes is important to understanding cell response to stress before cell death. Using FLIM, FCS, and HPLC, I focus on the enhanced autofluorescence response of cancer cells to the apoptosis-inducing drug - staurosporine at two different concentrations.

The cellular ATP depletion chapter describes the limitations of ATP sensors, with a significant focus on a newly discovered chemical ATP sensor. Since starvation was a necessary stress factor in this study, alteration in ATP levels was considered as an interlinked phenomenon.

Streszczenie

Wewnątrzkomórkowa organizacja molekularna ma kluczowe znaczenie dla przetrwania komórki eukariotycznej. Przykładem jest cytoplazma komórkowa – płyn złożony, w którym zachodzą główne procesy biochemiczne, warunkujące funkcje takie jak wzrost komórki, podział i ruch. Czynniki stresowe powodują zakłócenia w organizacji wewnątrzkomórkowej, a przetrwanie komórki w czasie stresu zależy od zmian w jej właściwościach fizycznych i biologicznych. Poznanie zmian indukowanych stresem w złożonym, zatłoczonym płynie ujawnić może istotne informacje na temat regulacji głównych procesów komórkowych i ich roli w przetrwaniu komórki. Jednakże istnieje ograniczona liczba informacji na temat procesów biofizycznych w czasie stresu komórkowego. Metody oparte na fluorescencji, takie jak spektroskopia korelacji fluorescencji (ang. *fluorescence correlation spectroscopy*, FCS) i obrazowanie czasów życia fluorescencji (ang. *fluorescence lifetime imagind microscopy*, FLIM), są doskonałe do mierzenia dyfuzji, interakcji molekularnych oraz czasów życia fluorescencji rozpuszczalników w niskich stężeniach (<1 μM) i małych objętościach (<1 μl), co czyni je idealnymi narzędziami analitycznymi do tego badania.

Stres jest nieodłącznym elementem towarzyszącym organizmom żywym. Niezależnie od tego, czy chodzi o ograniczenia w dostępności składników odżywczych, zmiany w stanach utleniania/redukcji, wzrost stężenia cząsteczek cytotoksycznych, czy zmiany w zawartości wody – formy stresu są nieograniczone. Wybrałam dwa czynniki stresowe, które wpływają na wszystkie organizmy, bez względu na ich wielkość czy złożoność – głodzenie komórek i stres mitochondrialny. Badałam wpływ zewnętrznego stresu na właściwości biofizyczne komórek rakowych. Ta praca opisuje kluczową technikę przetrwania, stosowaną przez wszystkie żywe gatunki na Ziemi – zachowanie w odpowiedzi na stres.

W rozdziale dotyczącym głodzenia komórek identyfikuję tendencje w wewnątrzkomórkowym zatłoczeniu molekularnym oraz wypływie wody z cytoplazmy i jądra komórkowego podczas przedłużonego braku dostępu do składników odżywczych. Pomiar FCS ujawnia wpływ zatłoczenia molekularnego na zmiany współczynników dyfuzji białka zielonej fluorescencji (ang. *green fluorescence protein*, GFP). Bez tego wewnątrzkomórkowego ruchu/transportu cząsteczek z jednego miejsca na drugie komórki nie mogą funkcjonować. W rozdziale podkreślono kluczowe punkty, takie jak odpowiedź komórki na stres głodowy w ujęciu kompartmentalnym, koncentrując się na zmianach współczynników dyfuzji i mechanizmach

oszczędzania energii. Jako rozszerzenie tych wyników, badane są efekty wyciszenia (ang. *knock-out*) genu kanału anionowego na dyfuzję GFP i homeostazę objętości komórki w komórkach HeLa. *Knock-out* genu został stworzony przy użyciu narzędzi edycji genów CRISPR-CAS9, a FCS zostało użyte do badania dyfuzji wewnątrzkomórkowej.

W rozdziale dotyczącym autofluorescencji komórkowej, mierzona jest odpowiedź komórki na „indukowaną śmierć komórkową" przez stres mitochondrialny. Mierzenie tych zmian jest istotne dla zrozumienia reakcji komórki na stres przed jej śmiercią. Przy użyciu FLIM, FCS i HPLC (ang. *high pressure liquid chromatography*), koncentruję się na wzmożonej autofluorescencji komórek rakowych na lek indukujący apoptozę - staurosporynę w dwóch różnych stężeniach.

Rozdział dotyczący deplecji ATP w komórce opisuje ograniczenia czujników ATP, z dużym naciskiem na nowo odkryty chemiczny czujnik ATP. Ponieważ głodowanie było koniecznym czynnikiem stresowym w tym badaniu, zmiany w poziomach ATP zostały uwzględnione jako zjawisko wzajemnie powiązane.

Table of Contents

1 Introduction 1
1.1 What is cellular stress. Why is it important? 1
1.1.1 Cellular starvation 2
1.1.2 Mitochondrial stress-induced cell death 5
1.2 Biophysical properties of cells 6
1.2.1 Macromolecular crowding 6
1.2.2 Diffusion and Viscosity 7
1.2.3 Autofluorescence 8
1.3 Methods to Study Cellular Biophysics 10
1.3.1 Fluorescence microscopy 10
1.3.2 ATP detection 15
1.3.3 CRISPR/Cas9 gene editing 18
1.4 Summary 20
2 Results 22
2.1 Cellular Starvation 22
2.1.1 Movement at nanoscale in cells 22
2.1.2 Measuring diffusion in HeLa cell cytoplasm 23
2.1.3 Measuring diffusion in HeLa cell nucleus 27
2.1.4 Volume changes during cellular starvation 30
2.1.5 Decrease in intramolecular crowder space in HeLa cells during starvation 32
2.1.6 Changes in interaction parameter 33
2.1.7 Morphological changes in 769-P cells during starvation 35
2.1.8 Cell re-growth in media after prolonged starvation 36
2.1.9 Conclusion 38
2.2 Cellular nanoviscosity in CLCNKA knockout cells 39
2.3 CLCNKA gene knockout 39
2.3.1 Knockout cell preparation and confirmation 39
2.3.2 Diffusion measurements during starvation in knockout HeLa cell cytoplasm 41
2.3.3 Volume homeostasis in $HeLa_{ko}$ cells during prolonged starvation 44
2.3.4 Conclusion 45
2.4 Cellular ATP depletion 45
2.4.1 Types of ATP sensors 45
2.4.2 Capabilities and limitations of genetic ATP sensors 46

2.4.3 Bisantrene as ATP sensor 47
2.4.4 Bisantrene-ATP interaction studies using TCSPC 48
2.4.5 Polarisation Results.....50
2.4.6 Spectroscopy results.....51
2.4.7 Intracellular behaviour of Bisantrene.....52
2.4.8 Conclusion 54
2.5 Cellular autofluorescence.....54
2.5.1 Increased autofluorescence as a response to Staurosporine-induced cell stress 54
2.5.2 Confocal imaging of different cancer cell lines during STS treatment 55
2.5.3 Cell viability after STS treatment 58
2.5.4 Fluorescence of Staurosporine.....59
2.5.5 Autofluorescence in heat inactivated cells.....61
2.5.6 HPLC analysis 63
2.5.7 Fluorescence lifetime analysis 65
2.5.8 Fluorescence lifetime imaging of mammalian cells 66
2.5.9 Conclusion 70
3 Summary and Conclusions 72

References

Appendix

A. List of abbreviations…….....A
B. Experimental procedures……B
B.1. Cell culture……1.1
B.2. FCS and confocal measurements……..1.2
B.3. Isolating plasmid F_0-F_1 ATPase (MALIONR) from *E.coli*……..1.2
B.4. Gel electrophoresis and MALIONR transfection in 769-p cells……..1.3
B.5. CRISPR-CAS9 gene editing protocol for creating cellular knockout…….....1.4
B.6. Bisantrene-ATP concentrations in TCSPC experimental set up……..1.5
B.7. HPLC experimental set up…….……..1.6
B.8. FLIM experimental set up for data acquisition……1.7

1 Introduction

1.1 What is cellular stress. Why is it important?

Cellular stress refers to anything that disrupts a system's normal functioning/conditioning, i.e., it disrupts cell viability or fitness. However, what stress encompasses is not very easily defined by these definitions. A study published in 2018 describes stress to be the most basic feature of all biological systems[1]. Cells are under constant stress, and cellular and molecular responses are required to balance stressful and un-stressful conditions. This can also be considered analogous to the dynamicity of the cellular systems, maintaining equilibrium constants via diffusion of particles of different sizes. The capacity to maintain the internal cellular processes remains prevalent in all organisms, irrespective of their size, from the smallest organism to the largest.

Stress mitigation in organisms is linked with survival. For example, warm-blooded hibernators like bears, dwarf lemurs, hamsters, and ground squirrels undergo core body temperature adjustments, decreased metabolic rates, and energy-consuming processes to ride the harsh periods of winter stress[2]. Stress response synonymous with this has been reported in other animals, too, including insects, birds, fish and mollusks[2]. Studying stress response is crucial for understanding growth and division in all organisms. In a mammalian cell, the smallest living building block of life, localised behavioural changes to stress have been observed.

Mammalian cells are continuously responding to external or internal stress at molecular levels. Cellular response to stress plays a vital role in various pathologies. Cancer is no exception. It has been studied how cancer development and progression are majorly linked with the ability of cancer cells to respond to stress stimuli. For example, cancer stem cells are known to have extremely high-stress tolerance, which makes them resistant to a range of treatment options[3]. Understanding these stress responses, thus, becomes crucial in designing therapies and treatments. Cells experience various types of stress. Stress affects biophysical properties in cells (Fig 1). In this thesis, I studied;

- Cellular starvation
- Mitochondrial stress (due to staurosporine)

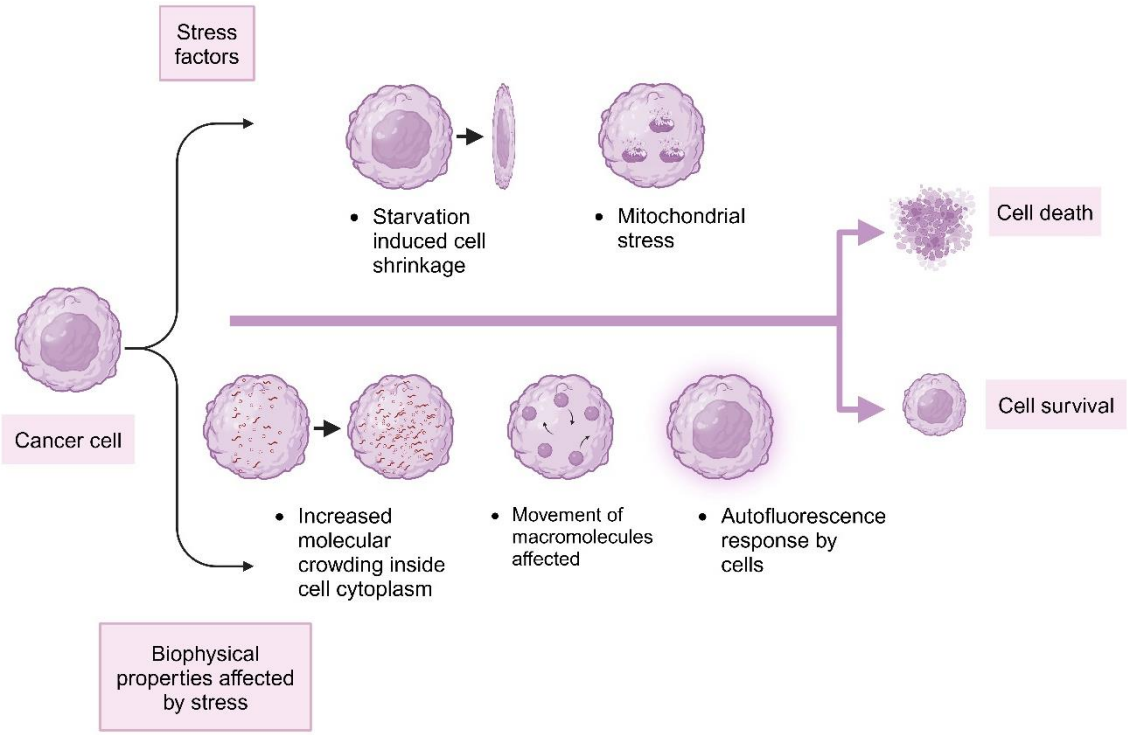

Figure 1: Stress effects on biophysical properties of cancer cells. Nutrient deprivation through starvation induces water loss from cells, altering the intracellular macromolecular environment. Concurrently, drug-induced mitochondrial stress disrupts cellular functioning by producing autofluorescence species from damaged mitochondria. Collectively, these stressors lead to compromised cellular integrity and altered biophysical properties, ultimately causing cell death.

1.1.1 Cellular starvation

Nutrient deprivation, which is achieved by removing glucose from cell surroundings, is a form of starvation. Under nutrient-restricted conditions, cells limit biosynthesis and activate catabolic processes, causing increased energy conservation. On the other hand, under nutrient-rich conditions, cells engage in anabolic pathways, resulting in increased biosynthesis of macromolecules like proteins, lipids, and sugars by utilization of energy in the form of ATP. Cellular starvation is intricately linked with increased stress in many living organisms. During starvation, various biological processes get disrupted, including pro-oxidant: antioxidant balance, increased endoplasmic reticulum stress leading to accumulation of unfolded proteins, and generation of reactive oxygen species (ROS) leading to mitochondrial dysfunction - all contributing to a higher probability of cell death[4].

1.1.1.1 Bacteria

Starvation has been extensively linked with increased stress resistance in bacteria. Starvation induces cytoplasmic shrinkage due to a reduction in cell volume and decreased diffusive motion of nanoparticles inside the cytoplasm. However, in bacterial cytoplasm, the diffusion coefficients (on a micrometer length scale) remain unperturbed/comparable to exponentially growing cells, indicating that cytoplasm remained relatively stable under starvation conditions[5]. This could be linked to bacterial stress resistance.

1.1.1.2 Yeast

In yeast, starvation affects cell division, intracellular diffusion, and changes in viscosity, among other processes. A shorter period of glucose starvation has a low impact on cell growth, but prolonged periods of starvation halt cell growth. In a continued starvation state, low metabolic rate, arrested growth, and cell dormancy are observed for the continued survival of the organism[6]. Cell growth is replenished when the nutrients/glucose supply is restored. Glucose depletion leads to changes in macromolecular mobility inside the nucleus and cytoplasm. Decreased glucose consumption reduces cell volumes by up to 15%, further impeding the macromolecular movement and protein-protein interactions[7].

Heat, in combination with nutrient deprivation, significantly influences yeast's response to changes in viscosity. At increasing temperatures (22°C to 42°C), measured cytoplasmic viscosity in yeast was 80% higher than controls, indicating deviations from expected behaviour according to the Stokes-Einstein equation[8]. Glucose deprivation was also reported to directly effect viscoadaptation (the ability of the system to adapt to viscosity changes), modulating the solubility and regulation of some molecules like glycogen and trehalose[8].

1.1.1.3 Healthy mammalian cells

Nutrient deprivation and water removal in mammalian cells create a solidified cytoplasmic system, forcing the cells to adopt a dormant state. Under these conditions, cells sustain themselves by reducing their metabolic output and energy consumption and going into an energy conservation mode. Cell cytoplasm undergoes cytoplasmic solidification due to the formation of macromolecular assemblies like stress granules and p bodies, which are highly favoured in stressful conditions. These solid structures provide structural support to cells under starvation stress[9]. Subcellular responses from cell organelles like ER (endoplasmic reticulum), nucleolus, and lysosomes play a key role in adaptive regulations during nutrient deprivation. For example, acetyl-CoA (coenzyme A) metabolite depletion induces nucleolar remodelling,

inhibiting pre-rRNA synthesis. This activates the p53-mediated stress response. Thus, the nucleolus acts as a sensor organelle to induce stress response on depletion of a specific metabolite[10].

1.1.1.4 Cancer cells

Cancer cells are more complicated than other living cells. Nutrient-deprived conditions in the tumour microenvironment induce apoptotic cell death. However, this apoptotic process also activates hypoxia-inducing factor (HIF), which promotes angiogenesis and tumour metastasis[11]. Thus, while starvation in cancer cells may initiate a death response, it does not guarantee cell death. Ongoing research on differential chemotherapy based on starvation is focused on testing the validity of the above-mentioned claims[12].

Cancer cells survive on high concentrations of glucose, due to constant energy demands (Warburg effect)[13]. Thus, changes in glucose concentrations (a form of nutrient deprivation), make them sensitive to survival. While cancer cells are continually reprogramming themselves based on how dynamic their surroundings are, implementing nutrient deprivation as a stress response has been explored as a potential factor excessively affecting cell growth and survival[14].

Alternative studies suggest that besides glucose, cancer cells use multiple other nutrients including, acetate, lactate, fatty acids, and glutamine, to support their metabolic demands[15]. However, the high metabolic energy demand for continuous growth and adaptation supersedes these alternate pathways in the long-term survival of tumour cells in a glucose-deprived environment. This raises questions such as: What happens to the cells when their energy reserves are depleted during starvation? Are these cells capable of sensing the declining glucose levels in their surroundings? Do they develop novel mechanisms to conserve energy for survival until conditions improve? Cells continuously try to strike a delicate balance between survival and adaptation strategies under stress conditions. Regulation of cell volume is one such mechanism. Correlating these mechanisms could provide novel insights into determining cancer cell's glucose dependence.

1.1.2 Mitochondrial stress-induced cell death

Regulated forms of cell death are intentionally employed by our bodies to keep us healthy and growing. Stress-induced cell death, however, could lead to pathologies such as cardiovascular dysfunction, metabolic syndrome, and cancer[16,17]. Mitochondrial dysfunction has emerged as a common precursor in all these disease conditions. The focus of this thesis remains on one emergent pathology, namely cancer. Increased metabolic demands of cancer cells abuse mitochondrial functions by disrupting electron transport chains, accumulating reactive oxygen species, and causing mitochondrial membrane potential disruption. This leads to increased mitochondrial stress. When mitochondria experience stress, they send signals to the entire cell to initiate an adaptive response known as integrated stress response (ISR). ISR is a broad response system that helps cells cope with stress by either regulating protein synthesis or pushing them toward apoptosis if the stress is too severe. ISR thus acts as a sensor for mitochondrial dysfunction.

Staurosporine (STS) is a broad-spectrum kinase inhibitor that induces apoptosis by inhibiting several protein kinases essential for cell survival and growth. One major event triggered by STS is mitochondrial dysfunction, which initiates a cascade of stress responses within the cell. Mitochondrial membrane integrity is compromised post-STS treatment, leading to membrane permeabilisation and the release of cytochrome C from the mitochondrial membrane into the cytoplasm. This leads to the activation of caspases, initiating the process of apoptosis. Prolonged exposure to STS causes severe mitochondrial damage. This activates ISR, sensitizing cancer cells towards apoptotic cell death.

A stressed mitochondria is one of the major reasons for ISR-induced cell death. Probing the biophysical properties of cells under these conditions could be a valuable tool for monitoring the underlying events leading to cell death. For instance, real-time monitoring of cellular stress could allow tracking of biochemical and structural changes in cytoplasm or mitochondria, further giving insights into how these changes transition from survival mechanisms to cell death. This could optimise drug treatments in cancer therapies, primarily focused on inducing cell death in malignant cells.

1.2 Biophysical properties of cells

Biophysical properties can serve as potential markers for identifying different types of cells and physiological changes occurring within the cell. They can also be employed as label-free markers for understanding molecular events. These include macromolecular crowding (increased concentration of macromolecules inside the cytoplasm), autofluorescence activity (inherent fluorescence of molecular species), and diffusion and viscosity alterations[18].

The intracellular environment comprises multiple molecular crowders, including proteins, carbohydrates, nucleic acids, organelles, cytoskeleton, and other cellular bodies, with sizes ranging from a few nanometers to hundreds of nanometers. Interactions between these molecules are responsible for the life as we know it. For these molecules to interact, there is continuous movement inside the cells. These molecules must move in a dense environment of thousands of other biomolecules to find their target, perform their function, and repeat the cycle. Thus, intracellular diffusion can be a limiting factor in cellular functioning. This makes it essential to understand the physical chemistry of a crowded environment, such as cell cytoplasm.

While changes in the diffusion of molecules inside cells could highlight their physical state, changes in the fluorescent properties of these molecules give information regarding the chemical state of a cell. Alterations in cellular fluorescence are the result of changing reservoirs of autofluorescent species. Identifying these autofluorescent molecules in living systems could enhance the development of non-invasive, label-free methods for distinguishing between different cells based on their physiological states, thereby serving as biomarkers for key cellular activities[19–21].

Thus, studying biophysical properties at a single cell level could reveal important information about cell behaviour, help identify diseases, and plan therapeutic interventions.

1.2.1 Macromolecular crowding

Macromolecular crowding is a feature of every living cell, and macromolecules occupy a large portion of cell volume. Macromolecular crowding regulates intracellular transport by affecting the diffusion of molecules, which, in turn, affects cell function. As shown in a 2015 study[22], increasing small crowding agents heightens the effective viscosity within the cell, slowing down the diffusion of the motor domains of motor proteins like Kinesin-1. This hindrance leads

to a decrease in motor velocity, affecting the efficiency of intracellular transport. Crowding influences the kinetics of cellular processes by impacting the diffusion and binding rates of molecular motors, thereby regulating overall cell function.

Major molecular processes occur in cell cytoplasm by diffusion of various biomolecules from one place to another. In a crowded cell cytoplasm, characteristic diffusion times and molecular interactions can help understand cell behaviour at the molecular level, in normal and pathological conditions. For instance, a study performed in A549 cells demonstrated an increased molecular crowding due to osmotic compression in early apoptotic phases of the cells, leading to hindered intracellular transport, right before caspase activation[23].

1.2.2 Diffusion and Viscosity

As discussed in the previous chapter, the movement or diffusion of macromolecules inside the cell is the essence of its function. Diffusion of molecules is affected by solvent viscosity, i.e. the drag force experienced by the molecule due to the liquid around it. In complex fluids like cytoplasm, which contains macromolecules and other crowders, the effective viscosity is determined by both the solvent and the surrounding macromolecular environment. This effective viscosity is scale-dependent, varying with the length scale of the observed molecular interactions. Cell cytoplasm behaves like a liquid for molecules <100 nm and as a gel for molecules >100 nm[24]. This potentially leads to alterations in viscosity experienced by macromolecules at different length scales[25].

Intracellular viscosity impacts the overall mechanical behaviour of the cells. For example, the actin-myosin dynamic is responsible for all the cell's mechanical work by converting the chemical energy into mechanical energy. Longer relaxation times of the actomyosin network result from increased intracellular viscosity, directly influencing cellular mechanosensitivity[26]. Some studies suggest that these observations indicate that cells function as "liquid motors" by inducing changes in intramolecular crowding. Various cellular compartments demonstrate differences in measured viscosity, including cell membrane, cytoplasm, nucleus, and subcellular organelles like mitochondria, endoplasmic reticulum, Golgi, and intracellular vesicles. Furthermore, alterations in macromolecular crowding have been linked with changes in diffusion rates or intracellular viscosity in cells during stress. For example, mitochondrial matrix solvent exhibits changes in viscosity, particularly under stress conditions such as chloramphenicol treatment[27]. This results in an eightfold increase in matrix viscosity compared

to the baseline conditions in untreated cells, which have a viscosity of 3.69 cP of fluorescent proteins like AcGFP1. Another study highlighted the effect of osmotic stress on macromolecular crowding by tracking the diffusion of GFP proteins in cancer cells by FCS measurements. The increase in viscosity (up to 5-fold from baseline values of 1 cP) was linked with increasing intracellular crowding rather than structural or conformational changes in GFP[28].

Studying an increase in intracellular viscosity is important because it can potentially hinder the diffusion of macromolecules intracellularly, affecting biochemical reactions. These changes affect overall intracellular transport dynamics and cellular homeostasis. Studying viscosity increase during stress conditions helps refine the design of molecular probes and sensors for real-time monitoring of cellular responses to stress. Additionally, it can enhance the development of drug delivery systems, allowing for more precise targeting and diffusion of therapeutic agents in stressed or diseased cells.

1.2.3 Autofluorescence

Fluorescence is the emission of light from a molecule that has absorbed light. A molecule fluoresces when it absorbs photons and subsequently re-emits them, usually at a longer wavelength, due to energy loss through non-radiative processes. It happens on very short timescales, within nanoseconds after initial excitation[29]. Some cellular components can exhibit fluorescence on exposure to light of a specific wavelength, which is defined as autofluorescence. Autofluorescence in cells has been recorded from various molecules, including collagen, elastin, cell organelles like mitochondria and lysosomes, but most importantly from the cyclical ringed structures like flavoproteins- FAD (flavin adenine dinucleotide), NADH (nicotinamide adenine dinucleotide), nucleotides and aromatic amino acids[30,31]. FAD is excited at λ_{ex} = 365 - 490 nm and emits at λ_{em} = 520 nm[32]. NADH excites at λ_{ex} = 340-370 nm and emits at λ_{ex} = 450 nm[33]. These molecules can be distinguished based on differences in their fluorescence lifetimes in the cell system. Free NADH exhibits lifetimes around 400-500 ps, whereas protein-bound NADH exhibits longer lifetimes in the range of 2500 ps[34]. Estimating free NADH to bound NADH provides insights into cell metabolism, classifying cells in various metabolic ranges. FAD lifetimes are different from these lifetimes. Three lifetimes are recorded for FAD in solution, highly dependent on its conformation. A short-lived component (~1 ps) attributed to water relaxation around flavin and the longer

lifetime component (9 ps). Both correspond to a quenched state of the molecule. The Lifetime measurements at 2.6 ns correlate with a steady-state fluorescence emission[35]. FAD exists in an unstacked confirmation at this lifetime, allowing for more efficient radiative decay of excited states.

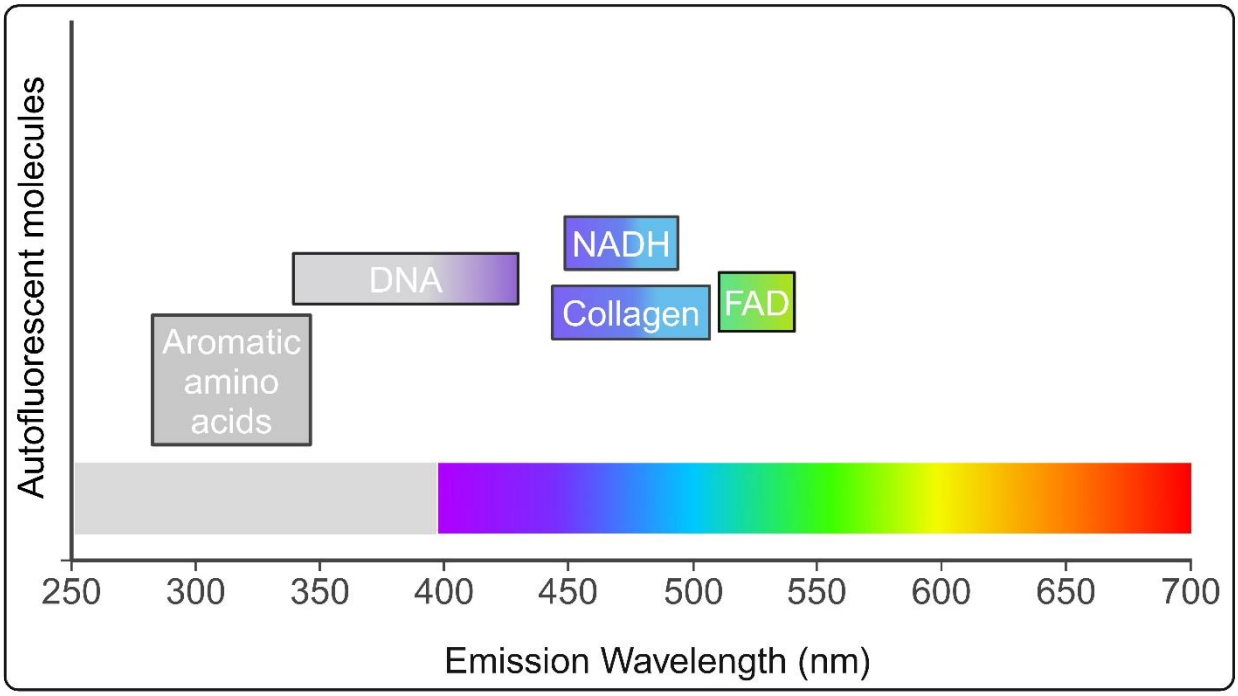

Figure 2: Autofluorescence of cellular organelles and molecules. Each box colour corresponds to the emission wavelength (in nm) of autofluorescent molecules, as shown on the x-axis.

FAD and NADH have previously been used as biomarkers of cellular metabolism. A high NADH fluorescence is characteristic of a reduced metabolic state, while a high FAD fluorescence is characteristic of quiescent or apoptotic cells[36,37]. Fluorescence profiles of these molecules are crucial for designing drugs that target a specific cell population during chemotherapy, thereby reducing tumour[38] recurrence. Drugs targeting quiescent or apoptotic cells specifically, have demonstrated improved efficacy in cancer treatment.

The autofluorescence response of NADH, coupled with FAD provides an accurate estimation of cellular bioenergetics, serving as a powerful tool for segregating various cell populations in tumours. For example, an increase in FAD fluorescence is characteristic in cancer biopsies from breast tissue, with an increase in redox ratio up to 27%[39,40]. The redox ratio measures relative concentrations of reduced and oxidised forms of a redox-active molecule like NADH and FAD. An increased redox ratio indicates a higher level of reduction, which is usually associated with cancerous activity. Studies suggest a strong link between an increase in

autofluorescence of NADH and FAD molecules in cells as an indication of cell death due to mitochondrial stress. FAD and NADH are majorly present in mitochondria, along with their cytosolic fracrions[41,42]. Fluorescence lifetime studies of these endogenous molecules are impactful in detecting cell death and changes in metabolic processes based on conformational differences[43]. Drugs impacting mitochondrial function and cellular fluorescence could provide insight into the importance of mitochondrial stress during cell death.

Autofluorescence has been studied as a physical indicator of cellular response towards stress in both prokaryotes and eukaryotes. A study done on *E.coli* suggested that exposure to different stressors led to an increase in the "green fluorescence" due to increased protein synthesis and other molecules, especially flavins[44]. Elevated cellular autofluorescence in bacteria is a critical stress response indicating increased energy production and detoxification by removing reactive oxygen species. Ampicillin-treated *S. cerevisiae* shows an increase in autofluorescence per unit volume, with its spectral properties resembling those of flavin proteins. Thus, autofluorescence response in prokaryotic and eukaryotic cells symbolises a universal survival methodology under stress conditions[45,46].

1.3 Methods to Study Cellular Biophysics

1.3.1 Fluorescence microscopy

Fluorescence occurs when a molecule absorbs light of a short wavelength (high energy) and emits a photon at a longer wavelength (lower energy). Fluorescence from specific dyes has been used to create images of samples with laser-spanning fluorescence microscopes since 1980's[47]. Fluorescence microscopy, in conjugation with super-resolution techniques, is one of the most powerful tools in evaluating biological substructures (Fig 3). Single-molecule fluorescence microscopy can study molecular-scale processes, including diffusion, molecular interactions, and the behaviour of proteins at the nanoscale[48]. Integrating fluorescence microscopy with fluorescence lifetime imaging and single molecule detection techniques like FCS gives valuable insights into multidimensional biological research.

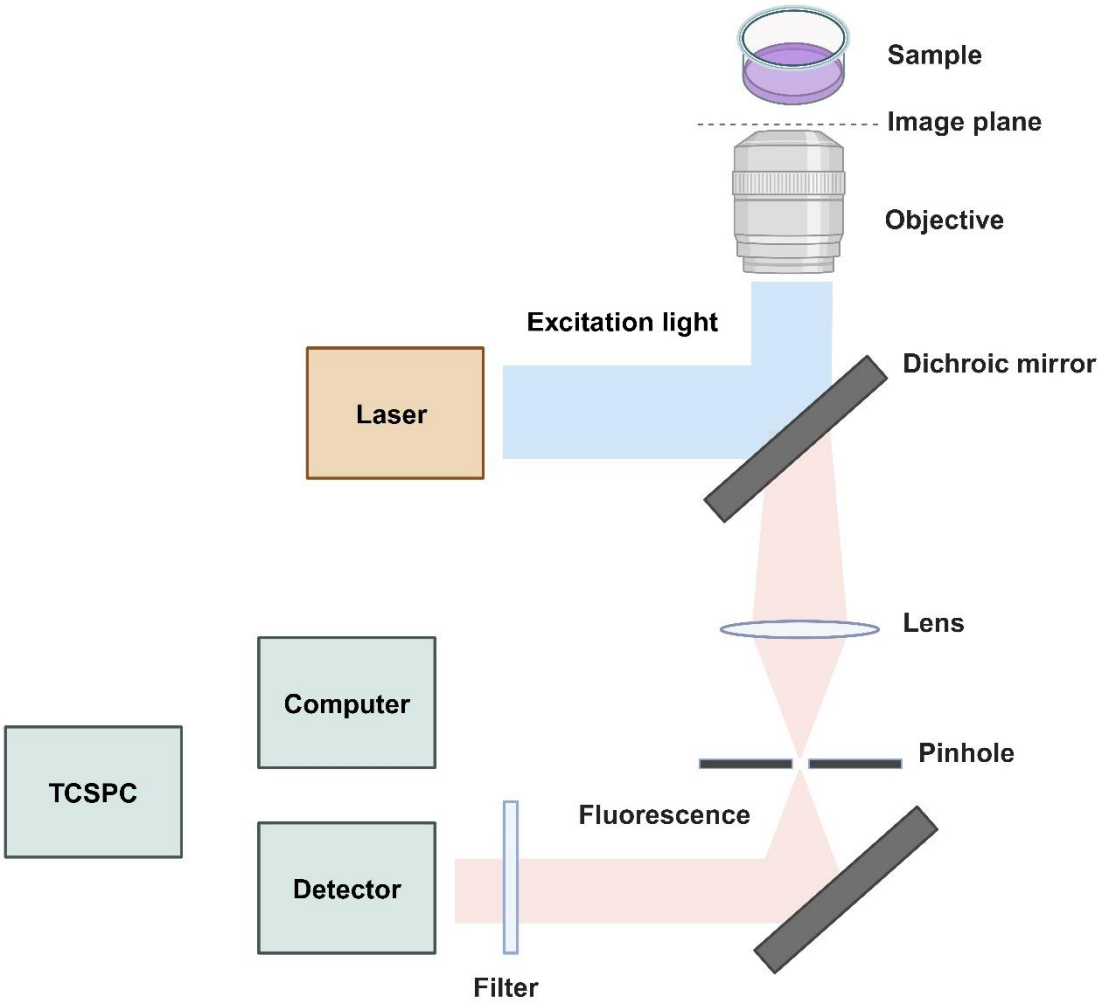

Figure 3: Confocal microscope set up with Time correlated single photon counting (TCSPC). The microscope is attached to a laser (light source), which emits an excitation beam. The beam travels towards the dichroic mirror, which acts as a filter and allows the light of a specific wavelength to pass through. It reflects the excitation beam towards the objective, which focuses the light on the sample. The fluorescent sample gets excited, and its fluorescence is collected, passing through the same light path up to the dichroic mirror. A pinhole attached below filters the collected light by removing the signal coming from out of the confocal plane. Eventually, the light travels to the detector, which is connected to the photomultiplier tube and converted into a digital form. The confocal microscope is further connected to a TCSPC apparatus for FCS set-up, which helps detect up to a single photon from the fluorescent sample.

1.3.1.1 Fluorescence correlation spectroscopy

FCS is a powerful technique to quantify molecular dynamics in living cells, typically at very low concentrations, often in the nanomolar range. It does so by analysing fluorescence intensity fluctuations of diffusing biomolecules in a small confocal volume of a few femtolitres[49,50]. These fluctuations are fingerprints of molecules diffusing through the confocal volume (Fig

4b,c), which is created by a laser-focused beam and experimentally determined by calibration[51]. Intensity fluctuations are recorded as a function of fluorescence intensity over time and are examined using correlation analysis (Fig 4c,d). This analysis contains information regarding the average number of molecules and the average diffusion time of flight within and across the confocal volume, respectively. By calculating the confocal volume's shape and size, the diffusion time can be converted to the translational diffusion coefficient of the molecules. The theoretical confocal volume can be calculated by:

$$v_{eff} = \frac{4}{3}\pi w_{xy}^2 w_z \qquad \text{Eq. 1}$$

Where; w_{xy} is the radial beam waist (radius in the lateral x-y plane), w_z is the axial beam waist (along the z-axis). With empirical validation however, confocal volume is derived based on both FCS measurements and specific diffusion characteristics;

$$\kappa = \frac{w_z}{w_{xy}} \qquad \text{Eq. 2}$$

Where, parameter κ is defined as the ratio of the axial beam waist w_z to the radial beam waist w_{xy}. The correlation analysis yields an autocorrelation curve of fluctuation intensity G(τ) on the y-axis over a period of time (Fig 4d). G(τ) is the time average of I(t) and the intensity fluctuation after the delay time I(t + τ).

$$G(\tau) = \langle I(t) * I(t+\tau)\rangle \qquad \text{Eq. 3}$$

It normalises intensity fluctuations over time by the square of averaged fluorescence intensity (dI(t) - ‹I(t)›), which can be represented as follows:

$$G(\tau) = \frac{\langle I(t)*I(t+\tau)\rangle}{\langle I(t)\rangle^2} - 1 = \frac{\langle dI(t)*dI(t+\tau)\rangle}{\langle I(t)\rangle^2} \qquad \text{Eq. 4}$$

This correlation curve can then be fitted to appropriate physical models for obtaining information about molecular behaviour in cells, including, diffusion coefficients, concentrations, kinetic constants, and other molecular interactions[52]. The autocorrelation curve is obtained by averaging fluctuations from molecules together, even though the signal from a single molecule is important for generating these fluctuations. Therefore, the correlation curve becomes a probability function and can be described as follows. At correlation time τ = 0, the probability of observing a photon is the highest; that is, G(0) is at the maximum value (this is because we are correlating the signal with itself at the same time point, the probability of detecting the photon at the same moment is the highest). As τ increases or there is a delay, we

measure how the intensity of the signal at time t correlates with the intensity at a later time t + τ, and the probability of detecting another photon decreases (because photons are emitted at random intervals and as time progresses, the correlation between intensity at t and t + τ decreases). Therefore, for a three-dimensional diffusion of a single component, the autocorrelation curve is presented as:

$$G(\tau) = \frac{1}{Np}\frac{1}{1+\left(\frac{\tau}{\tau_D}\right)\sqrt{1+\frac{1}{\kappa^2}\left(\frac{\tau}{\tau_D}\right)^2}} \qquad \text{Eq.5}$$

$$G(0) = \frac{1}{Np} \qquad \kappa = \frac{w_z}{w_{xy}} \qquad \tau_D = \frac{w_{xy}^2}{4D}$$

Where N_p is the number of particles, κ is the structure parameter obtained from the confocal volume during calibration and τ_D is the time of flight. The time of flight or τ_D of the molecule obtained from the curve is proportional to the mean distance (w_{xy}) travelled by the molecule, emitting photons and its diffusion coefficient. N_p or the average number of molecules can be

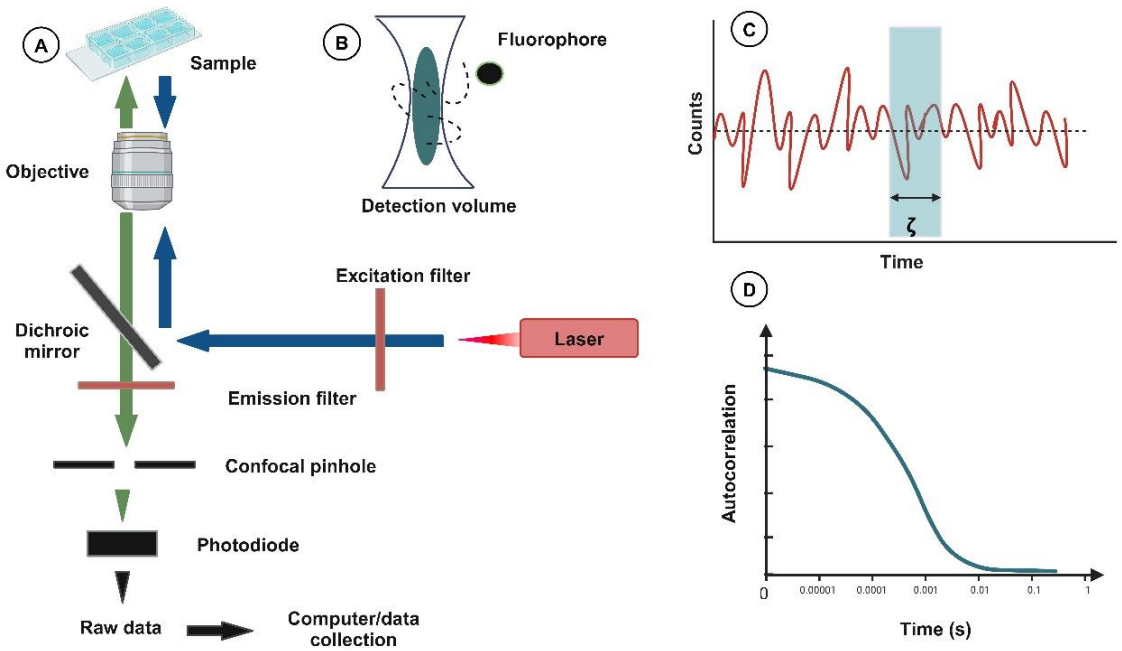

Figure 4: Theoretical concepts of FCS. (A) The confocal set up for the FCS remains similar to the one described in Fig 3. (B) Confocal volume calculated through calibration using probability density function, is an ellipsoid. Fluorescence from the samples is captured as fluctuations in intensity over a period of time, when fluorophore diffuses through the confocal volume of defined dimensions. (C) The time trace data from intensity fluctuations determines tau d (**τ**). (D) The autocorrelation curve is obtained by converting the intensity signal to correlation function over time. The G(0) obtained is then fitted with appropriate mathematical model to calculate molecular diffusion.

further calculated from G(0). FCS can be termed as a single particle tracking technique, that makes it essential for the samples to be in the range of a few nM, corresponding to 1-100 molecules in the confocal volume.

1.3.1.2 Fluorescence lifetime imaging

Fluorescence lifetime imaging (FLIM) is an advanced imaging technique that utilises the fluorescence of endogenous molecules by measuring their fluorescence lifetimes or decay times. The lifetime of a fluorophore is the average time spent in an excited state before returning to the ground state, emitting a photon. A fluorophore's environment contributes to these lifetimes, which are characteristic of each molecule. FLIM allows the distinction of fluorophores with similar fluorescence spectra by measuring differences in their lifetimes rather than relying solely on intensity or spectral characteristics. FLIM measures lifetimes using short-pulsed lasers (10^{-12} s - 10^{-15} s) for sample excitation[53]. For detection, a laser scanning microscope with a pinhole blocks all photons from out of the focus plane. The emitted photons then go through an objective lens and are separated using a dichroic beam splitter. Photons are quantified by photomultipliers or photodiodes (detectors). These incoming photons are recorded using a time-correlated single photon counting (TCSPC) apparatus attached to the laser scanning microscope.

TCSPC measures fluorescence lifetimes with high precision by using fast response detectors. In TCSPC, fluorescence intensity values are recorded in subsequent time channels. These channels contain information about the number of recorded photons after the initial excitation pulse. This generates a histogram or decay curve for an individual point or pixel in the image. To precisely measure fluorescence lifetime decay, the arrival times of thousands of photons at each pixel must be recorded[54]. This technique accurately estimates fluorescence decay parameters with low photon counts as well. TCSPC FLIM analysis can be performed by using a single exponential decay model. In this model, the fluorescence intensity decreases exponentially with time, giving a single characteristic lifetime. However, biological systems show more complex behaviours. Fluorescence, in these cases, can arise from two different energy states, environments or conformations. In biological systems, different lifetimes indicate different molecular environments, binding states, or conformational changes. In these cases, a 2 or 3-exponential model is employed. These models are more complex and contain several decay components and amplitude coefficients. The final FLIM image is usually colour-

coded; different colours correspond to lifetimes or fluorescence decay. Fluorescence decay is represented as:

$$I(t) = I_0 \left(A_1 e^{\left(-\frac{t}{\tau 1}\right)} + A_2 e^{\left(-\frac{t}{\tau 2}\right)}\right) \quad \text{Eq.6}$$

Where,

I(t) is the fluorescence intensity at time t,

A1 and A2 are the initial amplitudes of the decay components,

$\tau 1$ and $\tau 2$ are the lifetimes for the two decay components.

Understanding TCSPC and FLIM data using exponential decay data fitting has been the most common method of identifying characteristic lifetimes of autofluorescent species in solutions and cellular samples[55]. Autofluorescence measurement using fluorescence lifetime imaging is an excellent source of studying spatiotemporal changes in intracellular processes by estimating the lifetimes of a fluorophore[56].

1.3.2 ATP detection

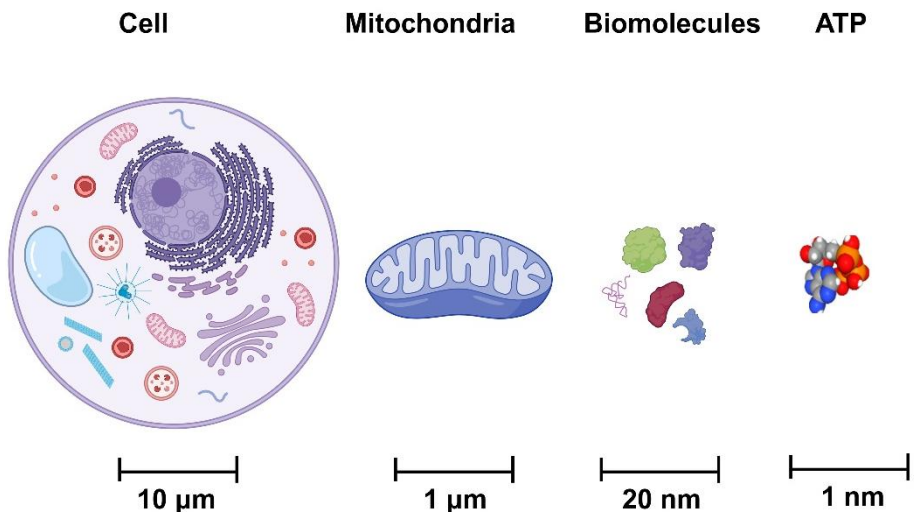

Figure 5: Scaling comparison of different molecules found inside the cell. A typical cancer cell is 10-20 µm in diameter. Each cell contains 100-200 mitochondria (1 µm in diameter). This is 10x smaller than a cell itself. Major macromolecules such as ribosomes, proteins, and vesicles are ~15-20 nm in diameter, which are 1000x smaller than a cell. 1 molecule of ATP is 1 nm in diameter, 10000x smaller than a cell. This molecule maintains the energy balance inside a cell, 10,000x bigger than itself. This schematic representation underscores the critical role that even the smallest molecules (nanometer scale) play ensuring proper cellular function.

Cells hydrolyse adenosine triphosphate (ATP) to obtain energy for its molecular and cellular processes[57]. ATP production – mainly happens by glycolysis (glucose breaking down into pyruvate), citric acid cycle (pyruvate further breaks down to generate ATP) and oxidative phosphorylation in mitochondria (electron transport chain)[58]. The size of an ATP molecule is ~1 nm, which is 10,000 times smaller than a mammalian cell (Fig 5). The intracellular concentration of ATP in a normal cell is ~2.3 mM[59], which is far more than what is required for energetic requirements from ATP. Such high concentrations of such a small molecule often raise questions regarding other uses of ATP than just the cellular energy provider. It is now believed that ATP also helps prevent protein aggregation and stabilisation[59].

1.3.2.1 Cellular ATP as an important marker

Mammalian cells produce 50 million ATP molecules per cells, and have a storage capacity of 6 billion ATP molecules/ cell (1-10 mM) at any given time[60]. Cellular energetic demands are met by utilising macromolecular precursors like lipids, sugars and proteins to generate ATP. Cancer cells in sugar-depleted environments (starvation), experience growth inhibition, cell cycle arrest, and often cell death[61]. These outcomes are tightly linked to fluctuations in intracellular ATP levels[62]. Cells with high ATP levels are phenotypically aggressive, show stem-like properties and are multi-drug resistant[63]. Conversely, low ATP levels trigger alternate survival pathways like AMPK-enzyme activation to reduce energy-consuming processes[64]. Thus, ATP has emerged as a critical biomarker for assessing the metabolic fitness of cancer cells. This has important implications in designing treatments for cancer cells with metabolically altered profiles. Various sensors have been developed to quantify intracellular ATP levels,. Different types of sensors for measuring ATP dynamics in cells are presented in the table below (Table 1).

Table 1: Characteristics and applications of various ATP sensors. Sensors highlighted in grey were utilised in this study.

Sensor Type	Mechanism	Advantages	Limitations	Detection Range	Sample Type	Examples
Luminescence-based	Luciferase enzyme converts luciferin into oxyluciferin in presence of ATP and releases light. The intensity of the light emitted is directly proportional to the amount of ATP present in the sample.	Highly sensitive, rapid detection, quantitative	Low spatial resolution, unstable reagents, environmental sensitivity	~10^{-9} to 10^{-12} M	Chemical solutions, cell lysates, microbial samples	CellTiter-Glo[65], ATPlite[66],
FRET-based Sensors	Measures energy transfer between donor and acceptor fluorophore. ATP binding induces conformational changes, bringing fluorophores closer together and increasing energy transfer. Change in fluorescence intensity allows ATP quantification.	High sensitivity and specificity, real-time data monitoring,	Photobleaching, complex probe design, potential steric hindrance	~10^{-6} to 10^{-9} M	Live cells, tissue sections, transgenic organisms, cell-free systems, microbial samples	Ateam[67], Perceval[68], RhoATeam[69]
Genetically Encoded Sensors	Plasmids containing ATP binding proteins are transfected into cells. ATP-protein interactions modifies emission properties. Changing fluorescence intensity quantifies ATP levels.	In-vivo quantification, high specificity, non-invasive, cellular integration	Limited by transfection efficiency, overexpression and cellular toxicity	~10^{-6} to 10^{-9} M	Mammalian cell lines, tissues, transgenic organisms	FLIP-ATP[70], MALIONR[71]
Electrochemical Sensors	Electrochemical ATP sensors detect ATP through its oxidation at an electrode modified with specific enzymes. The resulting electrochemical signal, typically measured as current, is directly proportional to the ATP concentration in the sample.	High sensitivity, can be miniaturized, rapid response, cost effective	Electrode fouling, calibration requirements, limited lifespan	~10^{-6} to 10^{-9} M	Living cells, cell lysates, tissue samples	Carbon nanotubes[72]
Chemiluminescent-based Sensors	Chemiluminescent ATP sensors utilize ATP to catalyze a reaction for producing excited chemical species. On returning to ground state, it emits light. Intensity of the emitted light is directly proportional to the concentration of ATP in the sample.	Highly sensitive, requires no external light source, rapid results	Limited shelf life, difficult real-time measurements	~10^{-6} to 10^{-12} M	Chemical solutions, cells, biological fluids	CL-ATP[73]
Colorimetric Sensors	ATP interaction with chemical reagents produces a colour change, which is measured spectrophotometrically. The extent of the colour change is proportional to the concentration of ATP in the sample.	Simple, low-cost,	Low sensitivity, unsuitable for live-cell measurements	~10^{-6} to 10^{-4} M	Chemical products, cell lysates	Colorimetric ATP biosensor, Si nanoparticles[74]
Ratiometric ATP Sensors	Two different fluorophores are used; binding of ATP causes a change in the emission ratio of the two fluorophores, allowing for quantitative measurements of ATP concentrations.	Allows real-time, dynamic ATP concentration measurement	Complex design, limited sensitivity at low ATP concentrations	~10^{-6} to 10^{-8} M	Live cells, tissues, cell lines	Ratiometric ATP sensor[75]
Nanosensor-based Sensors	Nanosensors are designed to respond to ATP binding with a measurable change in fluorescence or electrical conductivity.	High sensitivity, ability to target specific locations	Potential biocompatibility issues, complex fabrication	~10^{-6} to 10^{-9} M	Biological fluids, cell lysates, biofilms	Gold nanoparticles[76], Silver nanoclusters[77]

1.3.3 CRISPR/Cas9 gene editing

Gene editing is a powerful biotechnological tool that allows DNA sequence alteration in an organism with high precision. The alterations involve adding, removing, or modifying specific DNA sequences within the genome to change the organism's genetic code. This technique has been instrumental in broadening our understanding of gene function and designing appropriate therapies for genetic disorders. In the last few decades, there has been a few gene editing techniques which have revolutionised the field of genetic engineering. These are listed in the table below (Table 2).

Out of all the techniques, CRISPR-CAS9 is widely considered the most powerful and versatile gene-editing tool available today. This is due to its precision, efficiency, ease of use and broad applicability across fields like medicine, agriculture and basic research. CRISPR (clustered regularly interspaced palindromic repeats) was discovered as a bacterial immune system and uses a combination of single guide RNA (gRNA) and CRISPR-associated endonuclease protein called cas9 to target and modify DNA sequences[78]. A synthetic RNA molecule (gRNA) is designed to direct the endonuclease complex (cas9) to the target DNA sequence. This sgRNA is engineered to match the target DNA sequence that needs editing. sgRNA-cas9 complex is then guided to the target site, cas9 recognises a short DNA sequence called Protospacer adjacent motif (PAM), which is usually a sequence of "NGG"[79]. The PAM sequence is located adjacent to the target site and is crucial for cas9 activation. Upon correct recognition of the target sequence and PAM, cas9 induces a double-strand break (DSB) at the target site. As soon as a DSB is generated in the sequence, DNA repair mechanisms (usually non-homologous end joining) are activated to repair the DNA strand break, often introducing small insertions or deletions (indels) at the target site[80]. This leads to disrupted gene function or a knockout (Fig 6). The technique has already been used to target multiple disease-causing genes, creating animal models for sickle cell disease, muscular dystrophy, CAR-T therapy, cancer and cystic fibrosis[81,82]. CRISPR gene editing was employed to create a knockout cell line for this thesis.

Table 2: Gene editing techniques, their discovery and applications.

Gene Editing Technique	Discovered	How It Works	Applications
CRISPR-Cas9	2012	Uses a guide RNA (gRNA) to direct the Cas9 enzyme to a specific DNA sequence, where it makes a precise cut. The cell's natural repair processes then edit the gene.	Gene therapy (e.g., sickle cell anaemia, cystic fibrosis), cancer treatment, agricultural improvements, disease modeling[83].
Zinc Finger Nucleases (ZFNs)	1990s	ZFNs are engineered proteins with a DNA-binding domain (zinc fingers) and a DNA-cleaving domain (FokI nuclease) that target specific DNA sequences, allowing for targeted DNA modification through repair mechanisms.	Gene therapy (e.g., HIV treatment), creating herbicide-resistant crops, functional genomics (gene knockouts)[84].
TALENs (Transcription Activator-Like Effector Nucleases)	2010	Composed of TALEN protein domains and FokI nuclease. TALENs recognise specific DNA sequences, and FokI induces a double-strand break for targeted editing via repair.	Gene knockouts in plants and animals, disease research, and agricultural biotechnology (disease resistance)[85].
Mega nucleases	1980s	Mega nucleases are highly specific DNA-cutting enzymes that target specific sequences, but are difficult to re-engineer for new targets.	Used for highly specific gene modifications in research, though less versatile and flexible compared to other techniques[86].
Base Editing	2016	Base editors induce single-base changes without creating double-strand breaks, using deaminase enzymes to convert one nucleotide to another, e.g., C to T.	Correcting point mutations, studying disease-associated single nucleotide polymorphisms (SNPs), and improving crop traits[87].
Prime Editing	2019 by David Liu's lab	Prime editing is a precise form of CRISPR that can introduce specific changes, including all 12 possible base-to-base conversions, insertions, and deletions without double-strand breaks.	Correcting genetic disorders with complex mutations, creating precise gene edits in disease models, and potential applications in treating genetic diseases[88].

Even though gene editing with CRISPR is the most versatile technique, it has its challenges. Target-specific delivery of sgRNA does not entirely account for off-target mutations and side effects. Analysis of next-generation sequencing (NGS) data revealed that negative supercoiling of DNA, in contact with cas9 and sgRNA complex, leads to an increased super helical density of DNA in the adjacent regions, leading to increased free energy input, preventing other sgRNA-Cas complexes from binding. Cas protein diffuses at 45 $\mu m^2/s$, colliding with DNA 61 times every second. Molecular characteristics such as diffusion rates, macromolecular crowding and intracellular viscosity heavily impact the spatial distribution of transcription factors, thus impacting gene expression[28,89]. In my thesis, I analyse the diffusion coefficients of GFP in knockout cells compared to wild-type cells to highlight post-knockout changes in the nanostructure of cytoplasm.

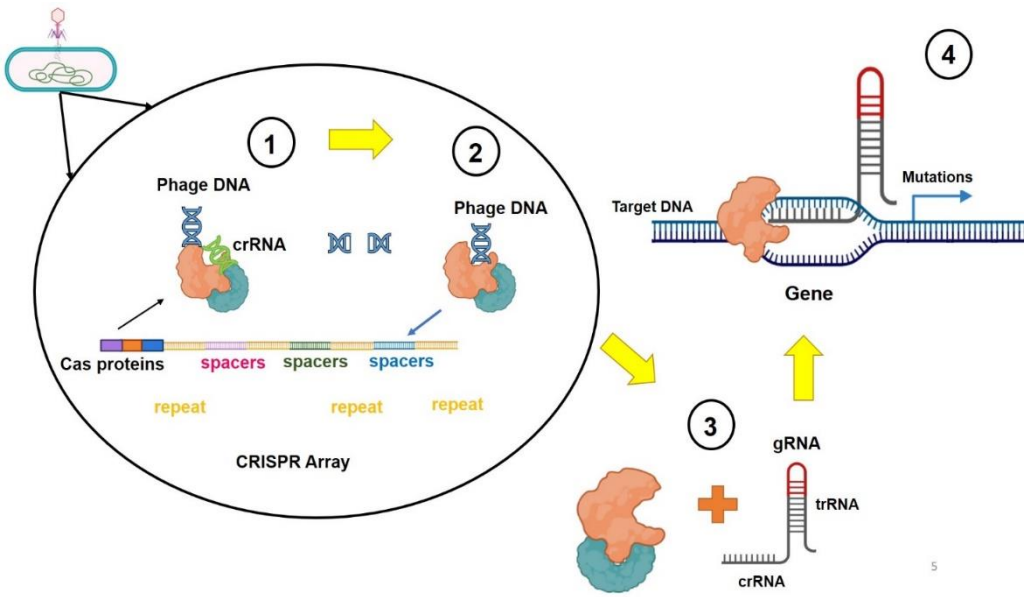

Figure 6: CRISPR-CAS machinery in bacteria as its immune system (1-2) and its application as a genome editing tool in mammalian cells (3-4). (1) The Crispr RNA gets activated on encountering a phage DNA and cuts the phage DNA with a nuclease called CAS9. It incorporates similar phage DNA oligonucleotides and makes CRISPR arrays in its own genome to remember for later infections. (3) CRIPSR-RNA, attached with a guide RNA, complementary to the gene of the target in any cell, is designed. (4) Along the CAS9 nuclease complex, it targets the gene of interest. It makes cuts at specific sites recognised by cas9 protein (PAM sequence), making indels (insertions/deletions) of single or multiple base pairs, thus disrupting gene function or creating a complete knockout.

1.4 Summary

The impact of stress on biological properties of cells like differentiation, gene expression and proliferation has been extensively studied, with tens of thousands of research articles published in the last 2 decades. In contrast, focused research on how stress influences biophysical properties – like macromolecular crowding or diffusion remains limited, with estimated publications in the hundreds. This disparity highlights the broader focus on cell biology compared to more niche research on the biophysical environment inside cells during stress - a niche that arises from the complexity of biophysical research. Studying cellular biophysics reveals critical insights into intracellular environments' physical and chemical mechanical properties, which significantly influence cell behaviour and adaptation during stress. Understanding these biophysical factors complements traditional cell biology approaches, offering a more comprehensive view of how cells perceive and respond to stress. Addressing this gap is a key focus of this thesis. Measuring intracellular alterations in complex fluids like cytoplasm is difficult due to the technical limitations of biophysical methods. Therefore, in-

depth biophysical properties were analysed by using diverse techniques including, FCS, FLIM, and gene editing with CRISPR.

Quantifying cellular biophysical response to stress could be a potential marker for differentiating pathologies. This thesis utilised validated mathematical models to analyse intracellular diffusion in wild-type and knockout HeLa cells during starvation. The work also highlights the importance of autofluorescence as an indicator of stress response across four cancer cell lines. These findings can be generalised to other cell systems to quantify cellular functions in stress. Stress responses are ubiquitous in living organisms, yet methods for identifying common cellular patterns are still lacking. Combining these results with existing data could help establish unified frameworks for understanding stress response in organisms.

2 Results

2.1 Cellular Starvation

2.1.1 Movement at nanoscale in cells

Cytoplasm acts as a mesh-like structure (gel-like morphology) for molecules >100nm in diameter. Whereas smaller molecules (<100nm) experience a more fluidic/liquid nature of cytoplasm. Thus, cytoplasmic viscosity is a determining factor in allowing the movement of molecules intracellularly. This fluidity/viscosity is dependent on the length scale[24]. Eq.7 denotes a mathematical representation of how viscosity depends on the length scale;

$$\eta_{eff} = \eta_0 \, A_{exp} \left[\left(\frac{\xi^2}{R_H^2} + \frac{\xi^2}{r_p^2} \right)^{-a/2} \right] \qquad \text{Eq.7}$$

Where, η_{eff} is effective viscosity experienced by the probe of hydrodynamic radius r_p , η_0 is the solvent viscosity (water, 0.705 mPa·s at 36°C), A is a pre-exponential factor (determined previously as 1.3 ± 0.3 for HeLa cells[24]), R_H is the average hydrodynamic radius of major crowders including proteins, ribosomes and other biomolecules (12.9 ± 2.3 nm for HeLa cells[24]), a is the exponent which defines the nanostructure of the liquid (0.62 ± 0.07 for HeLa cells[24]), which here is the intracellular environment, ξ is the average half distance between the major crowders (3.2 nm for HeLa cells). According to this model, we can estimate the change in viscosity if the radius of the probe and hydrodynamic radius of the crowders (assumed to remain similar under various cell conditions) are known.

Previous studies have shown that intracellular conditions change dynamically during stress in both prokaryotic and eukaryotic cells. Interior of a cell is a complex environment with millions of molecules moving every few seconds or even less. Stress can cause the average intermolecular crowder space - "ξ" to change, thus impacting intracellular viscosity. Various biological processes, including cell migration, motility and diffusion of molecules, have been linked to changes in cellular viscosity [91,92]. Changes in viscosity can alter the shape and structure of the cytoplasm, thereby significantly influencing the production of important signaling molecules involved in processes like cell growth, proliferation, maintenance and repair[93]. Viscosity in living cells refers to the physical constraint that opposes the diffusion of biomolecules through the complex cytoplasmic matrix. As its extension, nanoviscosity can be defined as the drag force experienced by probes in the nanometre range (1-100 nm), in cell

cytoplasm. According to Stokes-Einstein equation[94], viscosity can be defined by the following equation;

$$r_p = \frac{k_b T}{6\pi\eta_{eff} D} \qquad \text{Eq.8}$$

Where r_p is the hydrodynamic radius of the probe, k_b is the Boltzmann constant, T is the temperature (36˚C), η_{eff} is the effective viscosity of the complex fluid (Pa.s) at the given temperature and D is the diffusion coefficient. For size-dependent viscosity, D is inversely proportional to η_{eff}. Hence,

$$\frac{n_{eff}}{n_0} = \frac{D_0}{D} \qquad \text{Eq.9}$$

The results presented in this chapter are in terms of changes in diffusion;

$$H_{diff} = \frac{D_0}{D} \qquad \text{Eq.10}$$

Where $H_{diff} = \frac{D_0}{D}$ is defined as diffusion hindrance.

2.1.2 Measuring diffusion in HeLa cell cytoplasm

2.1.2.1 Diffusion of GFP in cytoplasm during starvation

GFP-transfected HeLa cells were used for these experiments. The GFP gene translates into GFP protein in the cell cytoplasm, which is ~28 kDa in size. The geometrical dimensions of a GFP molecule in terms of its length and diameter were estimated to be 4.2 nm and 2.4 nm, respectively[95]. By measuring the diffusion coefficient of GFP (with hydrodynamic radius = 2.3 nm), H_{diff} inside the HeLa cell cytoplasm during starvation were calculated. FCS curves obtained from the measurements were analysed using a 1-component free diffusion model (refer to appendix B.2 for calibration steps, FCS and confocal set-up). Cells were starved for four consecutive days by changing the nutrient-rich media (DMEM) on day 0 to phosphate saline buffer (PBS with Ca^{2+} and Mg^{2+} ions). Consecutive readings inside cells were taken in 4-5 different cells for four days.

During the first two days of starvation, I found that the H_{diff} in the cell cytoplasm remained constant, though higher than the value recorded on day 0. The diffusion hindrance experienced by the probe varied negligibly on days 1 and 2. However, by day 3, there was a noticeable

increase in diffusion hindrance compared to day 0. During the first two days of starvation, 60% to 80% cell death was observed. Notably, the measurements were taken from cells maintaining spindle shape morphology, representing surviving cells (Fig 7). By day 4, diffusion hindrance doubled, indicating restricted movement of GFP in starved HeLa cytoplasm. Cells obtain constant nourishment from nutrient exchange in culture media for growth and division. When cell media is exchanged with PBS, a stress-inducing environment is created. The results of these experiments suggest that diffusion in cell cytoplasm is hindered during prolonged starvation (in PBS), leading to increased H_{diff} experienced by GFP molecules.

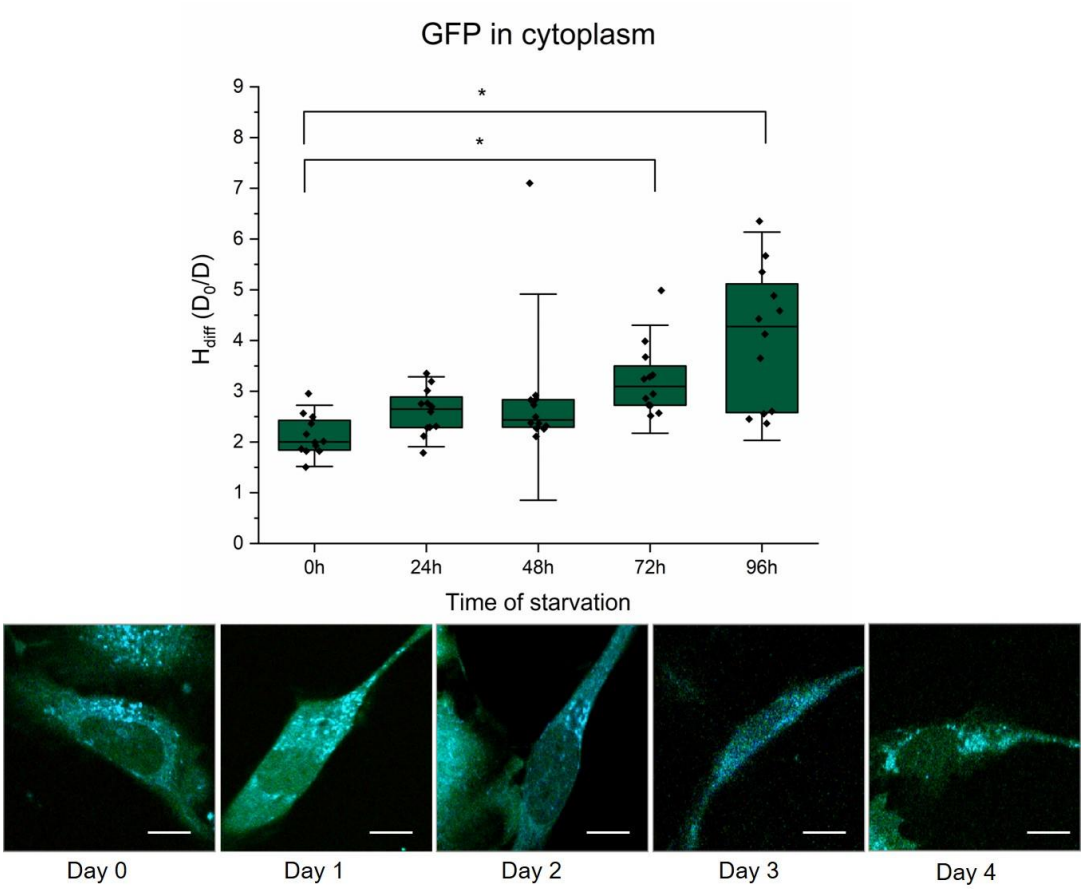

Figure 7: Diffusion hindrance (H_{diff}) measurements in cell cytoplasm over four days of starvation. Results are presented as box plots. Each bar represents averaged data collected from multiple cells with 5 measurements each/30s exposure time. The error bars represent the standard error of mean in all plots. Diffusion hindrance is calculated as a ratio of diffusion coefficients of GFP during starvation (calculated from time of flight) upon diffusion of GFP in water. FLIM images of HeLa-GFP cells during starvation over 4 days are shown at the bottom (from left to right). 2 sample variance Ttest was performed with *p>0.05. Scale bar: 50 µm.

2.1.2.2 Diffusion of ribosomes in cytoplasm during starvation

Additional experiments were performed with ribosomes as probes (different in size than GFP) to determine the viscosities in the cytoplasm in YO-PRO1 stained cells during starvation. YO-PRO-1 dye is a known DNA intercalator[96]. However, recent evidence has proved binding interactions of YO-PRO-1 with dsRNA as well[97]. Cells were briefly stained with 50 nM YO-PRO-1 dye, and dye uptake was confirmed using confocal imaging. YO-PRO-1 stained cells were used to measure rotational and translational diffusion of 60S or large subunit (15 nm) and 40S subunit or small subunit (3.75 nm) in cytoplasm under glucose-depleted conditions over four days. FCS curves obtained from the measurements were analysed using a 2-component free diffusion model[98]. These experiments were performed with the help of Dr. Karina Kwapiszewska.

FCS curves obtained from measurements of ribosomes in cytoplasm revealed interesting results. Single spot measurements from starved Yo-Pro-1 stained cells resulted in extensive photobleaching till ~2 minutes before the fluorescence intensity signal stabilised. Control cells (unstarved) stained with Yo-Pro-1 dye exhibited negligible photobleaching, as shown in Fig 8. After examining the FCS curves, it became clear that there might be two different populations (Fig 8) – with a freely diffusing component and an immobile component. As mentioned before, cytoplasm behaves differently for probes of different sizes. It might be possible that the LSU (15 nm) got immobilised in the cell cytoplasm, thus experiencing extensive photobleaching. The other mobile fraction with diffusion time >100 µs could potentially be small subunits (SSU) – which were not detectable in the presence of LSU due to a low degree of staining. In nutrient-deprived conditions, cytoplasm might undergo a change in pore size, decreasing from 100 nm to 30 nm. The diffusion coefficient obtained (~18 $\mu m^2/s$ on day 1) after fitting the data with 1 component model seems too big for a molecule of 15 nm in size. Along with photobleaching, this could indicate the immobilisation of LSU in starved cells, as predicted. YO-PRO-1 also binds to tRNA (2 nm), but because it is a small molecule (smaller than GFP – 2.3 nm), its expected diffusion coefficient should be higher. Therefore, the identified diffusing object could be predicted to be a small ribosomal subunit (40S), 3.75 nm in size. FCS curves were obtained in the subsequent days, keeping in mind that the freely diffusing particle is SSU (Fig 9).

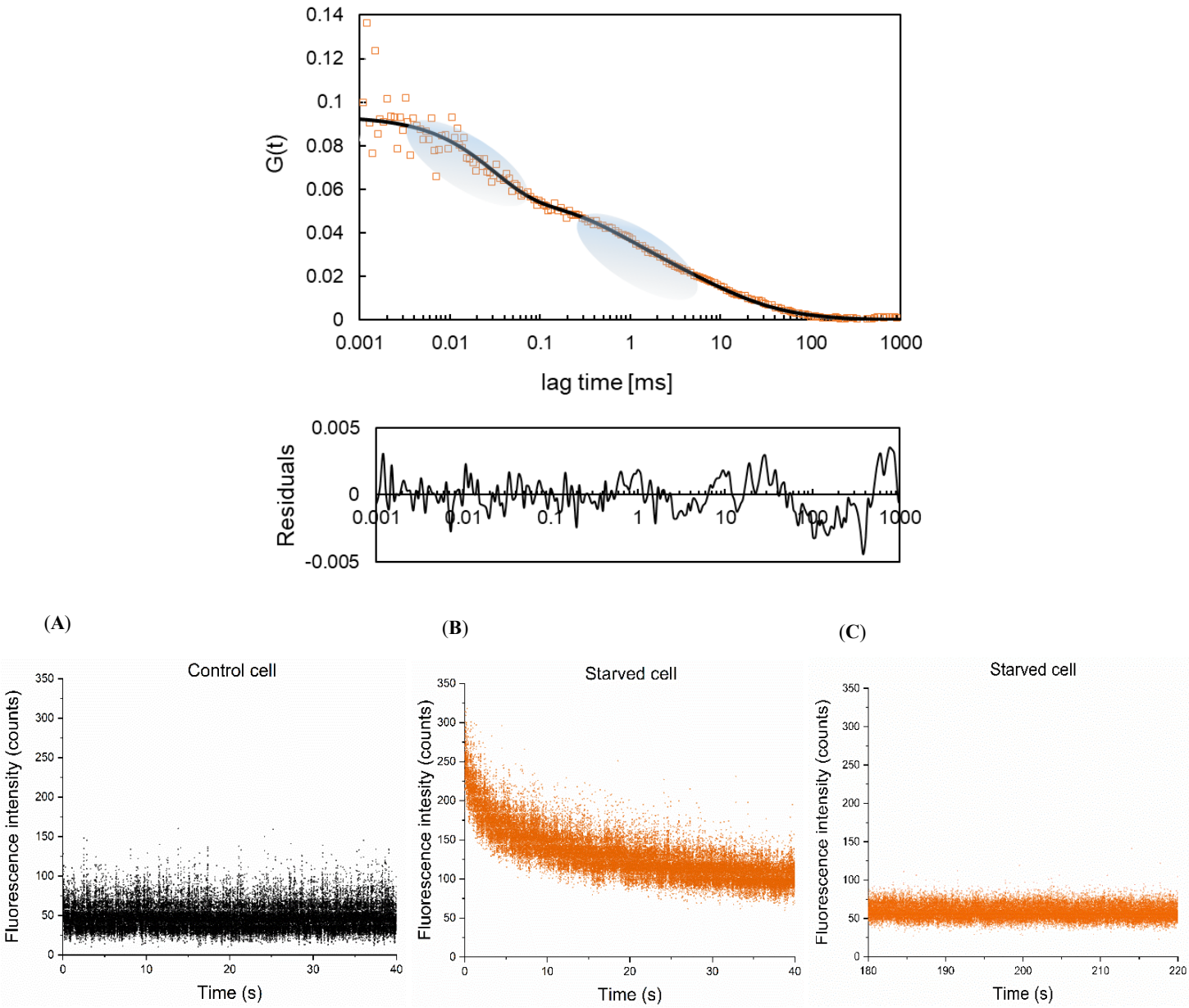

Figure 8: FCS measurements in cytoplasm with YO-PRO1 stained cells. The characteristic curve obtained for translational and rotational diffusion of YO-PRO1 stained ribosomes fitted with a 1-component diffusion model (blue shades). Time trace data analysis revealed a stable signal in control cells, indicating freely diffusing objects (A). However, photobleaching (B) indicates an immobile fraction of fluorescent molecules. (A) control cell (complete medium), (B) 96 h starved cell (0-40 seconds of measurement), (C) 96 h starved cell (the same cell, 180-220 seconds of measurement).

Diffusion hindrance for SSU (3.75 nm) increased from 3 $\frac{D_0}{D}$ on day 0 (here, the reference probe of the same size was measured– 20 kDa dextran[25]) to 13 $\frac{D_0}{D}$ on day 4 (Fig 9). Notably, a similar trend was observed for GFP over four days of starvation. However, SSU experiences a steeper increase in diffusion hindrance than GFP in a starved cell environment.

It was observed that the changes in diffusion hindrance were more pronounced for 40S ribosomal subunits (3.75 nm) than those of GFP (2.3 nm) (Fig 9). This suggests how a small change in probe size affects the molecular mobility inside cell cytoplasm under extreme stress conditions such as prolonged starvation (Fig 9).

2.1.3 Measuring diffusion in HeLa cell nucleus

2.1.3.1 Diffusion of GFP in nucleus during starvation

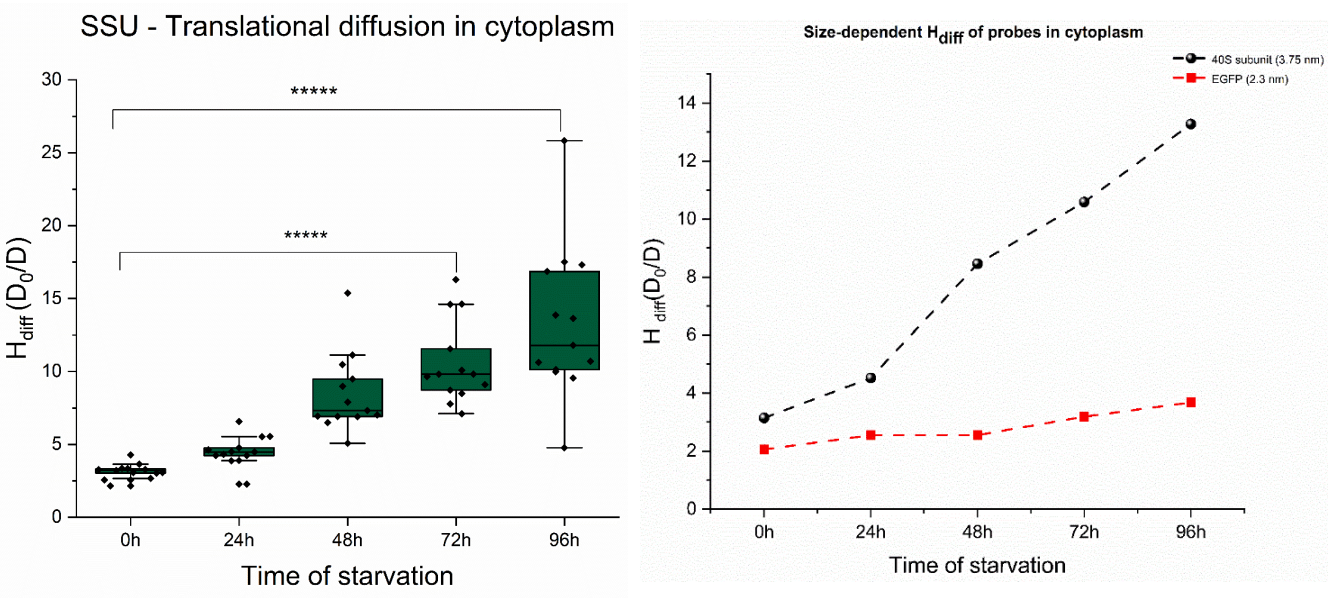

Figure 9: Translational diffusion (H_{diff}) of 40S small ribosomal subunit (SSU) in cytoplasm. Each bar represents data collected from 4-5 different cells, with 5 measurements each and an exposure time of 0-180 seconds. 0h bar plot shows diffusion hindrance for dextran of radii 3.75 nm in cell cytoplasm in unstarved Hela cell (equal in size to 40S ribosomal subunit). Error bars represent the standard error of mean. Two sample variance Ttest was performed (*****p values >0.00001). The line graph shows a comparison of H_{diff} measurements from two probes of different radii – GFP (2.3 nm) and ribosomal SSU (3.75 nm).

As mentioned in the introduction, distinct cellular compartments may exhibit differing levels of diffusion hindrance under stress conditions. Therefore, further measurements were performed in the nucleus. The nucleus is the command centre of a cell. Double-stranded DNA has survived millions of years and has predominantly emerged as a molecule of utmost significance due to its continuous repeatability, stability, and diversity[99]. Cells have mechanisms in place to protect their nuclear compartments during stressful conditions[100]. Diffusion coefficients of GFP molecules were measured in the nucleus of HeLa cells for four consecutive days of starvation. No significant changes in diffusion hindrance were observed in

the nucleus over the course of starvation, except on day 0 and day 4. (Fig 10). These observations highlight that the diffusion hindrance remains unaffected under stressful conditions of starvation in the cell nucleus. This implies that the nuclear compartment of the cell does not undergo any major transitions in its fluidic nature during stress when compared with the cytoplasm. Since the nucleus functions as the cell's control centre, unaffected diffusion hindrance may be an adaptive defence mechanism by which the cell preserves its most vital organelle under stress conditions, thereby maintaining its physiochemical properties. I want to point out the conservation of nanoviscosity values for GFP in HeLa cell nucleus in my study were similar to those found in another study, where diffusion of GFP is less sensitive to crowding effects and its relative mobility (compared to larger probes) remains conserved across various environments [101].

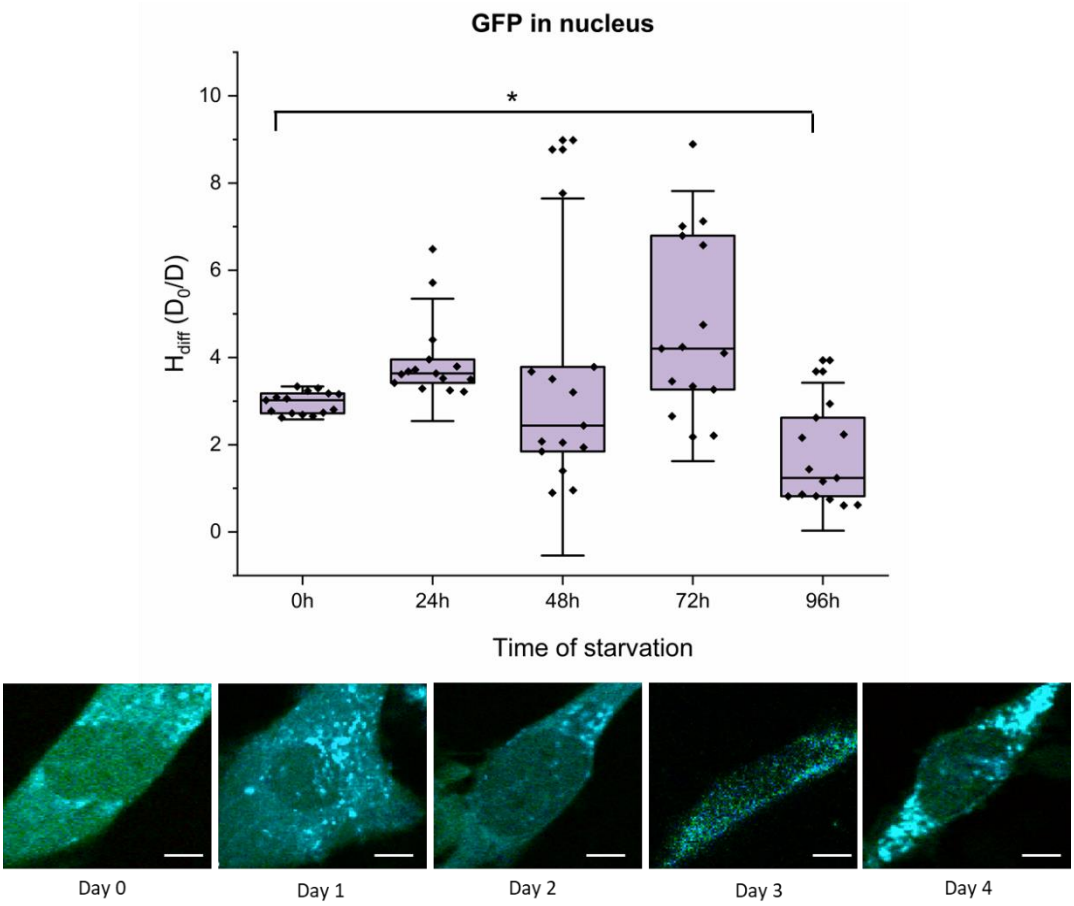

Figure 10: Diffusion hindrance (H_{diff}) measurements in cell nuclei over four days of starvation. Results are presented as box plots. Each bar represents averaged data collected from multiple cells with 5 measurements each/30s exposure time. The error bars represent the standard error of mean. FLIM images of HeLa-GFP cells during starvation over 4 days are shown at the bottom (from left to right). 2 sample variance Ttest was performed with *p>0.05. Scale bar: 50 µm.

2.1.3.2 Diffusion of ribosomes in nucleus during starvation

Same as in cytoplasm, diffusion measurements were performed with ribosomes as probes in the nucleus. LSU (15 nm) experienced minimal diffusion hindrance during prolonged starvation, with rotational and translational diffusion remaining largely unaffected (Fig 11). This suggests a stable diffusion environment within the nucleus for probes above 3 nm. Notably, the diffusion environment of GFP (2.3 nm) in the nucleus was analogous to that of Yo-Pro stained ribosomes during starvation. This highlights the constant diffusion profile maintained in cell nucleus for probes ranging between 2-20 nm in size. Diffusion hindrance in the nucleus has proved to be relatively stable on different length scales. This could be a significant cell survival strategy to protect the cell's genetic material under stress conditions, ensuring survival.

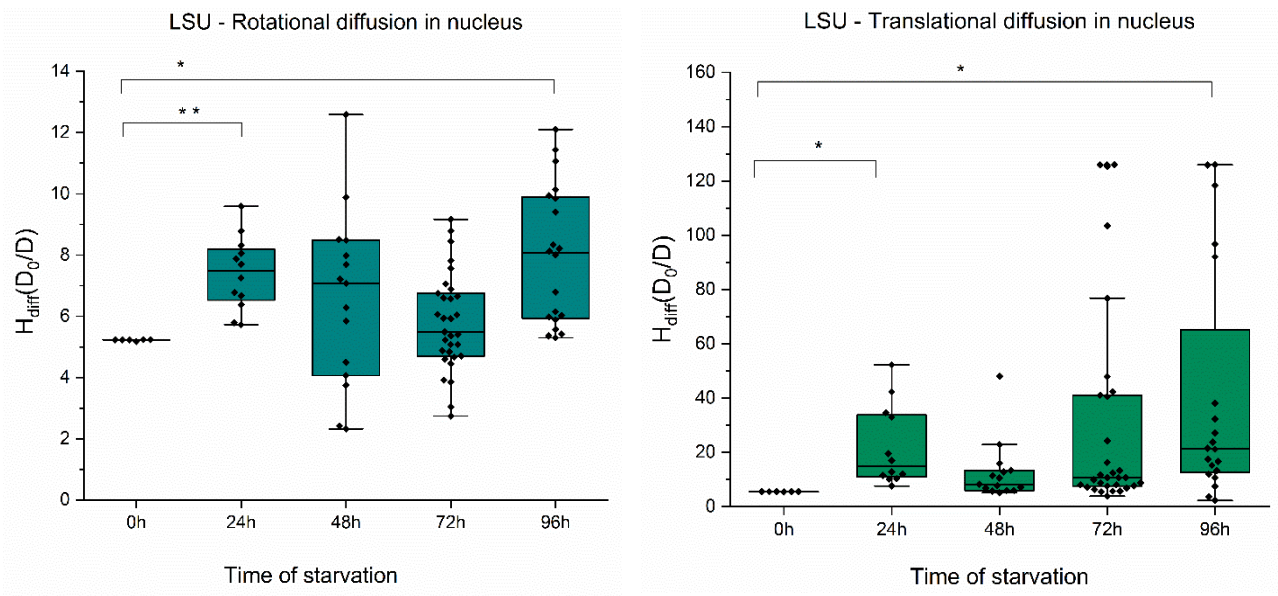

Figure 11: Diffusion hindrance (H_{diff}) experienced by large ribosomal subunit (60S) in HeLa cell nucleus during starvation using Yo-PRO-1 dye. (A) and (B) Rotational and translational diffusion of LSU in the nucleus. Each bar represents data collected from 5-10 different cells with 5 measurements, with an exposure time of 0-180 seconds. Error bars represent the standard error of mean. Two sample variance Ttest was performed (*p values >0.05, **p values >0.001).

Viscosity measurements at the microscale within live cells are highly compartmentalised, with significant variations observed between cytoplasm and different organelles such as endoplasmic reticulum, Golgi, and plasma membrane[102]. In my studies, I observed that this compartmentalisation extends to the nanoscale. Nanoviscosities measured in the nucleus and cell cytoplasm were different under starvation. These findings highlight that viscosity is not

uniformly distributed across cellular compartments and can fluctuate based on physiological conditions.

2.1.4 Volume changes during cellular starvation

70% of the intracellular space is occupied by water[103]. Without water, life would not have been possible on earth. Studying water movement in and out of cells is crucial for understanding its role in regulating cellular functions. Cells are dynamic systems. Water regulation through volume homeostasis is essential for maintaining proper intracellular balance and cellular integrity.

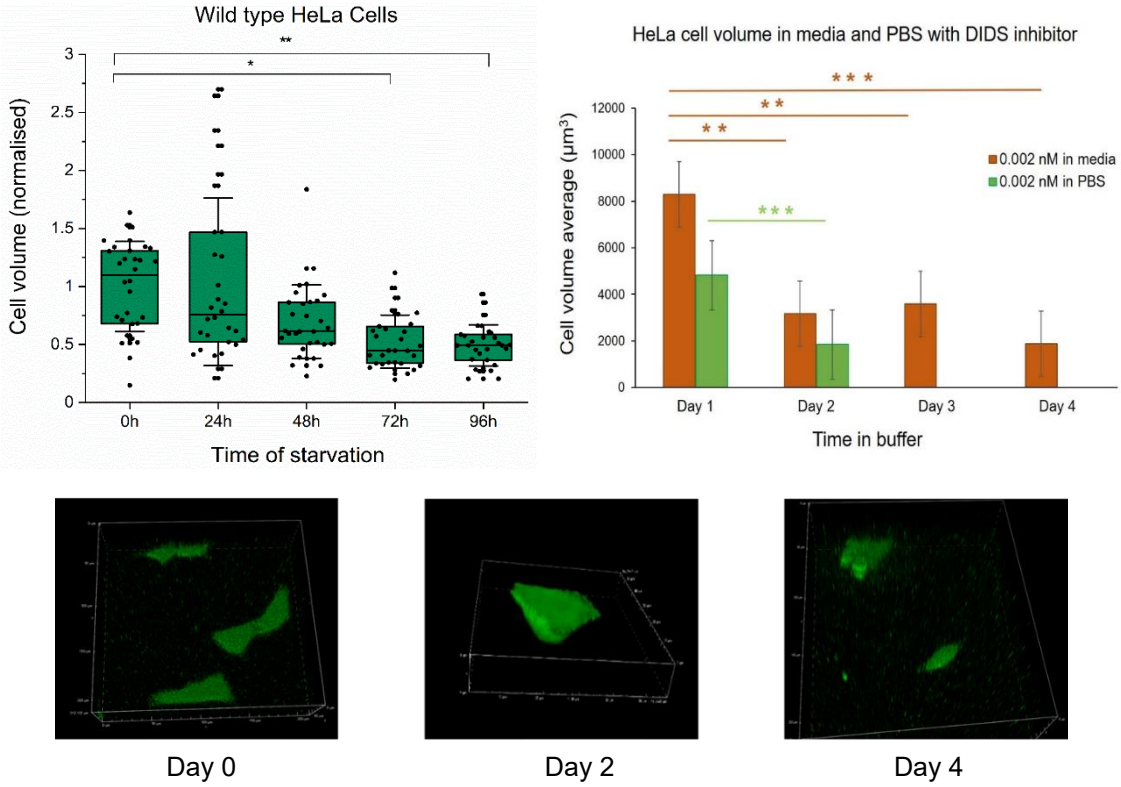

Figure 12: Measuring volume change in HeLa-GFP cells during starvation. HeLa-GFP cells were examined under a confocal microscope and excited with a GFP laser (488 nm) to perform a z-stack analysis of the cell (box plots). Results for volume change with DIDS inhibitor are shown with the help of a column graph. Approx. 0.3 µm/z-step, 11 µm area around the cell was covered from top to bottom in 20 seconds for both starved and un-starved cells. This 3D- imaging of cells was used to calculate the change in the volume of cells on the glass bottom slide. Each bar represents normalised values of volume (obtained from masking - in μm^3) for 10-30 cells during starvation. All cells still attached to the surface were measured. Z-stack masked images are presented below the graph (from left to right). Scale bar: 30 µm. Two sample variance Ttest was performed (*p values >0.05, **p values >0.005).

Over 4 days of starvation, a remarkable 50% cell volume reduction was measured in cells from day 0 to day 4 (Fig 12). A decreasing trend in cell volume throughout prolonged starvation proves water efflux from cells under stress (discussed in section 2.1.6). Cell volume perturbations can result from chronic or acute changes in and around cells and are influenced by changes in osmolarity, membrane potential, and plasma membrane channel activations[104]. Many channels, including aquaporins and CLC-based channels, maintain internal cell volume homeostasis and fluid secretion[105]. One such important channel is CLCNKA. 4,4'-Diisothiocyanatostilbene-2,2'-disulfonic acid (DIDS) is an inhibitor of this channel and its subtypes[106]. DIDS (stock – 25 mg; working concentration – 30 mM) inhibitor was used to block the anion channels in the cell membrane to check the water efflux response in cells during starvation. The concentration of inhibitors was collectively chosen from literature search[107] and the MTT assay performed in the lab. The MTT assay showed that 0.002 nM of DIDS shows 100% cell viability after four days in cell culture media (data not shown). The same concentration of DIDS in PBS (starvation conditions) was also analysed.

The volume changes in media, and PBS with 0.002 nM DIDS inhibitor was evaluated using confocal microscopy. On day 1, cells treated with 0.002 nM DIDS in media (Fig 12, orange bars) show a higher average cell volume than those treated with 0.002 nM DIDS in PBS (Fig 12, green bars). This could suggest that cells in media are likely more viable and healthy, allowing them to maintain a more adequate cell volume. By day 2, a marked reduction in cell volume is observed in both groups, with the cells in PBS showing a significant decrease (Fig 12). This reduction indicates that the cells in both conditions are experiencing stress, but cells in PBS are more affected. By day 3 and day 4, cell volume reduction continues for cells in media with the inhibitor, whereas cells in PBS with inhibitor die. Therefore, their cell volume could not be measured and is not shown. Blocking of the CLCNKA channel significantly affected cell volume in both media and PBS. Thus, the effect of CLCNKA channel knockout on volume homeostasis and GFP diffusion in cytoplasm will be discussed further in Chapter 2.2.

2.1.5 Decrease in intramolecular crowder space in HeLa cells during starvation

With decreasing water content (volume change), intermolecular crowder space decreases in the cell cytoplasm, which could hinder particle diffusion. Increased water efflux could be a reason for the increase in H_{diff} observed for GFP in cell cytoplasm during starvation (Fig 7). To confirm this, I calculated the correlation between the change in volume % and the increasing nanoviscosity or diffusion hindrance in HeLa cells. Previous studies identified effective nanoviscosity as a function of length scales with changing parameters like "ξ"[24]. Eq. 7 was used to derive a relationship between changing ξ and cell volume (ξ is an average half distance between major crowders). Since ξ is the half distance between major crowders in cytoplasm, this will also change during cell volume change (Fig 13). The changes in ξ can be approximated with the equation:

$$\xi' = \xi_0 \sqrt[3]{\frac{V'}{V_0}} \qquad \text{Eq.11}$$

The initial values of V and ξ are represented with the subscript "0", while values corresponding to post-cell shrinkage are distinguished using a prime symbol ($'$). With increasing water efflux, the gap between crowders (ξ) also reduces, bringing them closer to each other. Reduction in

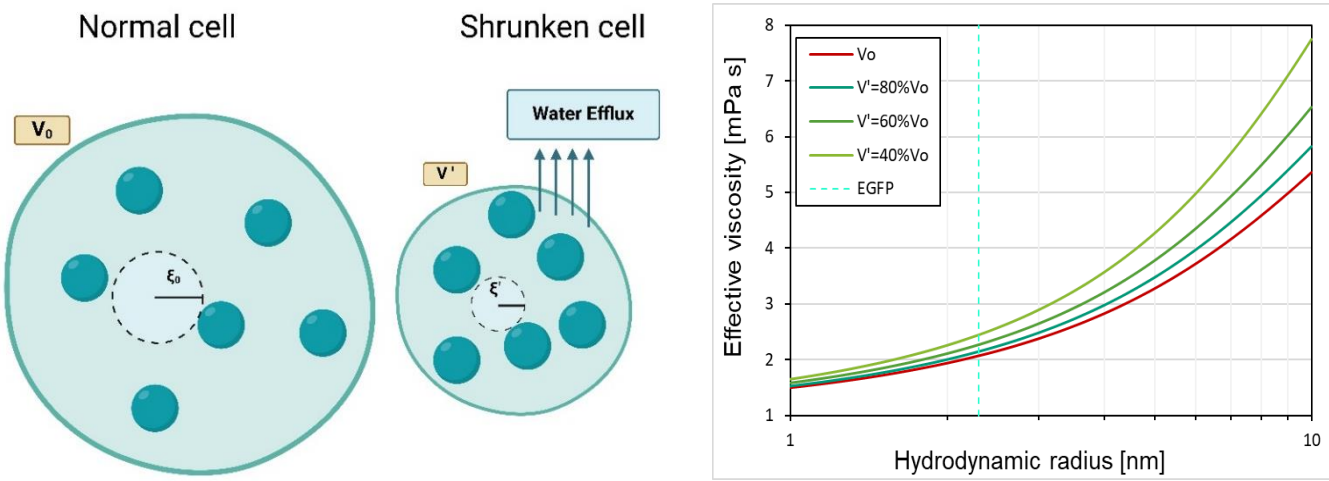

Figure 13: A schematic representation on the left represents the influence of volume change on viscosity in cells. Normal cell (left), holds a volume V_0 filled with molecular crowders (green circles) of an average radii. The average half-distance between these crowders has been described as ξ_0. When water efflux happens during volume change (V'), the cell shrinks (right), leading to a reduction in the average half distance between the crowders (ξ'). Meanwhile, the number and size of the crowders remain the same. H diff depends on ξ, as explained in eq.7. Reduction in ξ gives rise to increased H_{diff}, following eq.7. The line graph on the right illustrates the relationship between water efflux and changes in diffusion hindrance or viscosity in starved HeLa cells. Changes in ξ' correspond to the resulting volumes (V'), expressed as a percentage of the initial volume V_0. A dashed line shows the hydrodynamic radius of GFP.

the average distance between these crowders, in turn, affects the viscosity of the cell cytoplasm. The impact of cell shrinkage on effective viscosity (η_{eff}) in HeLa cells is presented in Fig 13.

2.1.6 Changes in interaction parameter

For theoretical determination of cytoplasmic viscosity during starvation, Eq. 7,8,9 and 11 were used, which took into account the cell volume measurements and predicted changes in intermolecular spaces. Changes in ξ_1 to ξ_2 were further employed to calculate the H_{diff}. H_{diff} calculated theoretically was different from the FCS measurements (Table 3). Although I found a correlation between water efflux and changes in measured H_{diff}, the discrepancy in calculated and measured values could not be explained solely by changes in ξ. Therefore, additional interactions in cell cytoplasm was explored.

Table 3: Values of calculated and measured H_{diff} of GFP in cytoplasm

Time of starvation	Calculated H_{diff}	Measured H_{diff}
0 h	2.1	2.1
24h	2.2	2.5
48 h	2.2	2.6
72 h	2.3	3.2
96 h	2.3	4.5

I hypothesised that water efflux from the cells would lead to molecules coming together, decreasing the available intramolecular crowder space (ξ). As freely diffusing molecules come close to each other, they should experience increased interactions. The interaction parameter or γ characterises the interactions between particles in a system. It is a measure used in thermodynamics to quantify the extent by which molecular interactions deviate from ideal behaviour in a system[108]. In this study, γ refers to probe interactions with molecular crowders in cell cytoplasm or energy required to overcome resistance between probe and crowders. The energy of a complex fluid largely depends on these internal interactions. Therefore, the length scale-dependent viscosity model was employed to study the diffusion coefficients and γ [109] in a nanoscale system.

As described in the model by *Sozanski et al.*[109] for proteins in polymer solutions, the changes in diffusion coefficient in a complex fluid-like cytoplasm can be expressed as;

$$D = D_0 exp\left[\frac{-E}{RT}\left(\frac{R_H}{\xi}\right)^a\right], \qquad \text{Eq.12}$$

D_0 = diffusion coefficient of the probe in water in the temperature T, D = diffusion of the probe in the cytoplasm, R_H = hydrodynamic radii of crowders, E = interaction parameter called, "γ" , ξ = intermolecular space, *a* – exponent from length-scale dependent viscosity curve, R – the gas constant, T – temperature [K].

Keeping the hydrodynamic radii of major molecular crowder the same, we assume a detectable change in diffusion coefficients from D_1 (probe in control, native cells) to D_2 (probe in a cell subjected to water efflux), γ parameter can be calculated for day 0 starvation as:

$$\frac{D_1}{D_0} = exp\left[\frac{-\gamma\left(\frac{R_H}{\xi_1}\right)^a}{RT}\right], \qquad \text{Eq.13}$$

ξ_2 results from removing water molecules from the cell cytoplasm, decreasing the intermolecular space from ξ_1. Correlating changes in diffusion coefficient with change in energy, we get,

$$\mathrm{RT}\ln\left(\frac{D_1}{D_0}\right) = -\gamma\left(\frac{R_H}{\xi_2}\right)^a, \qquad \text{Eq.14}$$

$$-\left[\mathrm{RT}\left(\ln\left(\frac{D_1}{D_0}\right)\right)\left(\frac{R_H}{\xi_2}\right)^a\right] = \gamma_1 \qquad \text{Eq. 15}$$

$\gamma 1$ [kJ/mol] changes with changing "D" and "ξ" ($\xi 1$ to $\xi 2$ - calculated separately for all days of starvation).

ξ_1 – size parameter from length-scale dependent viscosity curve,

ξ_2 – size parameter calculated from volume change (from V_1 to V_2) experiment, from

$$\xi_2 = \xi_1 \sqrt[3]{\frac{V_2}{V_1}} \qquad \text{Eq.11}$$

D_1 – diffusion coefficient of the probe measured in native cells,

Table 4 provides calculated values for the change in interaction parameter with respect to the change in intermolecular crowder space during prolonged starvation.

Table 4: Change in interaction parameter (γ) in HeLa cells during starvation for EGFP (2.3 nm)

Day	Comment	ξ [nm]	γ [kJ/mol]
Day 0	Native cell	3.2	0.7
Day 1	24h starvation	2.0	0.7
Day 2	48h starvation	2.8	1.0
Day 3	72h starvation	2.6	1.2
Day 4	96h starvation	2.5	1.3

2.1.7 Morphological changes in 769-P cells during starvation

To observe the changes in cancer cells during nutrient deprivation, the morphology of 769-P cells under a confocal microscope. An altered glucose metabolism causes cellular stress and potentially influences cell morphology, survival and proliferation. These effects have been documented in 769-P cells[110]. Therefore, this cell line was chosen to perform morphology-based experiments during nutrient-deprived conditions. For this study, the MALIONR genetic nanosensor (discussed in section 4.2.1) was transfected in 769-P cells to study the ATP consumption over a period of glucose starvation (cell line was chosen to highlight the effect of glucose depletion on major organs like the kidney, which is the parent source for these cells. Refer to Appendix B.3, B.4 for plasmid isolation (MALIONR) and transfection protocol.

Cells starved till 21h showed no further increase in growth rate. After 21h, a decrease in fluorescence intensity of MALIONR was first recorded. Cell-cell anchorage was broken after 40h in PBS, and cells formed macropinocytotic cups (Fig 14). After 72h of starvation, membrane blebbing was noticed, and cellular appendages (finger-like projections) were visible. These helped cells to increase their mobility in the solution (probably looking for resources from other cells or in the solution to get replenished). After 90h of starvation, 90% of the cells became circular and were motile, with finger-like projections visible from the membrane.

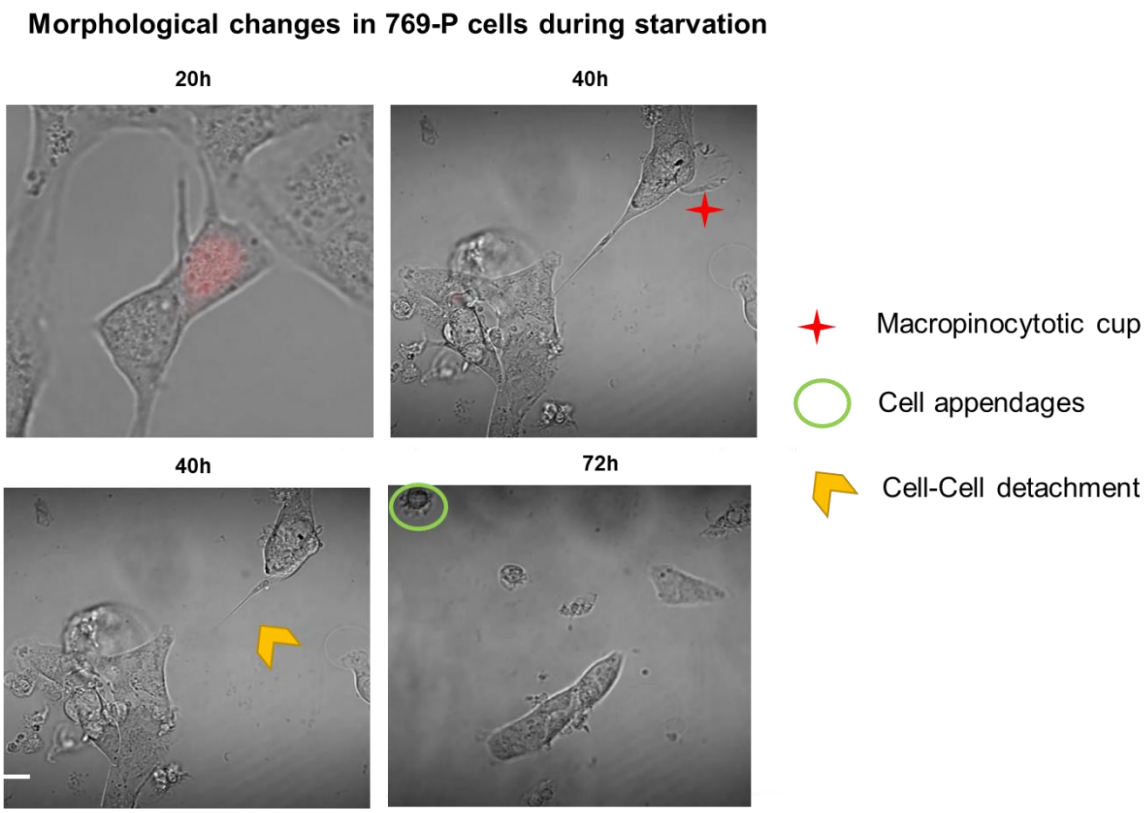

Figure 14: Confocal images of 769-P cells at 60X. 769-P cells transfected with MALIONR plasmid containing gene sequence of ATP synthase protein where, F_0F_1-ATP synthase protein fluoresces after binding with intracellular ATP in cells[122]. Cells were imaged for 96 h in phosphate saline buffer (without glucose and other cell nutrients). ATP-dependent fluorescence is reduced drastically by the end of 30h. 40h after starvation, a macropinocytotic cup could be seen (red star). The cell-cell attachment was broken after 40h of starvation (yellow arrow). Around 72h of starvation, cell appendages could be seen (green circle). These appendages helped in increased cell motility. Scale bar: 60 µm.

2.1.8 Cell re-growth in media after prolonged starvation

Studies suggest that cancer cells undergo a dormant state of energy conservation under stressful conditions[111,112]. Many single-cell organisms like bacteria and yeast have also been found to adopt similar survival mechanisms. A population study was conducted to observe cell behaviour during starvation,. Before starvation began, bright-field images were taken from three specific areas in two glass slide wells where cells had been pre-seeded. The procedure was repeated to capture images on day 0, day 2, and day 4 of the starvation period. After four days of starvation, the cell medium was changed from PBS to complete DMEM media containing growth factors. A similar imaging procedure was used to document changes on day 5, day 7, and day 9. By day 4, many cells had detached from the surface and were floating in PBS as debris. After four days of starvation, the PBS containing cell debris was collected and

centrifuged at 1100g for 5 minutes. The supernatant was discarded, and the pelleted cell debris was resuspended in fresh, complete growth media. This resuspended media containing cells was transferred to another 35 mm glass slide. A similar media change was applied to the original slide, which contained the remaining 1% of cells still attached to the surface. The few remaining cells on the original slide reached 60% confluency within three days of culture in complete media containing growth factors (Fig 15). Cell growth was also observed in the slide containing resuspended cell debris in complete media.

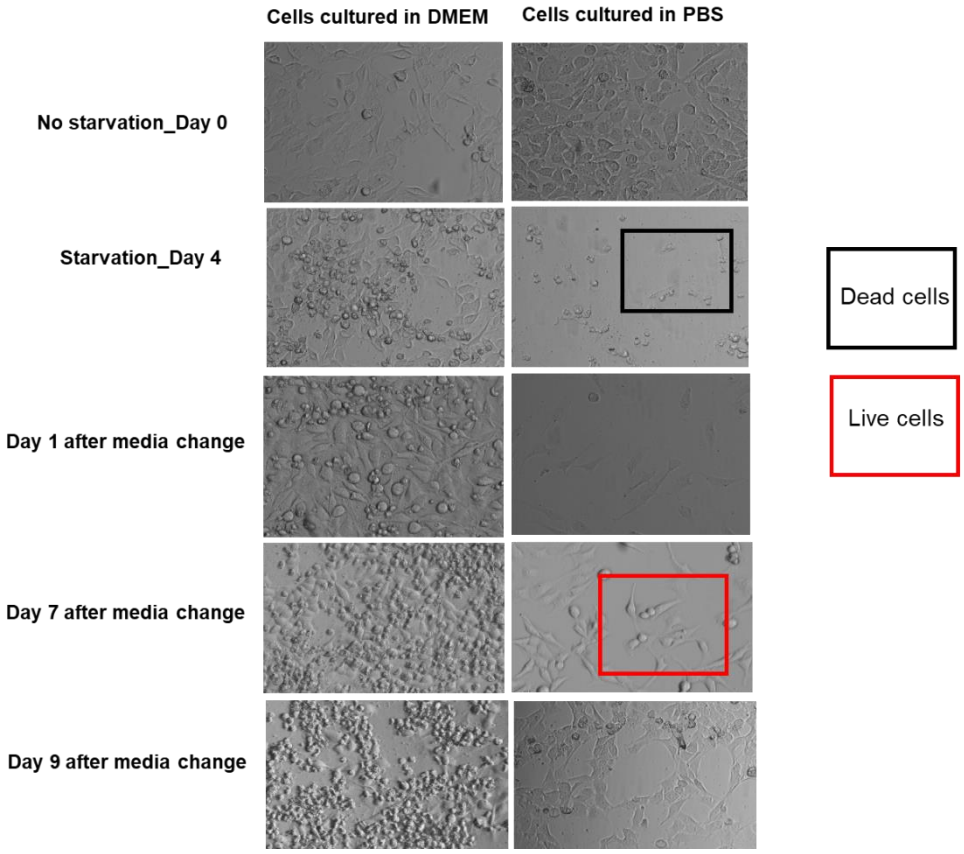

Figure 15: Starvation panel of HeLa GFP cells. Cells were starved in PBS for 4 days and re-cultured in complete growth media after starvation. Cells in PBS well started growing on day 1. Cells were starved in PBS for 4 days and re-cultured in complete growth media after starvation. Cells started growing on day 5 and continued their growth till day 9. Scale bar: 20 µm.

These observations suggest that starvation is highly stressful for mammalian cells, leading to water loss and cell shrinkage (or near-death states). They can enter a dormant state and reactivate when nourishment becomes available (Fig 15).

2.1.9 Conclusion

I measured changes in diffusion coefficients of GFP (2.3 nm) and ribosomes (LSU – 15 nm, SSU – 3.5 nm) inside HeLa cells under prolonged starvation. GFP diffusion hindrance increased during prolonged starvation, along with a 50% reduction in cell volume. This decrease in cell volume was attributed to water efflux, which was further linked to increased intracellular viscosity and reduced intermolecular space in cell cytoplasm. Theoretical and measured values of GFP diffusion showed deviations, which were explained by changes in interaction parameter. The interaction parameter (γ) increased due to increased interactions and reduced intermolecular crowding from 3.2 (ξ_1) to 2.5 (ξ_2). 40S subunits (3.75 nm) were also measured in cytoplasm. The increased diffusion hindrance during starvation demonstrated that probes smaller than 5 nm, such as GFP (2.3 nm) and 40S subunit (3.75 nm), experience enhanced diffusion hindrance under similar conditions. Furthermore, measurements of D in the nucleus showed a compartmentalised viscosity in starved cells. Cell nuclei exhibited negligible variations in diffusion hindrance towards GFP and ribosomes during starvation as opposed to cytoplasm. From these studies, it was inferred that under stress conditions, cells maintain an undisturbed nuclear state in terms of diffusion of particles at the nanoscale. Notably, cytoplasm mesh pore size changed from 100 nm to 30 nm when stress was increased. This transition is not unique to mammalian or cancer cells. A similar response has been reported in unicellular organisms like yeast and bacteria[113]. Therefore, it is plausible to suggest that such stress adaptations may be evolutionarily conserved across single-cell and multicellular organisms.

Cancer cell resilience to starvation was also studied qualitatively. Starved cells were re-cultured in complete media to assess recovery in size and number. After 3 days in complete media, starved cells demonstrated 60 % confluency. This indicates that cancer cells enter an inactive state under stress conditions and resume growth when conditions improve.

2.2 Cellular nanoviscosity in CLCNKA knockout cells

2.3 CLCNKA gene knockout

In my previous chapter, I reported a study on the effect of a chloride channel inhibitor targeting the CLCNKA channel. In this chapter, I present the continuation of that study. Chloride channel proteins, or the CLC family, constitute a group of transmembrane anion channels. These channels are expressed in plasma and intracellular membranes of cells in most living organisms[114]. CLCs like CLC-ka proteins are involved in significant physiological processes such as voltage-gated channel activity, signal transduction, transepithelial transport and cell volume homeostasis[115]. CLCNKA gene coding for this protein is highly prone to small genetic variations, causing structural and functional changes in the resultant protein. Mutations in these genes are associated with various human diseases called channelopathies[116,117]. Membrane proteins make up 30% of all proteins in the human genome[118]. 60% of current drug targets thus focus on membrane channel proteins. CLCNKA gene knockout was created to study biophysical alterations in wild-type HeLa cells ($HeLa_{wt}$) under nutrient deprivation. Results were analysed to correlate changes in macromolecular crowding with cell volume (similar to $HeLa_{wt}$). The knockout cell line was created at the genetics division of Harvard Medical School, Brigham and Women's Hospital.

2.3.1 Knockout cell preparation and confirmation

Fig 16 describes a CRISPR-CAS9 gene editing schematic for creating a HeLa knockout ($HeLa_{ko}$) cells. For the cell line preparation protocol, refer to Appendix B.6. The knockout was confirmed by next-generation sequencing (NGS) of the genomic DNA of the resultant clone. NGS data was analysed using an online tool namely – "crispresso". The results of the analysis are shown in Fig 17.

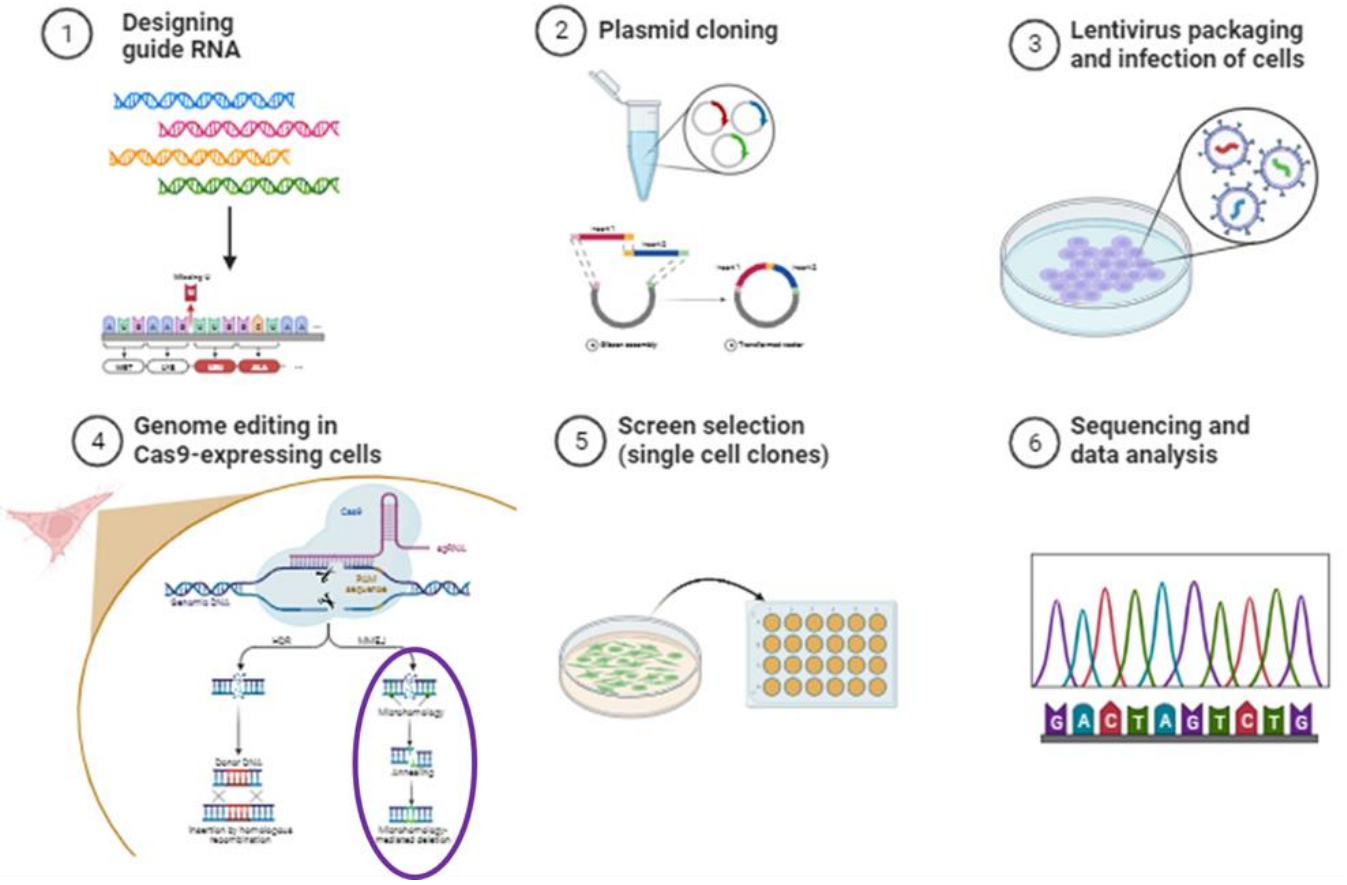

Figure 16: CRISPR-Cas9 editing protocol to create a knockout HeLa GFP cell line. (1) 4 gRNA sequences were designed using in-Delphi against the target gene, CLCNKA (chloride anion channel) (2) These gRNA sequences were cloned into a lenti-plasmid backbone. The sequence of the plasmid was confirmed using Sanger sequencing. (3) and (4) The plasmid was then transduced into $HeLa_{wt}$ to create a gene knockout. (5) HeLa clones were cultured in antibiotic-selected media after transduction. Clones positive for knockout were the only clones that survived. (6) gDNA from positive clones was isolated, and the sequence was confirmed using Sanger sequencing.

Multiple clones were analysed on crispresso. Distinctly, clone G4 analysis revealed that most identified reads exhibited modifications different from the parent clones. The pie chart on the left (Fig 17) shows the proportion of modified (63.28%) and unmodified (36.72%) reads, indicating that a significant fraction of the target DNA underwent modifications, demonstrating efficient genome editing by CRISPR/CAS9 system. The mutation position distribution plot on the right (Fig 17) shows the location of various mutations (insertions, deletions and substitutions) across the reference amplicon. A sharp peak at 70 bp on the reference amplicon highlights that the most modifications (in this case, insertions) occurred at this site. This is the expected site for CAS9-induced double-strand breaks. Below the position chart, the reference sequence is displayed alongside reads containing mutations (Fig 17). The reference sequence corresponds to the original DNA sequence targeted by the sgRNA, which directs CAS9 to the

cut site. The most frequent mutations involved guanine, covering 39.04% of all the reads. It was confirmed with 10,000 reads/base pair. This comprehensive analysis confirms that the CRIPSR-CAS9 system successfully created the CLCNKA knockout in HeLa GFP cells.

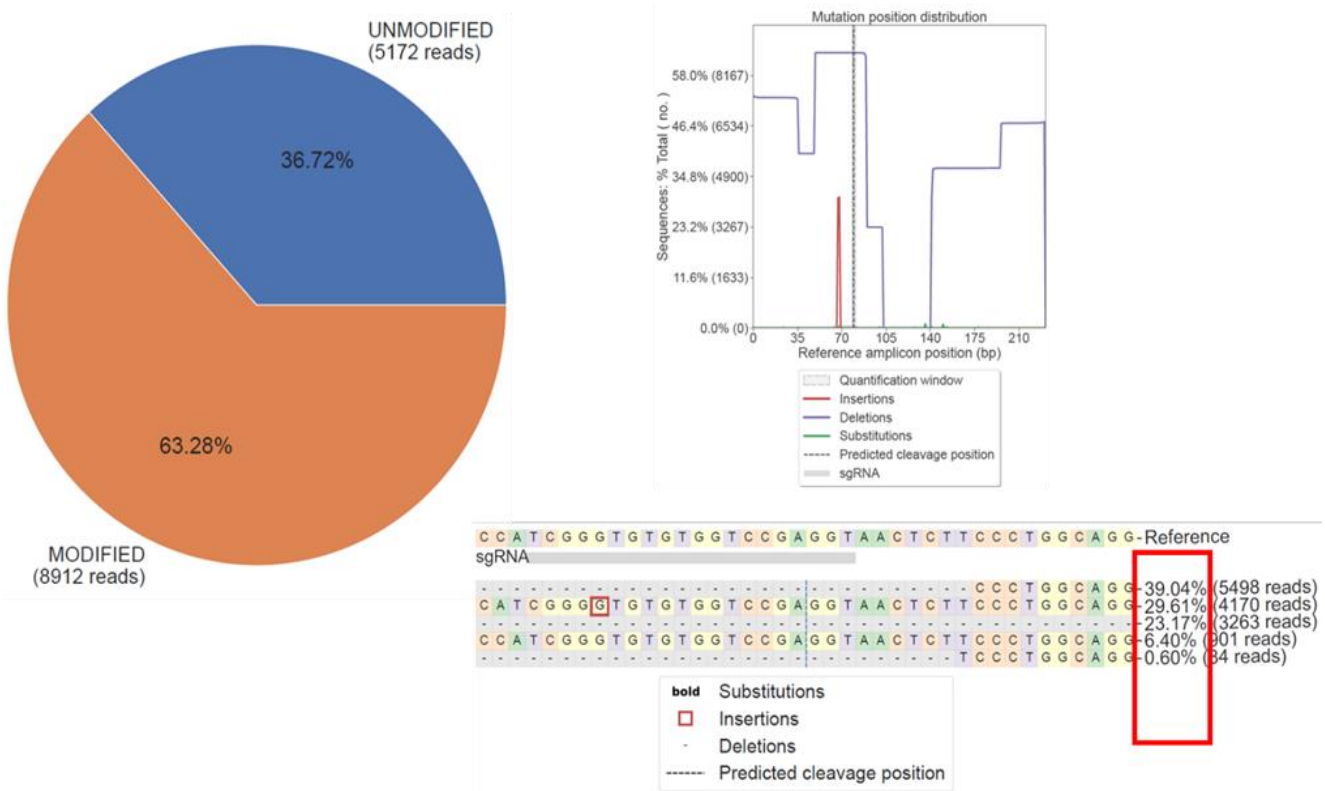

Figure 17: HeLa GFP clone was sent for NGS sequence to confirm the indels. The pie chart represents the number of reads done on a 230 bp of DNA from the clone. The red box identifies the type and total % of mutations created after editing.

2.3.2 Diffusion measurements during starvation in knockout HeLa cell cytoplasm

The time of flight of GFP was measured in 4-5 $HeLa_{ko}$ cells per day, with 5-10 measurements each (30s/measurement). Diffusion coefficients were calculated from the measurements using Eq.8,9. On day 0, cell media was exchanged with PBS, and measurements were taken immediately. The selection of a suitable physical model for fitting experimental data is necessary. In this analysis, two distinct models – simple diffusion and anomalous diffusion were used to fit the FCS data and investigate the diffusion behaviour of GFP molecules in the $HeLa_{ko}$ cells. The same FCS curves were fitted using both models to compare. The simple diffusion model was applied to test the classical assumption of uniform diffusion of GFP across cytoplasm, like in the $HeLa_{wt}$ cells. However, the simple diffusion model did not adequately

capture the observed diffusion of GFP in the $HeLa_{ko}$ cells, indicating that GFP diffusion was more complex (Fig 18). In contrast, the anomalous diffusion model provided a better fit for the observed data (better-fitted residues), suggesting that the diffusion of GFP molecules in the $HeLa_{ko}$ cells exhibits a non-linear behaviour (Fig 18).

In anomalous diffusion, the mean square displacement of the probe increases sub linearly with time (MSD $\propto t^{\alpha}$) in contrast to the linear relationship observed in simple diffusion[119]. The anomalous exponent (α) for probes in complex fluids like cytoplasm typically ranges between $0<\alpha<1$. This phenomenon was not observed in $HeLa_{wt}$ for GFP, where α is close to 1, equal to free diffusion. However, in $HeLa_{ko}$, $\alpha = 0.75$ was obtained from measurements coherent with the values of α observed in cytoplasm[120]. It is possible that the knockout induced changes in the nanostructure of the cytoplasm, resulting in anomalous behaviour of GFP within the cell cytoplasm. Anomalous behaviour of GFP could be due to additional membrane compartmentalisation upon knockout or interaction of GFP with other molecules. D values calculated for GFP on day 0 of starvation were ~50 $\mu m^2/s$ and ~30 $\mu m^2/s$ for wild type and $HeLa_{ko}$, respectively. These results are consistent with the observation that the effective diffusion coefficient in anomalous diffusion is lower than in simple diffusion due to hindrance in the free movement of the probe.

Interestingly, minimal fluctuations in GFP diffusion were observed in $HeLa_{ko}$ cells during prolonged starvation, with diffusion rates remaining consistently within the range of 30 to 40 $\mu m^2/s$ (Fig. 18). GFP experienced negligible diffusion hindrance during prolonged starvation (Fig 18). This suggests that starvation did not significantly alter the cytoplasmic structure or the diffusion behaviour of GFP in $HeLa_{ko}$, unlike the changes observed in wild-type cells, where prolonged starvation resulted in increased cytoplasmic viscosity and a decreased diffusion coefficient by day 4. Cell viability was assessed using calcein/PI staining in control and starved cells. Control cells cultured in media exhibited predominantly green fluorescence, indicating high viability, with only a few cells showing red fluorescence, suggesting compromised membrane integrity and potential cell death.

In contrast, starved cells displayed fewer adhered cells with green fluorescence, indicating viability, while floating cells exhibited red fluorescence, signifying cell death. Diffusion coefficient measurements were performed on cells exhibiting a spindle-shaped morphology (Fig.18).

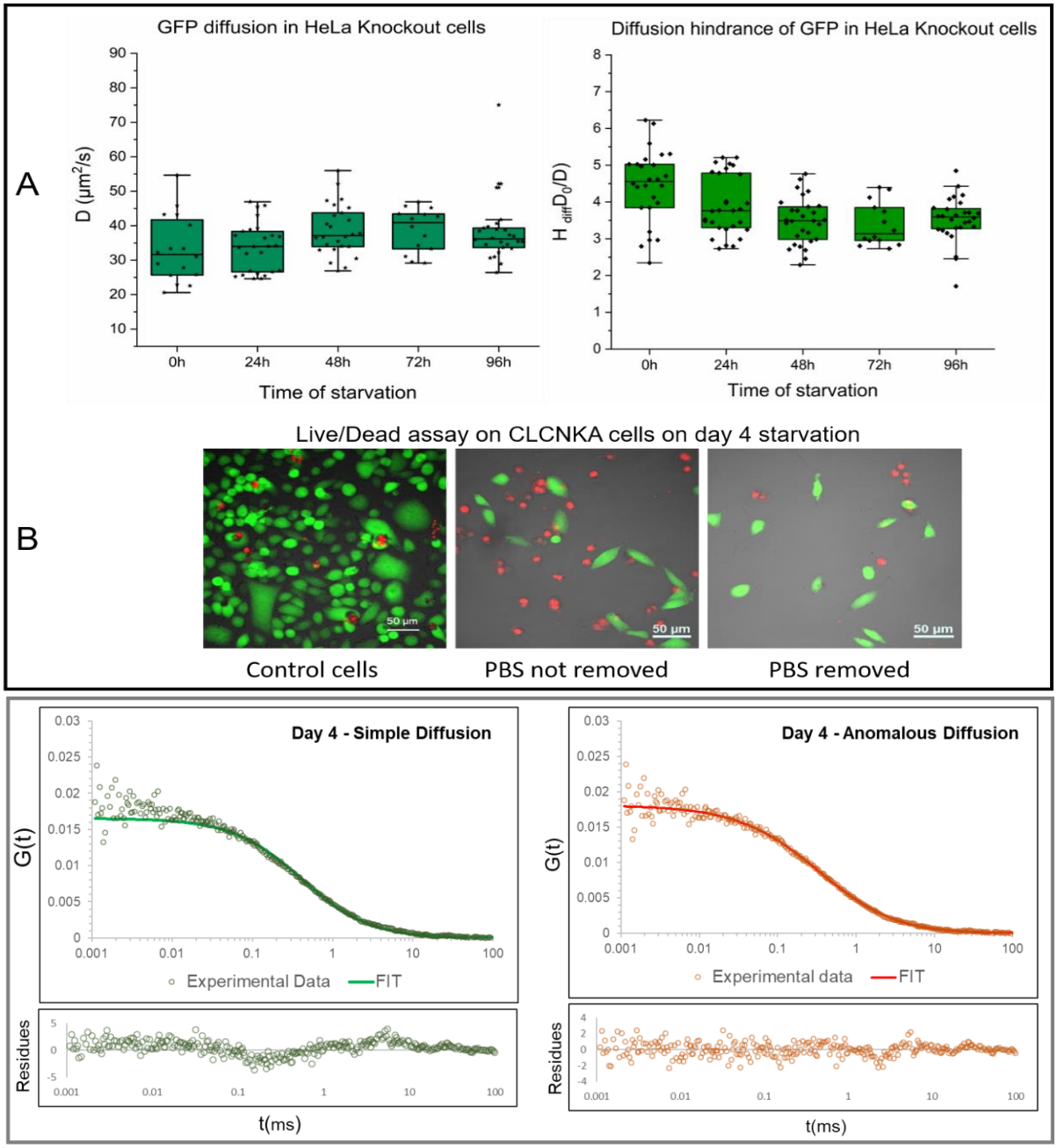

Figure 18: (A) shows the diffusion coefficient and diffusion hindrance of GFP in the $HeLa_{ko}$ cytoplasm during prolonged starvation, and (B) shows cell viability using calcein and PI dyes. Each bar represents readings from 5-4 individual cells, with 4 measurements each, for 30s/measurement. Error bars are standard deviation. 2 variance one-way ANOVA test was performed with a p-value at 0.00068. Below the graphs, the model fitting of diffusion coefficients obtained for cells during starvation has been shown (in the grey box). The figure compares the fitting results from the simple diffusion and anomalous diffusion models. The same FCS curves were fitted with 2 different models – anomalous diffusion model (red) and simple diffusion model (green).

2.3.3 Volume homeostasis in HeLa$_{ko}$ cells during prolonged starvation

For starved HeLa$_{wt}$, a decrease in diffusion coefficients was linked with a 50 % decrease in cell volume (Fig 19). For comparison, the volume of starved cells during starvation was measured in HeLa$_{ko}$ cells. HeLa$_{ko}$ did not exhibit water loss similar to that observed in HeLa$_{wt}$. Assuming the intracellular water content remains unchanged, the unaltered diffusion coefficients in HeLa$_{ko}$ compared to wild-type cells are consistent with this observation. Cancer cells employ various regulatory mechanisms to survive under extreme conditions, including acquiring mutations and upregulating survival signals, such as the downregulation of pro-apoptotic genes like bax and bak[121]. HeLa$_{ko}$ cells showed less variability in volume changes than HeLa$_{wt}$ cells, suggesting gene knockout altered volume homeostasis in these cells. The results support this hypothesis, as no significant changes were observed in GFP diffusion coefficients or cell volume during prolonged starvation in the HeLa$_{ko}$. This suggests that, unlike in wild-type cells where starvation induces alterations in both diffusion behaviour and cell volume, the HeLa$_{ko}$ maintain their cellular integrity and diffusion characteristics, likely due to the activation of these alternative survival pathways.

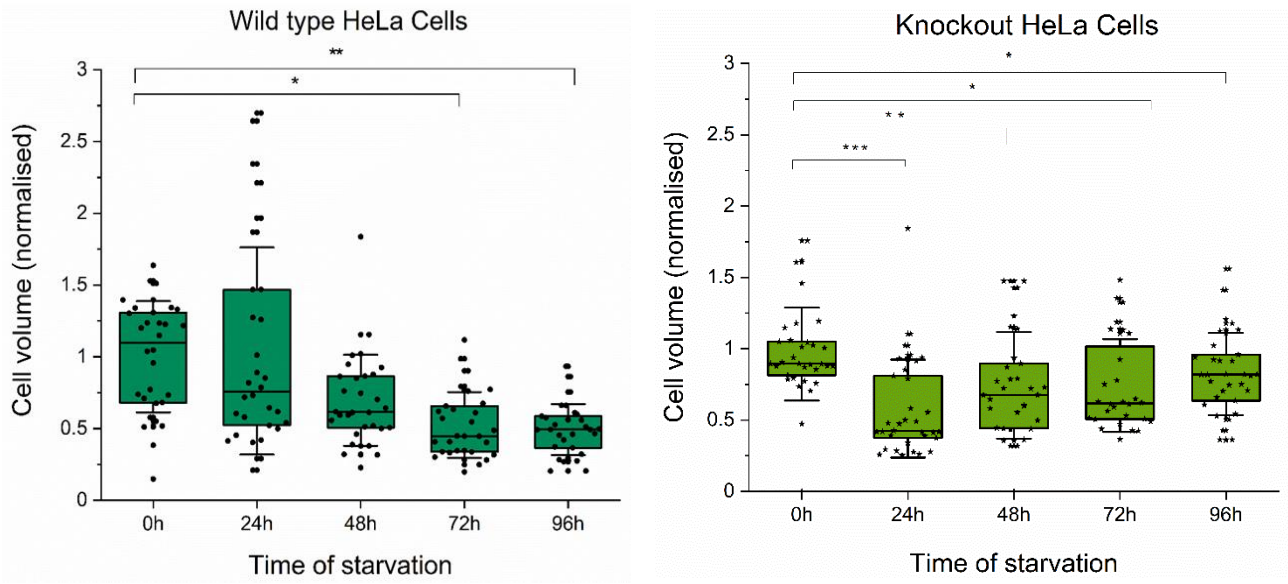

Figure 19: Cell volume changes in HeLa$_{wt}$ and HeLa$_{ko}$ cells. Each bar represents readings from 10-20 cells over prolonged starvation in PBS. Error bars represent the standard error of mean. HeLa-GFP cells were examined under a confocal microscope and excited with a 488 nm laser to perform a z-stack analysis of the cell for volume measurements (same as in previous experiments).

2.3.4 Conclusion

In $HeLa_{wt}$, altered diffusion of GFP in cell cytoplasm was associated with water loss during starvation. In the $HeLa_{ko}$, however, the results were different. No water loss was observed, which led to the assumption that the intermolecular distance between the cells remained the same, showing minimal to no effect on macromolecular crowding. The diffusion hindrance for GFP in $HeLa_{ko}$ did not increase over prolonged starvation, as was observed for $HeLa_{wt}$ cells. However, it was noticed that average diffusion coefficients of GFP in $HeLa_{ko}$, without any stress, were lower in the cytoplasm (~31 $\mu m^2/s$) and nucleus (~38 $\mu m^2/s$) (data not shown) when compared to the diffusion coefficient of GFP in $HeLa_{wt}$. This means that the movement of GFP was much more restricted in knockout than in wild-type HeLa in both cellular compartments. Since the intensity fluctuations of GFP molecules were recorded in the effective confocal volume of a few femtolitres, which spatially probes a small region within the cell cytoplasm, the restricted GFP movement might be non-uniform and localised. This hypothesis is supported by the anomalous diffusion of GFP molecules in the $HeLa_{ko}$ cells, leading to changes in the diffusion coefficient of GFP compared to the diffusion coefficients measured in the $HeLa_{wt}$ cells. Gene knockout in HeLa cells could contribute to this non-uniform behaviour of GFP in cell cytoplasm locally.

2.4 Cellular ATP depletion

ATP depletion is directly linked with glucose deprivation. The first two chapters focus on changes in biophysical properties intracellularly during starvation. Therefore, attempts were made to quantify ATP levels in glucose-depleted conditions.

2.4.1 Types of ATP sensors

ATP sensing is essential in understanding cellular energetics. More than 5000 articles have been published using currently available ATP sensors (Table 1) to quantify intracellular ATP levels. While these sensors are extremely valuable in research, finding a sensor for each project's unique set-up can be challenging. These challenges arise because identifying an ATP sensor remains difficult due to differences in sample complexity, sensitivity, specificity, dynamic ATP ranges across systems and the sensor's real-time monitoring capabilities. For this thesis, my goal was to quantify ATP concentrations in single cells, for which two types of

ATP sensors were selected – a genetic nanosensor (MALIONR) and a chemical sensor (Bisantrene). However, the results did not yield reliable ATP measurements in cells. The main issues encountered with these two sensors will be discussed in detail in the following sections.

2.4.2 Capabilities and limitations of genetic ATP sensors

As discussed in the first chapter, a genetically encoded sensor, MALIONR, was initially used to record the morphological changes during intracellular ATP depletion and measure diffusion coefficients in starved 769-p cells (Fig 20A). The sensor was chosen for its high specificity and easy integration with the biological systems post-transfection.

To measure ATP levels quantitatively, FCS was the best single-molecule technique. While others have measured overall fluorescence intensity, my goal was to focus on single-cell measurements. The sensor allowed for the detection of morphological changes during ATP depletion via confocal imaging; the measurement of diffusion coefficients in cell cytoplasm using FCS could not be achieved. This sensor consists of a red fluorescent protein called

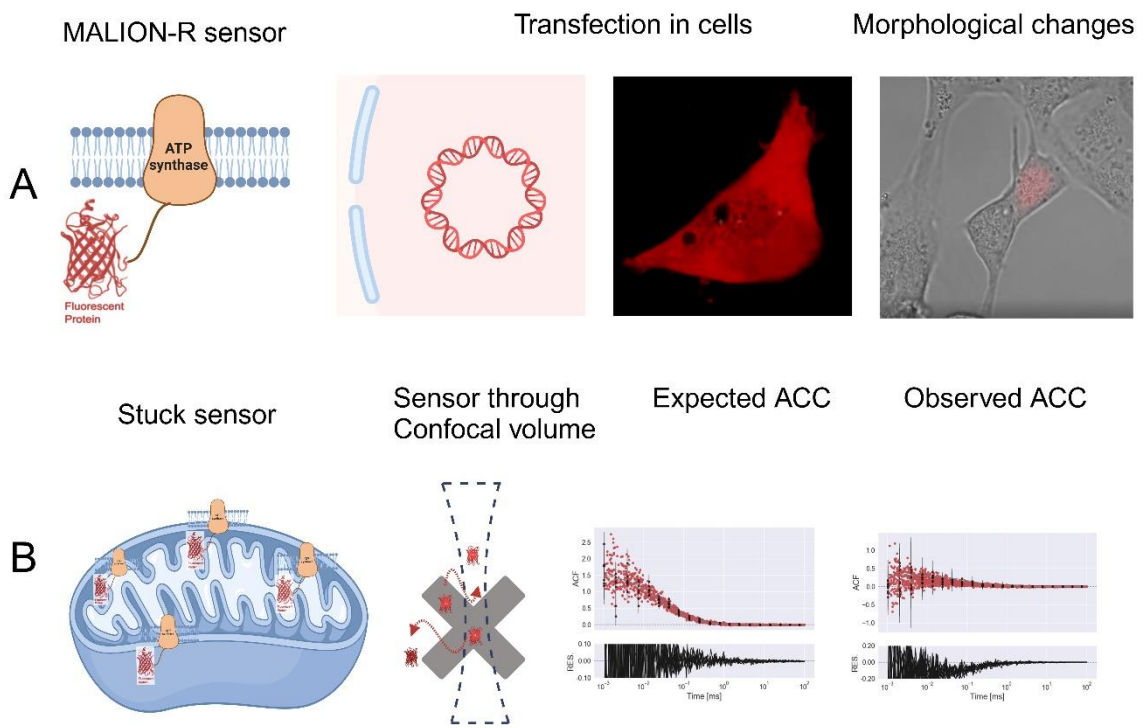

Figure 20: Genetic ATP nanosensor for studying intracellular ATP changes. After transfection into mammalian cells, the sensor was found to be immobilised (stuck) due to its interactions with intracellular membranes. This made studying the movement of the sensor bound to ATP difficult using FCS. Scale bar in the image (A): 60 µm.

mApple, inserted into the ε subunit of F_0-F_1 synthase, a component of the membrane-bound ATPase complex. On transfection, the sensor localises within the cytoplasm, where ε subunit binds to ATP, triggering a conformational change that alters the fluorescence of mApple.

For FCS measurements, the fluorescent probe must be able to diffuse within the confocal volume. However, due to its inherent interaction with membrane components, the sensor or parts of the sensor could interact with intracellular membrane structures, limiting its mobility within the cytoplasm and hindering its ability to diffuse freely for accurate measurements of diffusion coefficients (Fig 20 B). This hindered the acquisition of FCS curves, preventing the quantification of intracellular ATP. Additionally, the number of ATP binding sites on the sensor could not be identified, making it challenging to determine its molecular brightness, further affecting ATP quantification.

Genetic nanosensors expressing fluorescently tagged ATP binding protein motifs have been in circulation from some time[122,123]. While they are widely used in extensive studies, these sensors require tedious protocols of plasmid transfections into cell lines. To negate this shortcoming, a novel chemical sensor was explored as a reasonable alternative for simple ATP quantification assays.

2.4.3 Bisantrene as ATP sensor

Anti-tumour activity of anthracene drugs, including bisantrene and doxorubicin, was established in the late 1980s. Since then, these drugs have been used to target multiple leukaemia and solid tumours like breast cancer[124]. Bisantrene reduced cell growth in the brain, breast, and pancreatic cancers[125]. The bioactivity of this drug on various types of cancer has been studied previously[126]. While the anti-tumour activity of this molecule has been well documented, another study highlighted the possibility of using it as an intracellular ATP sensor[127]. The affinity of bisantrene salt towards ATP was demonstrated, and its application was studied as a fluorometric ATP sensor when excited at 370 nm.

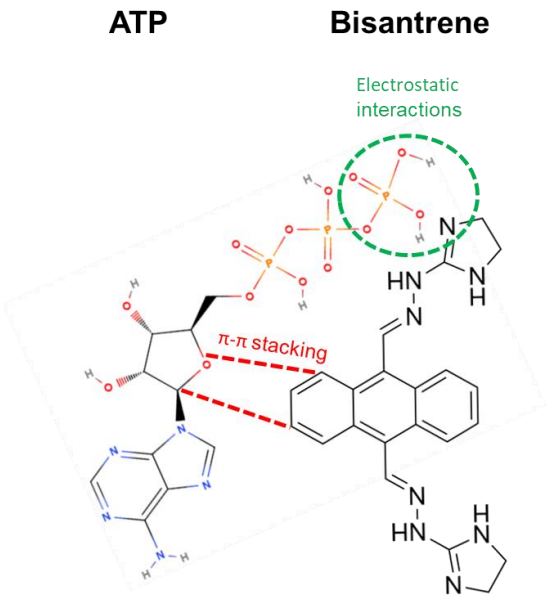

Figure 21: Chemical interaction between bisantrene and ATP to produce fluorescence. The anthracene core of bisantrene is planar and can intercalate between base pairs of nucleic acids present in ATP (red lines). This can lead to π-π electron conjugation. This interaction is presumably stabilised by the interaction between negatively charged phosphate groups of ATP and negatively charged amines in bisantrene (green circle).

According to the following referred study[127], anthracene moiety in contact with an ATP molecule causes the rearrangement of electron clouds in the anthracene core, leading to π-π electron conjugation (Fig 21). This rearrangement causes photon emission, with an emission maxima recorded at 504 nm. It was explained that this interaction is stabilised by the electrostatic attraction between the negatively charged phosphate group of ATP and the positively charged amine group in the anthracene ring.

2.4.4 Bisantrene-ATP interaction studies using TCSPC

Studies suggest that anthracene and its derivatives fluoresce between $\lambda_{ex/\,em}$: 300 / 500 nm[128,129]. The choice of buffer largely influences the fluorescence properties of many molecules. Different concentrations were tested in different buffers to test the changes in fluorescence intensity of the bisantrene-ATP complex. Refer to Appendix B.6, Table B4 for information regarding molecular characteristics, types of buffer, bisantrene and ATP concentrations.

Fluorescence intensity or counts/s were recorded using the time trace information from TCSPC measurements. Although no significant molecular brightness was recorded to obtain ACC at

these concentrations (appendix B.6, Table B4) of the bisantrene-ATP complex, increasing the concentrations of bisantrene alone in buffers showed higher photon counts (Fig 22). Equal volumes of ATP and bisantrene were added to the buffers to assess the molecular brightness of the ATP-bisantrene complex (Refer to Appendix B.6, Table B4). When micromolar bisantrene concentrations were analysed in buffers, increased peaks in time trace were observed (Fig 22).

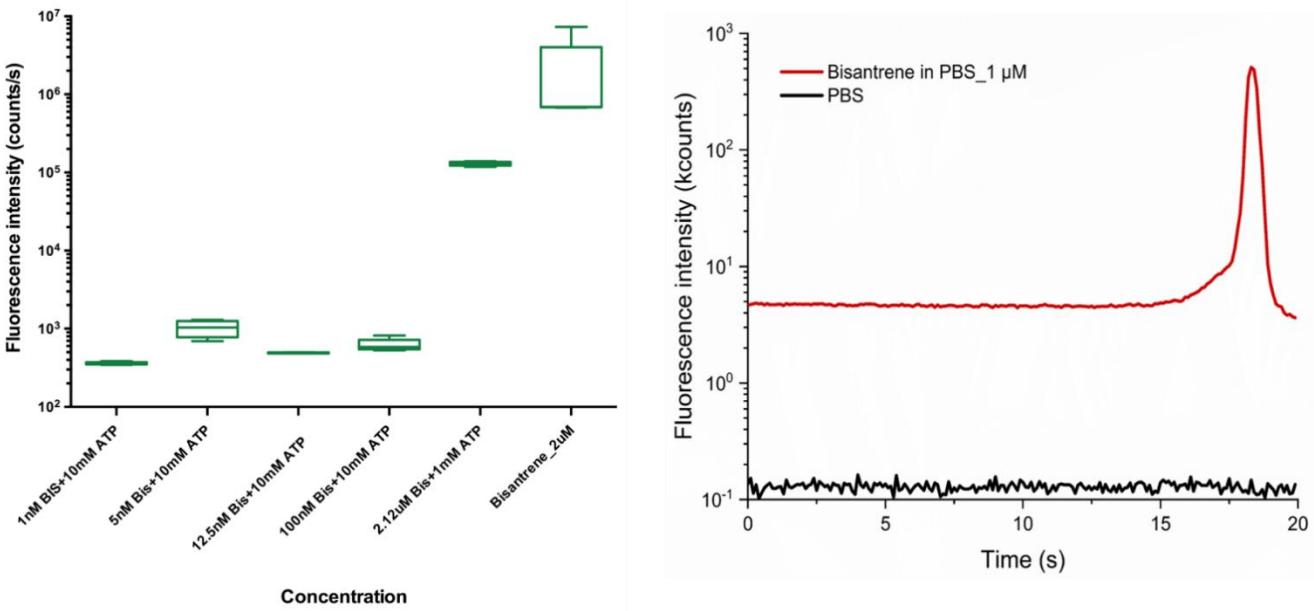

Figure 22: Fluorescence of bisantrene. The graph on the left show fluorescence intensity counts of bisantrene with and without ATP, in PBS. Each bar represents measurements taken in buffer at different concentrations. 5-10 measurements per sample were taken for 30 seconds. 2 μM bisantrene in PBS under a confocal microscope fluoresces on excitation with a 488 nm laser, emitting at λ = 520 nm. Time trace data for bisantrene in buffer revealed an increased fluorescence intensity cell count in μM concentrations, shown on the right.

The fluorescence intensity of the bisantrene molecules in the buffer solution increases significantly with bisantrene concentration (Fig 22, left panel). The fluorescence intensity measured at low nanomolar concentrations (1-100 nM) was between 100 and 1000 counts/s. When the concentration of bisantrene was increased to 2 μM, the fluorescence intensity increased by several orders of magnitude ($10^6 – 10^7$ counts/s). This increase was observed in the presence of ATP (ATP-bisantrene complex) and without (2 μM bisantrene only in buffer). The sharp peak in the time trace of fluorescence intensity (Fig 22, right panel) was associated with the presence of bisantrene molecules in buffer, and no significant contribution from ATP was observed. This suggests that bisantrene exhibits a concentration-dependent increase in fluorescence intensity, with the highest intensities observed at higher concentrations, independent of ATP's presence.

2.4.5 Polarisation Results

Polarisation microscopy was applied to explore further the nature of bisantrene molecules in different water-based buffers. These experiments were performed with the help of Dr. Agnieszka Wisniewska. Bisantrene crystals were observed in physiological buffers like PBS and water. Furthermore, bisantrene crystal morphology was evaluated at three temperatures in water and PBS buffers. At 25˚C, needle-shaped and tetrahedron-like crystals were detected in both the water and PBS, respectively. To assess the temperature dependency of crystal formation, images were recorded at increasing temperatures from 25˚C to 80˚C. On increasing

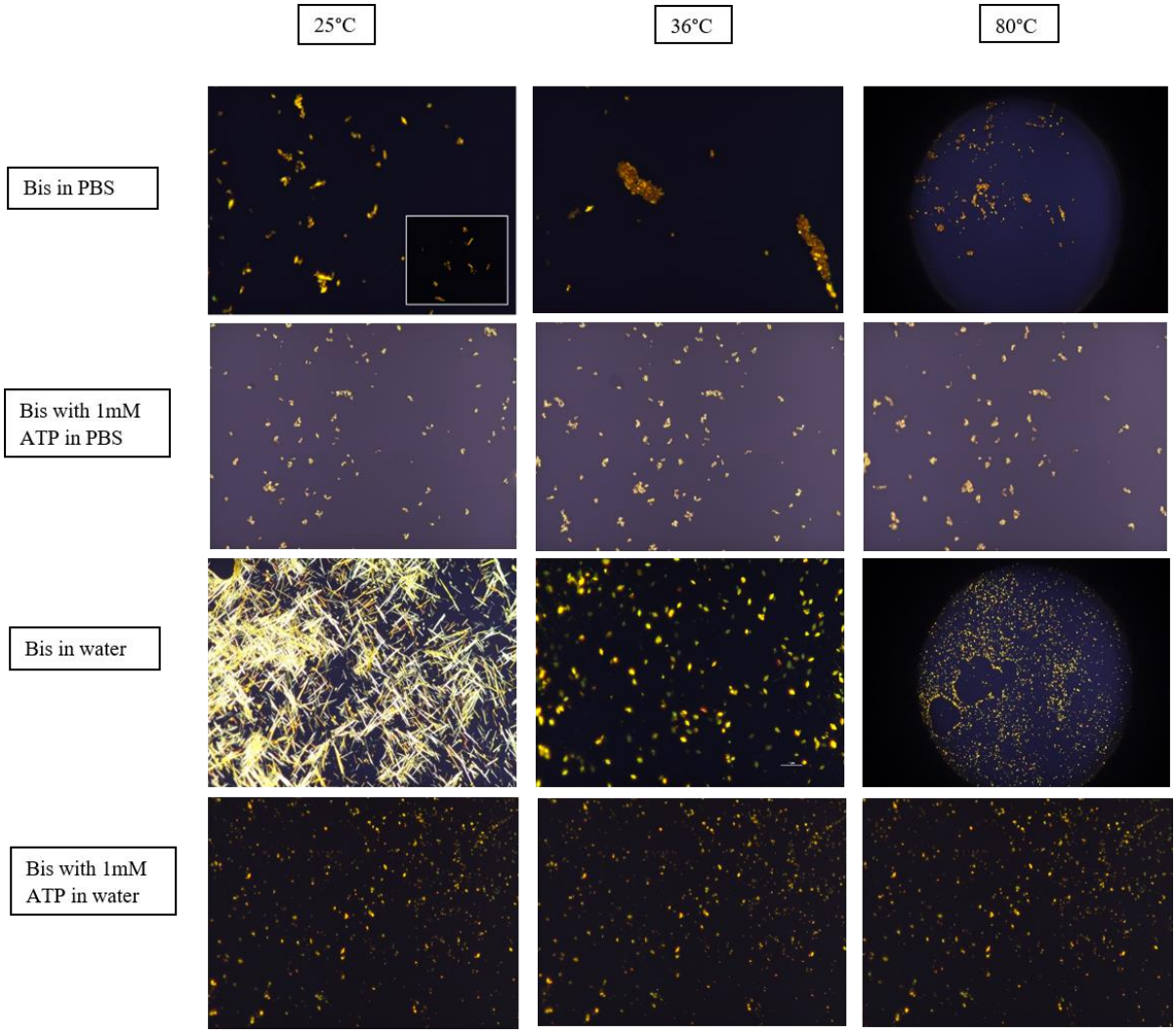

Figure 23: 2 µM bisantrene crystal solution in water and PBS under polarisation microscope. The image of bisantrene in TRIS:DMSO buffer is presented as an inset in the first image. Sharp needle-like crystals, and diamond-shaped small crystals of bisantrene were observed in water (middle panel: left to right). No change in aggregation or crystallization was recorded with an increase in temperature when ATP was added to bisantrene in water (bottom panel: left to right) and PBS (middle panel: left to right). Polarisation images after cooling temperatures from 80˚C to 25˚C (data not presented) were recorded. All images were taken after reaching respective temperatures at T0 min.

the temperature in water, needle-shaped crystals disappeared. This could be due to the increased solubility of bisantrene crystals in water at a higher temperature.

Needle-shaped crystals completely dissolved at 36˚C (temperature required for cell growth supplemented with 5% CO_2), leaving only tetrahedron-shaped crystals by the end of the first temperature cycle (80˚C in water). Needle-shaped crystals reappeared when the temperature was gradually lowered from 80˚C to 36˚C at intervals of 3˚C every 5 mins (Fig 23). From observation, it was noted that recrystallisation reduced crystal size. Similar experiments were performed with bisantrene crystals in PBS. Bisantrene crystals remained tetrahedron in shape, without any change with changing temperature cycles. Samples with bisantrene containing different concentrations of ATP were checked in water and PBS. No changes were reported in crystal shape, size or solubility. Results for 2 µM bisantrene with 1 mM ATP in water and PBS are shown in Fig 23.

In conclusion, bisantrene crystals exhibit temperature-dependent morphological changes in water. Needle-shaped crystals dissolved at 36˚C and recrystallized upon cooling, resulting in reduced size. In contrast, tetrahedron-shaped crystals in PBS remained stable and unchanged across temperature cycles and in the presence of ATP.

2.4.6 Spectroscopy results

As the concept of using bisantrene as an ATP sensor was derived from a previous study, I replicated the findings from that study to acquire spectroscopic data on the absorption of

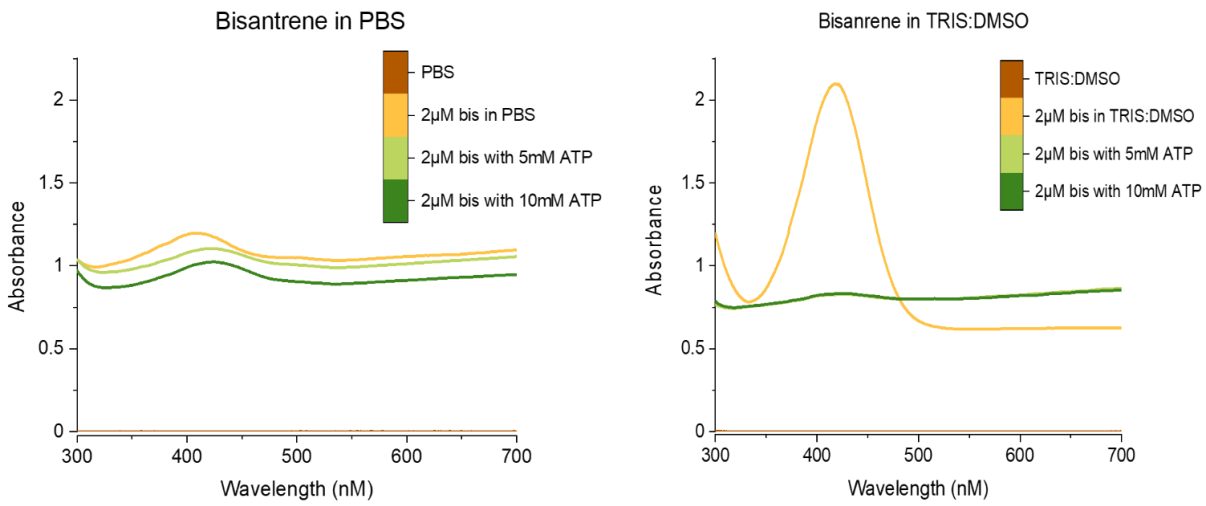

Figure 24: UV-Vis absorbance spectra of bisantrene in PBS and TRIS:DMSO buffer : (a) and (b) Absorbance of different concentrations of bisantrene salt (with and without ATP) at 25˚C in PBS and TRIS:DMSO (90:10) respectively.

bisantrene (300 – 700 nm) in 2 different buffers at 25˚C. For TRIS:DMSO buffer, a spectrum corresponding to the one observed in the parent study was obtained (Fig 24). The same measurements were performed in a water-based PBS buffer. When the DMSO-based stock solution of bisantrene was dissolved in PBS, increased opacity of the solution following subsequent precipitation and sedimentation of the crystals was observed. The solution contained suspended particles, impairing absorbance measurements. The presence of bisantrene crystals in PBS was responsible for light scattering. Thus, the absorbance measurements for bisantrene in PBS were a collective sum of the sample's absorption and scattering. This is evident from the decreased apparent absorbance reported in the solution when the salt started settling down in PBS (Fig 24).

2.4.7 Intracellular behaviour of Bisantrene

This research aimed to understand the interaction of bisantrene as a chemical sensor for ATP in a physiologically relevant media (as opposed to a precious study[127] where bisantrene's fluorescence properties were checked only in organic media) and a live cell model. Thus, bisantrene behaviour towards mammalian cells was analysed. In a typical HEK/HeLa cell, ~3×10^{10} ATP molecules (5-10 mM) can be found in the cytoplasm[130]. To study the potential of bisantrene as an intracellular ATP sensor, 1 and 2 µM bisantrene dihydrochloride prepared in PBS were added to human embryonic kidney (HEK 293) cells to investigate drug-ATP interaction in an intracellular environment. I examined the fluorescence of bisantrene-treated cells using a confocal microscope. Both 405 nm and 488 nm lasers were used. However, only the 488 nm excitation yielded a fluorescence signal from a small population of cells (Fig 25 C, F). The number of fluorescent cells was significantly lower compared to the non-fluorescent cell population.

The uptake of bisantrene by HEK cells was non-uniform since a very small percentage of HEK cells were fluorescent. Cellular uptake of bisantrene was very low in HeLa cells as well. Bisantrene concentrations as low as 1-2 µM proved toxic to cells within 20-30 minutes after its addition. Cells began detaching from the glass slide during this time. Cells still attached to the surface had bisantrene crystals/aggregates attached to the cell membrane. On close observation, apoptotic bodies could be seen in HEK cells after 20 min of bisantrene addition (Fig 25 E). A green fluorescent signal from the extracellular environment was observed. It was unclear whether the signal was due to bisantrene-induced cell lysis or from the free molecules

of bisantrene interacting with each other in PBS. In the case of cell lysis, the released ATP from cells could have interacted with the free bisantrene molecules to exhibit a fluorescence signal. To negate the effect of cell lysis, only bisantrene salt (2 µM) in PBS (without cells) was excited with a 488 nm laser (Fig 25 C), and the fluorescence was observed under a confocal microscope.

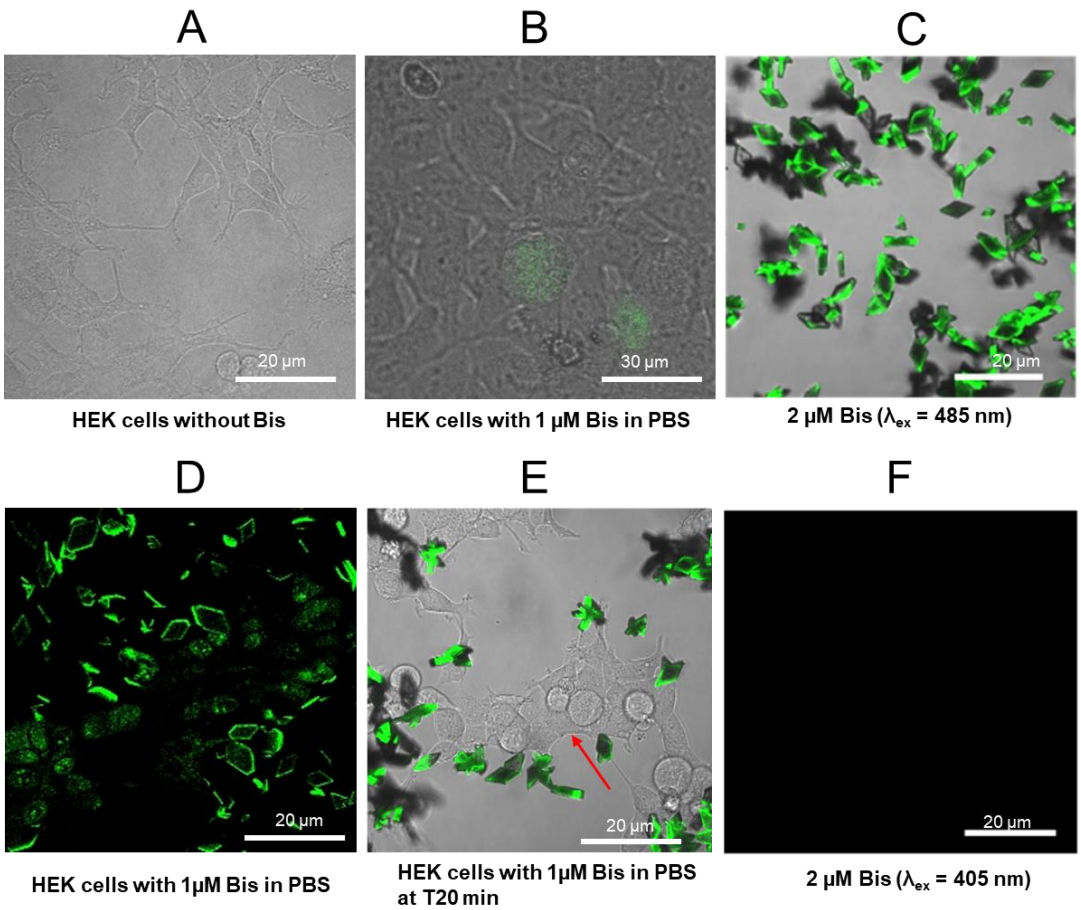

Figure 25: Confocal images of bisantrene salt interaction in HEK cells. (A) Cross-section of HEK cells seeded in 35mm glass-bottom slide and viewed in brightfield before adding bisantrene. (B) Fluorescence of 1 µM bisantrene salt in PBS on HEK cells imaged upon excitation at 485nm (T=0 min incubation with bisantrene, all channels). (C) 2 µM bisantrene crystals in PBS (λ_{ex} = 485 nm). (D) Fluorescence of 1 µM bisantrene salt in PBS on HEK cells imaged upon excitation at 485nm (T=0 min incubation with bisantrene, EGFP channel). (E) Uptake of 1 µM bisantrene salt in PBS by HEK cells, with apoptotic morphology (red arrows) formed after 20 min of drug addition. (F) 2 µM bisantrene crystals in PBS (λ_{ex} = 405 nm).

The fluorescent signal was recorded from compact shapes attached outside the cells, which could be crystals or aggregates of bisantrene salt (Fig 25 E). Further experiments conducted in HeLa GFP cells aimed to examine the crystal morphology of bisantrene. The area and length of bisantrene crystals and HeLa in PBS were measured. Fig 26 shows the difference in the length and area of bisantrene crystals (~12 µm) and HeLa cells (~140 µm) as measured,

respectively. The bisantrene crystal to cell size ratio is 10x different from each other. However, for passive cellular uptake, smaller molecules are much more favourable130, which explains my previous observation of minimal uptake of bisantrene by cells.

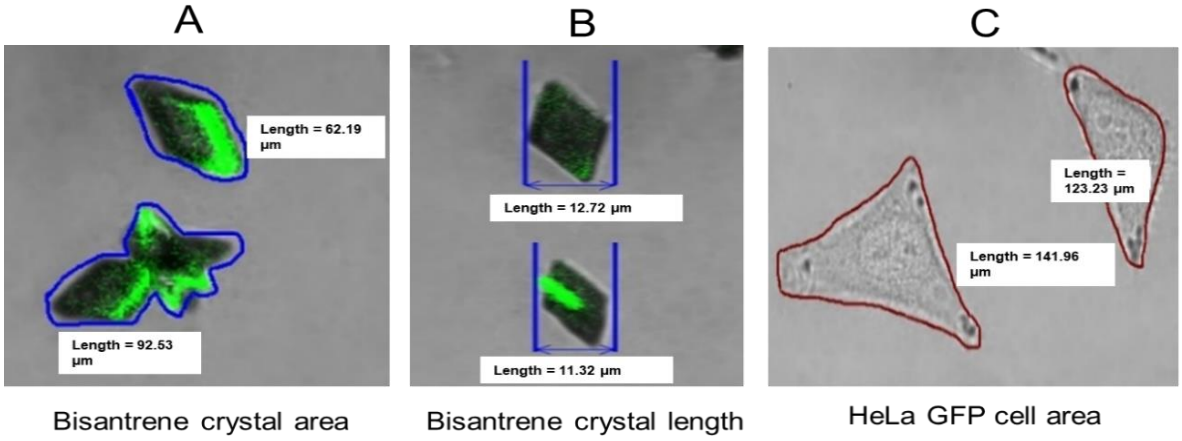

Figure 26: Size determination of bisantrene crystals and HeLa cells. The size of cells and crystals are in the same order of magnitude (~µm), which explains the little uptake of crystals by the cells.

2.4.8 Conclusion

These studies conclude that bisantrene forms crystals in physiologically relevant media, generally used for growing cells. The size of these crystals is comparable to the size of the cells, making it impossible for them to be up-taken by mammalian cells. ATP binding with this crystallised salt might form stable interactions, hindering bisantrene from changing its chemical structure to fluoresce. It is crucial to highlight that drug size, temperature and buffer conditions are important factors to be considered when studying bis-ATP molecule interactions. Thus, the application of bisantrene as an ATP sensor in living cell models is unlikely.

2.5 Cellular autofluorescence

2.5.1 Increased autofluorescence as a response to Staurosporine-induced cell stress

Living cells are composed of various biomolecules, many exhibiting fluorescent properties when excited by UV-Vis light. Increased autofluorescence, observed within the ultraviolet (300 – 400 nm) to visible light (400 – 700 nm) wavelength range, has been characteristic of abnormal behaviour in many organisms. It reflects changes in the concentration or state of

endogenous fluorophores like NADH, FAD, lipofuscin, collagen, elastin and many more[131]. Multiple studies have identified increased autofluorescence as a stress response during or preceding cell death[132–134]. Staurosporine (STS) is an alkaloid responsible for inducing intrinsic apoptotic cell death by altering mitochondrial membrane potential[135]. The study aimed to explore the effects of STS on cellular autofluorescence and extracellular aggregate formation across various cancer cell lines. Initial observations suggested increased fluorescence intensity upon STS treatment, prompting further investigation into its underlying mechanisms and contributing molecular species. In this chapter, confocal microscopy, fluorescence lifetime imaging, and HPLC will be used to analyse the increase in autofluorescence in cancer cells following STS treatment.

2.5.2 Confocal imaging of different cancer cell lines during STS treatment

STS powder was dissolved in DMSO to make a 4.2 mM stock solution, which was then diluted with PBS to a final concentration of 100 µM. The final solution of STS was added to four cell

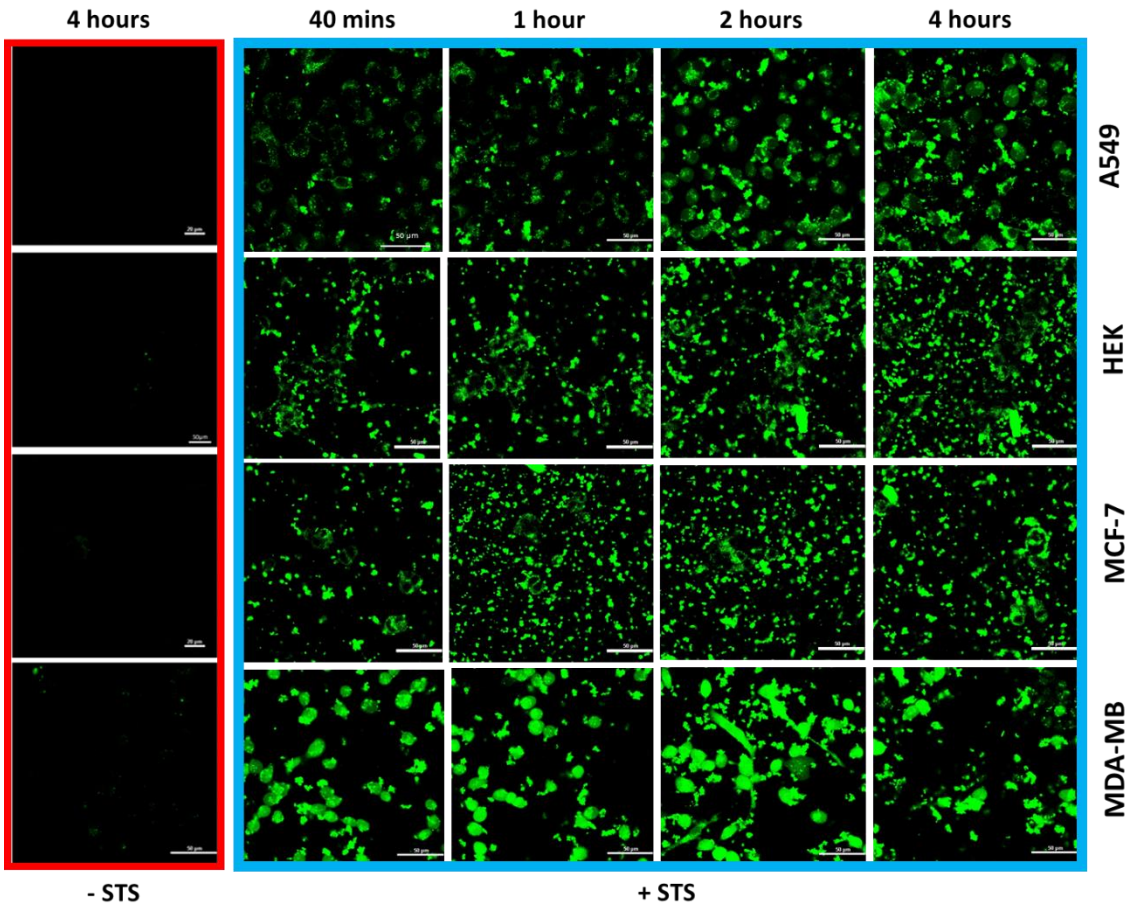

Figure 27: Confocal images of different cell lines under the influence of STS at 100 µM. Before drug addition (-STS), cells kept in PBS showed no fluorescence at λ_{ex} = 488 nm (red box). After drug addition (+STS), starting from 30 min till 2h, an increase in fluorescence intensity was observed in these cell lines (blue box). Scale: 20 µm.

lines - MCF-7, A549, HEK and MDA-MB. A high concentration of STS (100 µM) was used to ensure near-maximal inhibition of protein kinases and accelerated apoptotic response[136], approximately 100-1000 times higher than the typical IC_{50} range (0.1-10 µM) used in longer experiments for most cancer cell lines[137]. Staurosporine treatment caused an increase in the number of extracellular aggregates, which exhibited fluorescence upon excitation with a 488 nm laser. An increase in fluorescence intensity due to aggregates was observed in all cell lines after half an hour of treatment with STS. The fluorescent aggregates outside the cells were consistent and independent of the cell type, indicating a shared underlying mechanism (Fig 27).

Cells showed membrane blebbing after 1-2 h of treatment. The apoptotic morphology of cells was confirmed with confocal microscopy (Fig 28, inset zoom image). Mean fluorescence intensity (MFI) inside and outside the cells was quantified from these confocal images using Imaris software. MFI is described by the voxels (3d pixels) enclosed within the cytoplasm and aggregates to calculate the voxel intensity statistics. The sum of MFI from each pixel has been described in Fig 28 below. MFI inside the cell cytoplasm has been highlighted with white boundaries, and aggregate MFI was calculated for the blue dots. Analysis of the images revealed that the mean fluorescence intensity outside the cells (aggregates) was approximately tenfold higher than that inside the cells (Fig 28). The fluorescence signal recorded from the PBS buffer outside the cell was stronger than inside cells, likely from aggregates or other autofluorescent species bound to cell debris, contributing to the increased fluorescence. In contrast, the fluorescence intensity signal from the cell cytoplasm was weaker, arising from natural cellular autofluorescence. The number of aggregates observed outside the cells increased when the cells were exposed to the drug for 4 hours as compared to the first hour of treatment (Fig 28). However, this increase in the number of aggregates did not significantly alter the fluorescence intensity inside or outside the cells.

This may be due to several factors. First, since confocal imaging was used, variations in the imaging depth could have influenced the captured fluorescence signal, potentially leading to an underestimation of changes in fluorescence intensity. Additionally, the characteristic fluorescence intensity of the aggregates or complexes themselves might not vary with the increase in their number, resulting in no significant change in overall intensity. Thus, no saturation or equilibrium was likely reached while aggregates increased, and the fluorescence signal remained stable.

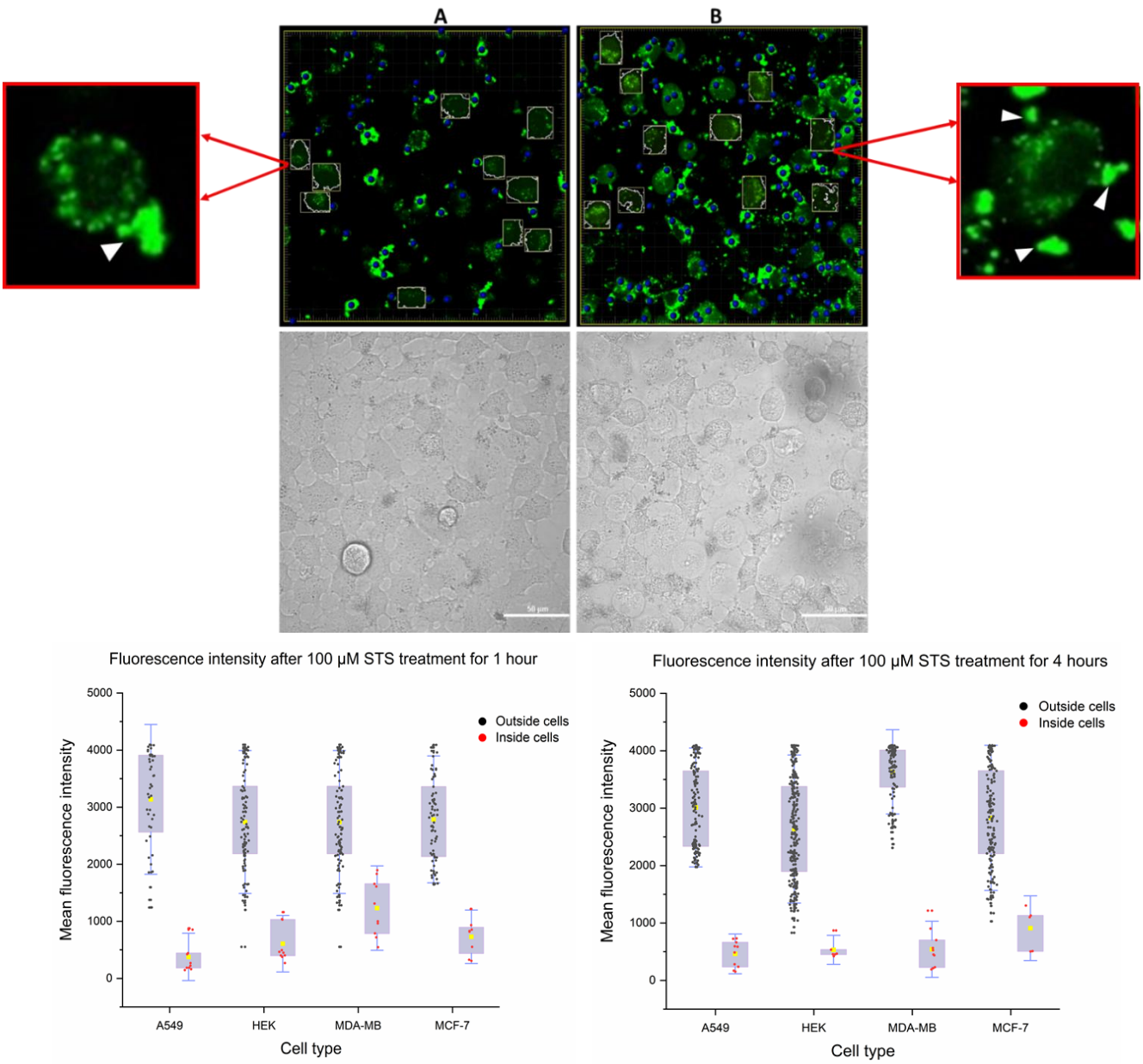

Figure 28: Mean fluorescence intensity in cells after staurosporine treatment. (A) and (B) represents the confocal image analysis for A549 cells in Imaris as an example. A similar analysis was done for all cell lines. Scale: 20 µm. The blue dots represent the aggregates, and the white boundary outline represents apoptotic cells. Mean fluorescence intensity (MFI) for aggregates and cells has been compared between different cell lines below the images as box plots. Each dot on the box plot corresponds to aggregate intensity (black dots) and cell intensity (red dots). The yellow dot for both plots is the mean intensity. MFI is plotted on the y-axis, with cell lines on the x-axis, for both aggregates and cells, at 2 different time points.

2.5.3 Cell viability after STS treatment

MTT assay was performed on all cell lines after 4 hours of treatment with 100 µM STS. The experiment was performed to quantify the heterogeneity in the cytotoxic effect of STS on different cell lines. % cell viability was calculated as follows:

$$\% \text{ viability } = [\frac{\text{Treated sample} - \text{blank (PBS)}}{\text{Untreated sample} - \text{blank (PBS)}}] * 100$$

At 100 µM after 4 hours, cell viability varied between different cell lines. MCF-7 cells were most affected by the cytotoxic effects of STS, whereas A549 cells had the highest cell survival (Fig 29). The percentage viability quantified by MTT depends on multiple factors, including treatment duration, concentration, and cell susceptibility to death due to a particular drug.

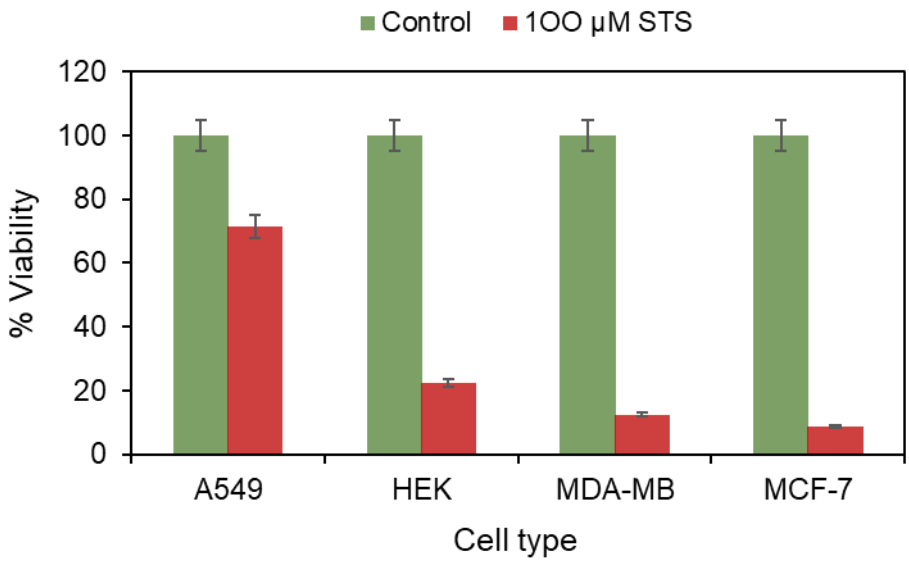

Figure 29: MTT cell viability assay on cells after STS treatment. The absorbance was calculated in triplicates for all cell lines – treated, untreated and blank samples. The assay was performed in a 96-well plate on the same day for all cell lines, at a seeding density of 50,000 cells/well. The error bars represent the standard error of mean.

2.5.4 Fluorescence of Staurosporine

To determine if STS itself contributed to the fluorescence, its optical properties were analysed. λ_{max} of STS was calculated using the Woodward-Feiser[138] rules**,** a set of empirical guidelines used to predict the absorption maxima of organic compounds based on their structure. These rules were derived from experimental data and are used as a practical method to estimate the λ_{max} for compounds with similar structural features. This differs from a purely experimental approach, where λ_{max} would be measured directly using a UV-Vis spectrophotometer. By applying the Woodward-Fieser rules, I estimated the λ_{max} of STS.

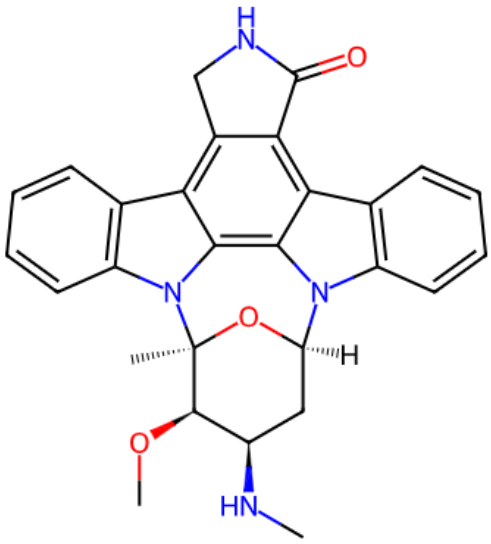

Figure 30: Structure of staurosporine.

STS is a tetracyclic alkaloid with a fused benzene, pyridine ring system, and other functional groups[139]. It has connected rings of quinolone and indole with alternating single and double bonds. This allows free electron movement across the entire structure, creating a conjugated system. Conjugated systems have light absorption tendencies, usually in UV-visible regions. As the extent of conjugation in the system increases, the absorption wavelength and fluorescence emission shift to longer wavelengths. Based on this conjugated structure, λ_{max} of the system can be estimated using rules as follows:

$$\lambda_{max} = \text{Base value} + \text{Substituent contributions} + \text{Other contributions}$$

With the base value of aromatic conjugated systems adjusted for quinolone and indole conjugation, STS's estimated λ_{max} (absorption) is 320-360 nm. Further applying stokes shift to the absorption maxima (80 – 100 nm) estimates the fluorescence emission of STS at 400-460 nm. Based on the Woodward-Fieser rules[140,141], table 6 below has been constructed to illustrate

the contributions of individual substituents in the STS conjugated system, as predicted by these rules. These calculations demonstrate that STS is not expected to be fluorescent on its own when excited with a 488 nm laser.

Table 6: Calculation of λ_{max} for STS using Woodward-Fieser rules of electronic conjugation in aromatic systems.

Steps	λ_max	Systems
Base λ_{max} for conjugated aromatic systems	250-270 nm	Base value for aromatic conjugated systems.
Quinoline conjugation	+30-40 nm	Quinoline is a fused benzene-pyridine system.
Resulting λ_{max} for quinoline	280-310 nm	λ_{max} shift due to quinoline conjugation.
Indole conjugation	+30-50 nm	Indole conjugation with quinoline.
Final λ_{max} (absorption)	320-360 nm	λ_{max} after considering both quinoline and indole.
Fluorescence λ_{max} (after Stokes shift)	400-460 nm	Estimated by applying Stokes shift (80-100 nm).

Furthermore, STS was tested for its intrinsic fluorescence in PBS at 36°C using TCSPC. No fluorescence was obtained for staurosporine at PBS's highest tested concentration (100 µM). This suggests that either the molecule's counts per second (fluorescence intensity) are too low or the molecule could not be detected by the SPAD detectors in the TCSPC. To eliminate vendor bias, staurosporine from three vendors was tested (Selleckchem, Sigma Aldrich and Merck). Since no fluorescence response was observed for cells treated with 100 µM, the lower concentrations of STS were neglected for this analysis.

To investigate the fluorescence properties of STS within a cellular context, it was imaged in PBS buffer supplemented with model proteins such as albumin, BSA, and lysozyme. These experiments offer initial insights into how STS might interact with molecular components in the cytoplasm. This experiment aimed to assess changes in intrinsic fluorescence characteristics of staurosporine in the presence of naturally occurring biomolecules, like proteins. Fig 31 represents images taken on a confocal microscope. The fluorescence intensity of 100 µM STS in PBS buffer, when excited with a 488 nm laser, was almost negligible. STS showed some autofluorescence in PBS in the presence of naturally present biomolecules (Fig 31).

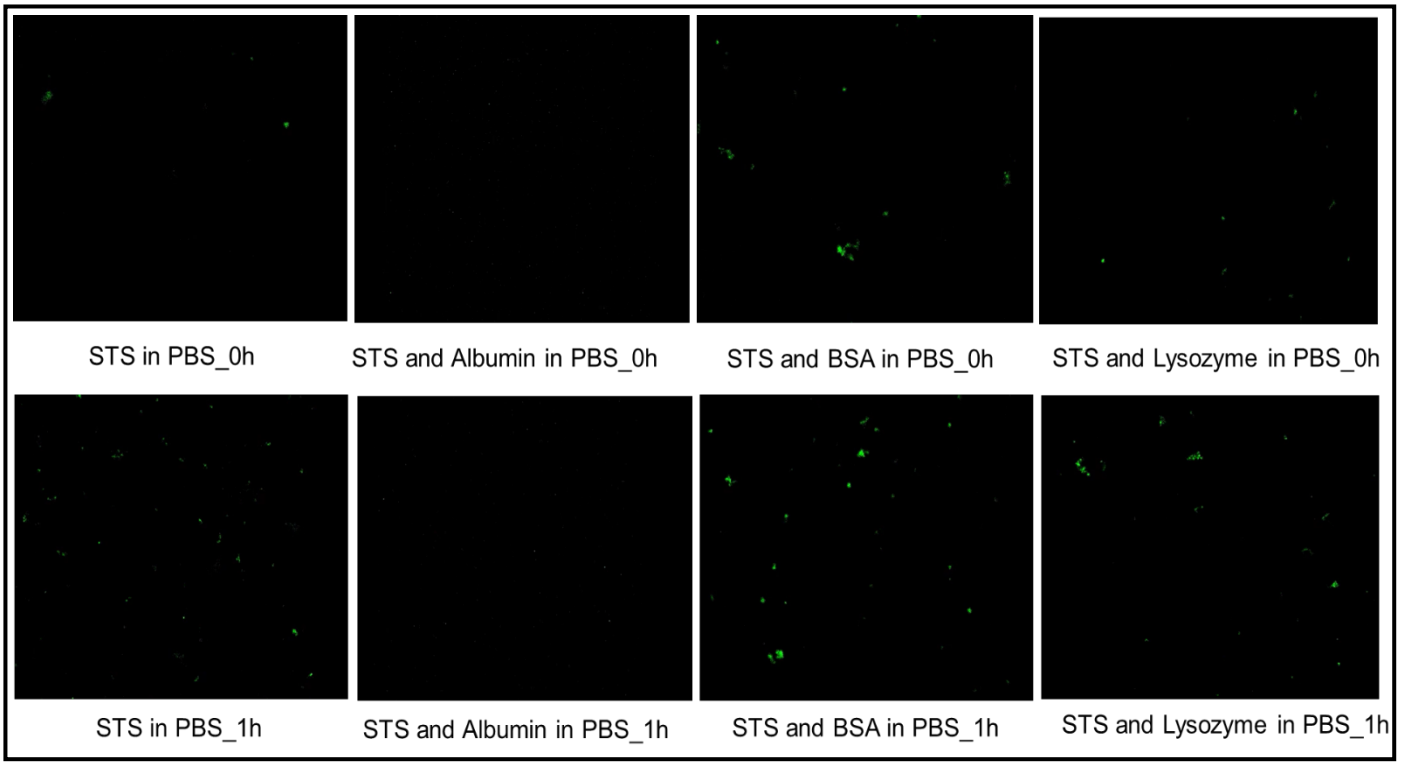

Figure 31: Staurosporine in the presence of other biological molecules. 100 µM STS in PBS, in the presence of naturally present biomolecules like BSA, albumin, and lysozyme (at physiological concentration), shows some fluorescence at λ_{ex} = 488 nm. However, STS alone in PBS does not fluoresce. Scale bar: 20 µm.

2.5.5 Autofluorescence in heat inactivated cells

Experiments involving heat-inactivation of cells were conducted to assess whether active cellular metabolism or protein interactions with STS influenced the observed increase in fluorescence - in and outside cells. Cytoplasmic protein denaturation in mammalian cells begins at temperatures above 42 degrees, with significant denaturation detected around 70 degrees for most proteins[142]. Complete or extensive denaturation leads to loss of function with destruction of protein structures[143], thus impairing metabolic processes. In my experiments, cells were heated in a water bath for 1 hour at 90 degrees. After that, cells were observed under a confocal microscope. Increased cellular autofluorescence was detected in heat-inactivated cells, without STS (Fig 32 C), compared to control/untreated cells (Fig 32 B – without STS, with no heat inactivation). Additionally, heat-inactivated cells retained the fluorescence following STS treatment and new extracellular fluorescent species were detected after the STS was added to the buffer (Fig 32 F, G). STS did not significantly alter internal cellular fluorescence. However, additional extracellular fluorescent species were observed in the buffer after STS addition. This further confirmed the hypothesis that intrinsic cellular fluorophores,

rather than drug-protein interactions, were responsible for the observed autofluorescence. On the other hand, STS may be binding to cell debris in heat-inactivated cells, forming fluorescent extracellular species.

A study demonstrated that dead or metabolically impaired/inactive cells lose their ability to maintain normal redox states[144]. Thus, autofluorescent molecules like NADH and $FADH_2$, along with others, accumulate in cells in their oxidised forms. This accumulation could be causing increased fluorescence after binding with STS, as seen in Fig 32 G, especially in the emission range corresponding to flavins (520 - 540 nm). The live dead analysis of heated cells revealed the accumulation of calcein am and propidium iodide dyes in cells, suggesting a metabolically stressed/inactive state of dying cells after the temperature treatment (Fig 32 D, E).

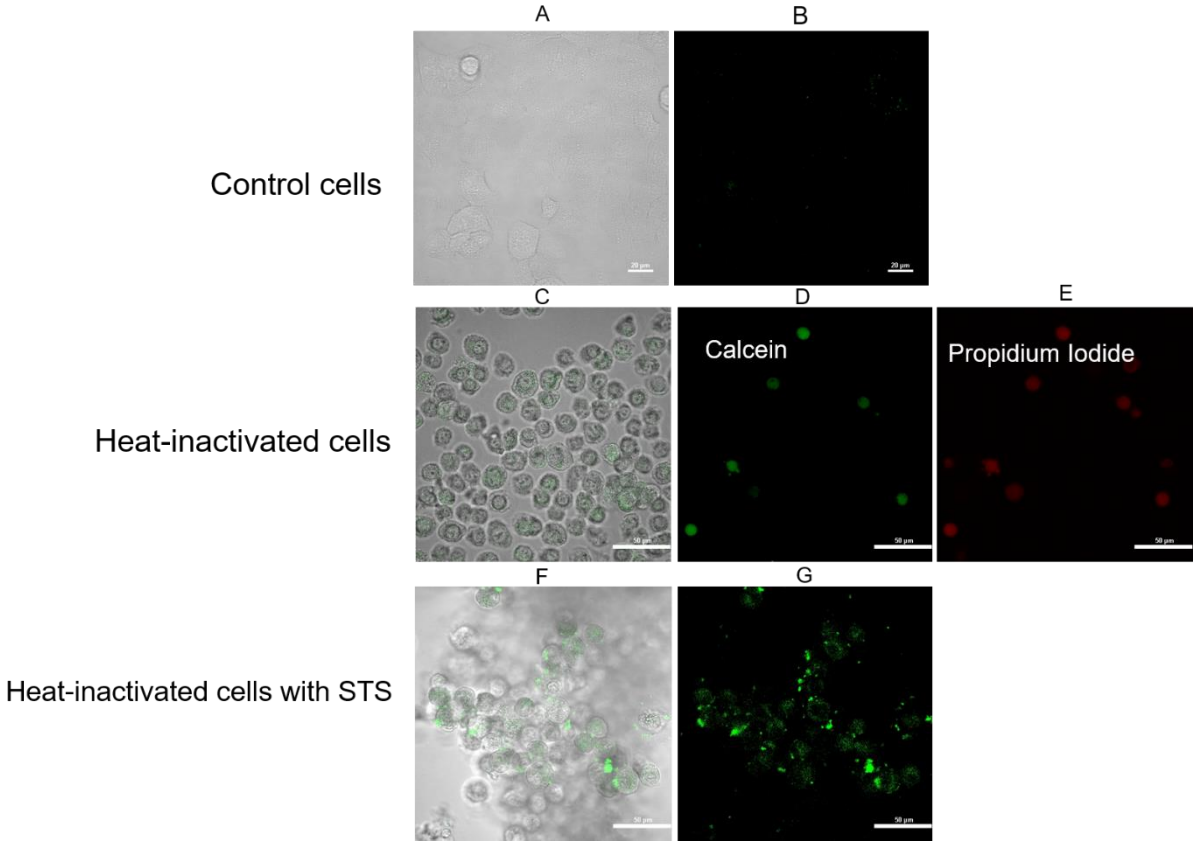

Figure 32: Heat inactivation of cells. Confocal images of A549 cells heated at 90°C for 1 hour show autofluorescence when excited with a 488 nm laser (top panel). Live/dead staining was performed on these cells with 1 µg/ml calcein and 100 µg/ml PI in a 1:10 ratio. Furthermore, 100 µM STS was added to heat-inactivated cells and excited with a 488 nm laser. Confocal images (bottom panel) show fluorescence and TD channel. Scale bar: 20 µm.

This observation led to the hypothesis that STS may influence intracellular fluorophores, potentially through structural modifications, aggregation, or metabolic shifts. The fluorescence observed inside the cells can be attributed to intrinsic biomolecules, as cells continuously generate autofluorescent compounds. Thus, an increased number of autofluorescent molecules post-STS treatment could be causing an enhanced fluorescence signal. The cell samples were also excited with a 405 nm laser. No fluorescence was recorded at this wavelength for any cell line.

2.5.6 HPLC analysis

High-performance liquid chromatography (HPLC) was employed to identify autofluorescent species and extracellular aggregates generated after STS treatment. These experiments were performed with the help of Dr. Monika Asztemborska. HPLC was employed to separate and identify the molecular constituents of autofluorescent species and extracellular aggregates formed after STS treatment. Refer to Appendix B.7 for the HPLC experimental set-up. Cells were treated with 100 µM STS (dissolved in PBS) and kept at 37°C for 2 hours. After 2 hours, PBS was collected from the treated cells and taken for HPLC measurements (Appendix B.7, table B5). The analysis of extracellular aggregates collected from PBS post-STS treatment focused on identifying potential autofluorescent metabolites, particularly FAD and NADH. Both FAD and NADH exhibit intrinsic fluorescence when excited by light in the 300-400 and 450-490 nm range, respectively[145]. Specifically, FAD has an excitation maximum of around 450 nm and an emission maximum of around 520 nm. In comparison, NADH has an excitation peak of around 340 nm and an emission peak of around 460 nm. Given that the excitation wavelength of the 488 nm laser falls within the range where both metabolites exhibit significant fluorescence (confocal microscopy results, Fig 27), it is reasonable to attribute the observed autofluorescence to FAD or NADH in the PBS samples collected after STS treatment. Therefore, these two metabolites were primarily chosen for HPLC analysis in the samples. Refer to the table below for the experimental design.

While NADH was not detected, a peak corresponding to FAD was observed, consistent with its known absorption properties and the detection wavelength. Since FAD is a natural cellular component, it was hypothesised that the drug might induce conformational changes or aggregation, altering FAD's fluorescence. For FAD detection, samples were measured for 20 min each at excitation/emission wavelengths of 450 nm/500 nm. Since the peak of interest eluted consistently at 12 mins and matched the retention time of the reference FAD under the

same experimental conditions, the experiment was carried out for a total length of 20 min for each sample.

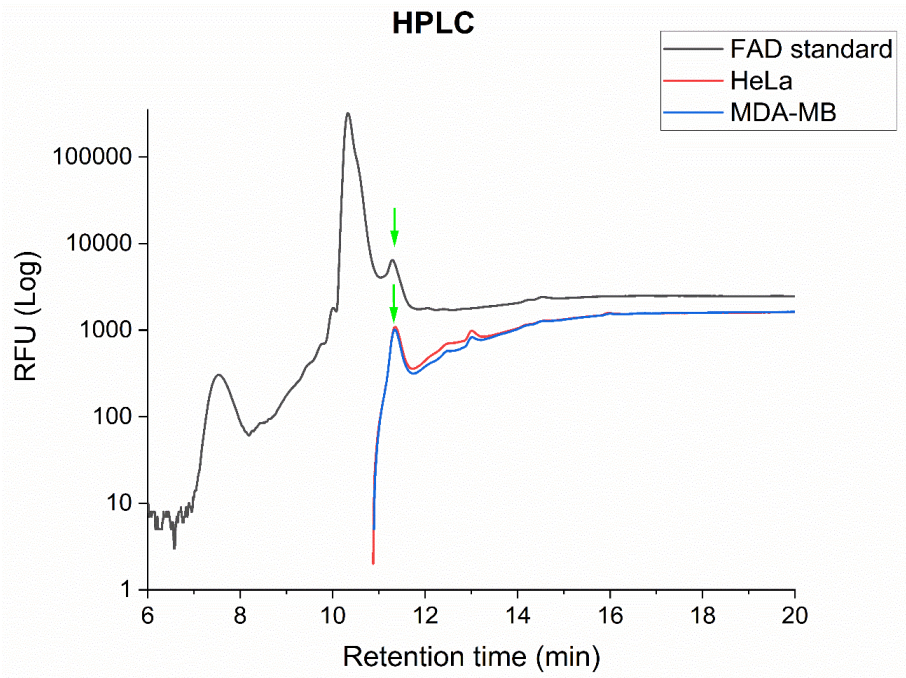

Figure 33: Chromatogram from HPLC measurements for two cell lines to confirm the presence of FAD in PBS exudes, treated with 100 µM staurosporine for 2h. The black curve shows the standard FAD for comparison with other cells. The green arrow for the peak at 11 min shows a similar peak for FAD in all the samples, in comparison with the standard FAD in solution.

The results were plotted as fluorescence intensity vs retention time for two cell lines (Fig 33). After 20 mins excitation, chromatograms revealed a high fluorescence intensity peak from FAD standard in the buffer (10^5 RFU) between 10-11 min retention time and a lower intensity peak (10^3 RFU) between 11-12 min (Fig 33). Similar peaks corresponding to the low-intensity peak of FAD were observed at 11.5 min for samples from both cell lines - HeLa and MDA-MB (10^3 RFU). Due to the presence of cellular debris and other components in the PBS samples collected from the cells, there was poor resolution between the samples before 6 minutes, which hindered the chromatographic separation and affected the ability to detect distinct peaks (before 6 mins). This interference likely contributed further to the absence of the expected larger peak at ~10 minutes. Additionally, since a quantitative analysis of PBS from all cells was not possible due to these concerns, not all cell lines could be tested. Although this supported the possibility that FAD contributed to the fluorescence, the presence of FAD in untreated control cells suggested that the increase in fluorescence could result from altered FAD dynamics rather

than the generation of new fluorophores. Alternatively, the fluorescence might stem from other unidentified species with overlapping spectral properties.

2.5.7 Fluorescence lifetime analysis

The fluorescence of FAD and its lifetime in PBS buffer was measured using FLIM. FCS measurements were also performed for FAD in the buffer. The concentration of FAD used for the fluorescence correlation spectroscopy (FCS) measurements was 1.02×10^{-5} M (as the FCS curve was obtained at this concentration). The size of FAD, as reported in the literature, is estimated to be 0.8 nm[146]. The diffusion coefficient of FAD was calculated from FCS experiments, where three measurements were taken over 30-second intervals at 37°C (physiological temperature for cell growth). The diffusion coefficient values were averaged, and the results are shown in Table 8. The curves obtained were fitted with a 1-component diffusion model.

Table 8: FAD characteristics and data

Sample	Radius (nm)	D (μm²/s)	T (K)
FAD in PBS	$0.8*10^{-9}$	224.22	309.15

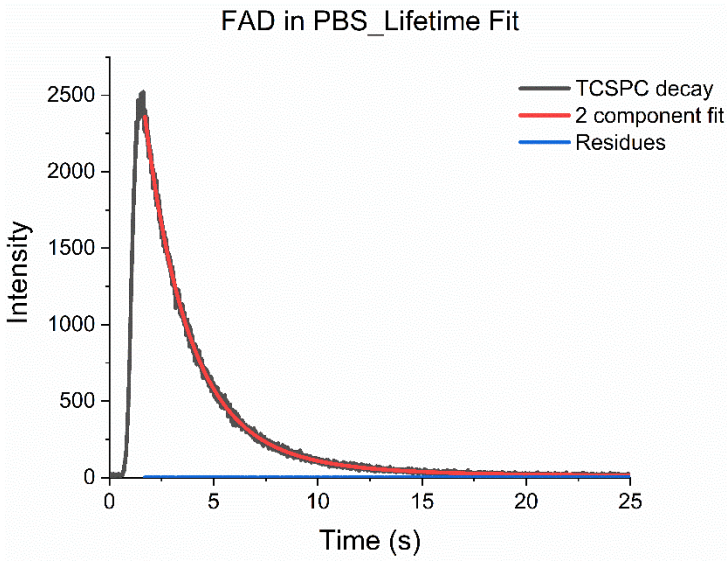

Figure 34: TCSPC decay curve of FAD at a concentration of 1.02×10^{-5} M in PBS, with a 2 component model fit overlaying experimental data.

The fluorescence lifetime decay of FAD in buffer (1.02×10^{-5} M) was fitted with a bi-exponential model. The optimal fit revealed two lifetimes of FAD in PBS – 2.1 ns and 5.2 ns (Fig 34).

2.5.8 Fluorescence lifetime imaging of mammalian cells

Cells contain 500,000 to 3,000,000 molecules of unbound FAD[147], which are involved in multiple metabolic pathways[148,149]. FAD's fluorescence lifetime inside cells highly depends on its concentration and cellular environment. Changes in its lifetime and fluorescence intensity could result from changing pH, redox states, temperature, structural conformations and interactions with other metabolites[150]. STS induces apoptosis in cancer cells by inhibiting protein kinases. This inhibition triggers mitochondrial dysfunction, leading to changes in the cellular redox state, including increased production of reactive oxygen species (ROS) and a shift towards a more acidic intracellular environment. FAD, being highly sensitive to fluctuations in redox states, pH and other microenvironmental changes, undergoes conformational alterations that affect its fluorescence lifetime and intensity. Monitoring these alterations in FAD's fluorescence characteristics makes it possible to track early signs of mitochondrial dysfunction, redox imbalance and cell progression towards cell death.

In this study, cells were treated with STS at two different concentrations, and fluorescence lifetime imaging microscopy (FLIM) was performed on these cells (refer to Appendix B.8, table B6). Region of interests (ROI) were created on the FLIM images, and these ROIs were fitted with the 2 lifetimes derived from the FAD decay curve in PBS to analyse the fluorescence lifetime properties of the treated cells. This approach demonstrated that the lifetimes of cellular autofluorescence aligned with the lifetimes derived for FAD in a buffer. Therefore, it was concluded that it is FAD which contributes to the autofluorescence. Refer to data acquisition parameters below:

FLIM images of cells treated with high and low concentrations of STS (100 µM and 1 µM) were acquired at different time points – 0h, 1h and 2h. FLIM images of A549 cells are shown in Fig 35. A similar analysis was performed on all other cell lines. Based on TCSPC results from FAD in buffer, it was assumed that the increase in fluorescence intensity after STS treatment was primarily due to FAD molecules. Thus, ROIs were selected within the acquired FLIM images of treated cells to evaluate spatially resolved fluorescence lifetimes. The lifetimes of 2.1 ns and 5.2 ns, derived from the FAD decay curve in PBS, were applied to the FLIM

images for analysis. These lifetimes were then mapped onto the images of the cells, generating a pseudo-colour representation where the colour scale corresponds to the distribution of these lifetimes across the image. The increasing contribution of molecules exhibiting longer lifetimes (5.2 ns) was observed when low drug concentrations (1 µM) were compared with high drug concentrations (100 µM) during the same induction period (Fig 36). The number of extracellular fluorescent species is higher in cells treated with 100 µM staurosporine for 2h than cells treated with 1 µM. This concentration-dependent increase in autofluorescence response was observed in all 3 cancer cell lines and HEK cells.

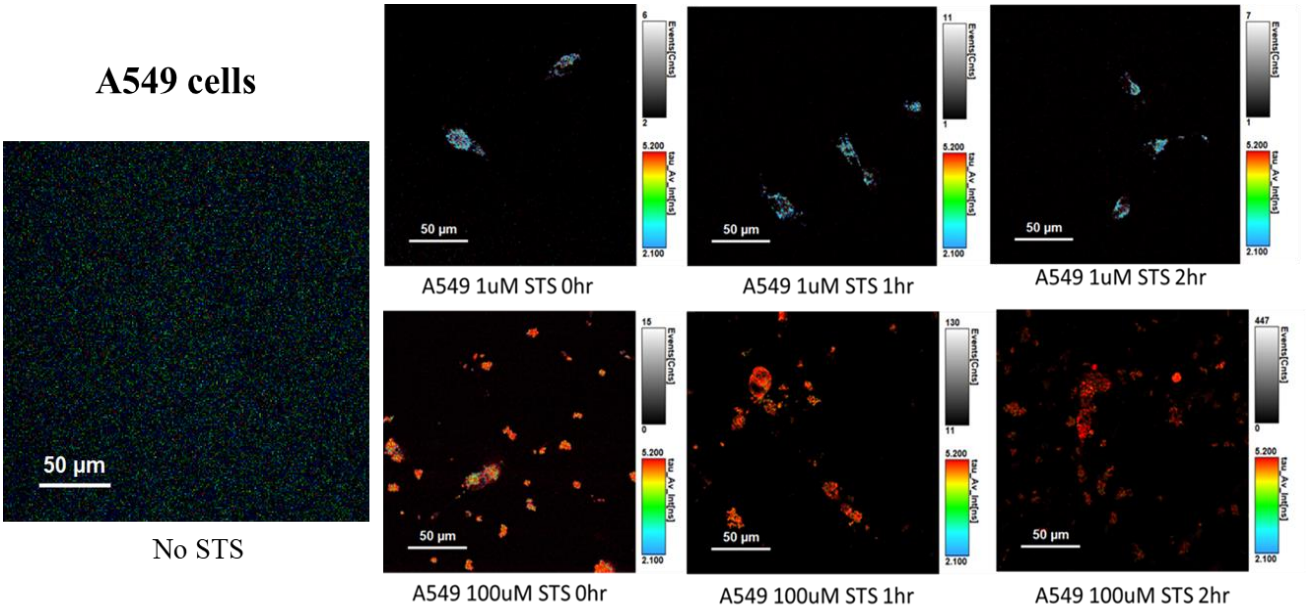

Figure 35: FLIM analysis of FAD lifetimes in A549 cancer cells. The colour bar represents the corresponding fluorescence lifetime values for each pixel in the image. The lifetime values are also mapped onto the extracellular regions (PBS) outside the cells, as shown in the images. Scale bar: 50 µm.

ROIs were typically selected from single cells for fluorescence lifetime analysis. For each of the four cell lines, 5-6 ROIs were chosen to represent the cellular response. Multiple ROIs (5-6 per cell line) were selected from different cells within the population. The data from the selected ROIs were analysed by applying the fixed lifetimes, determined from the FAD decay curve in the buffer to the FLIM images. The contributions of these lifetimes were then quantified in terms of their respective amplitudes. At 100 µM STS, 75% of FAD components in cells exhibited a longer lifetime of 5.2 ns (A_1), and 25% had a shorter lifetime of 2.1 ns (A_2). A reverse trend was observed for 1 µM STS treated cells (Fig 36). FAD exhibit a higher % of longer lifetimes in cells treated with high drug concentrations. The relative contribution of each lifetime component (A_1 and A_2) to the total fluorescence signal was calculated by expressing

their amplitudes as a percentage of the total photon counts, normalised to 100%. These results were consistent across all tested cell lines.

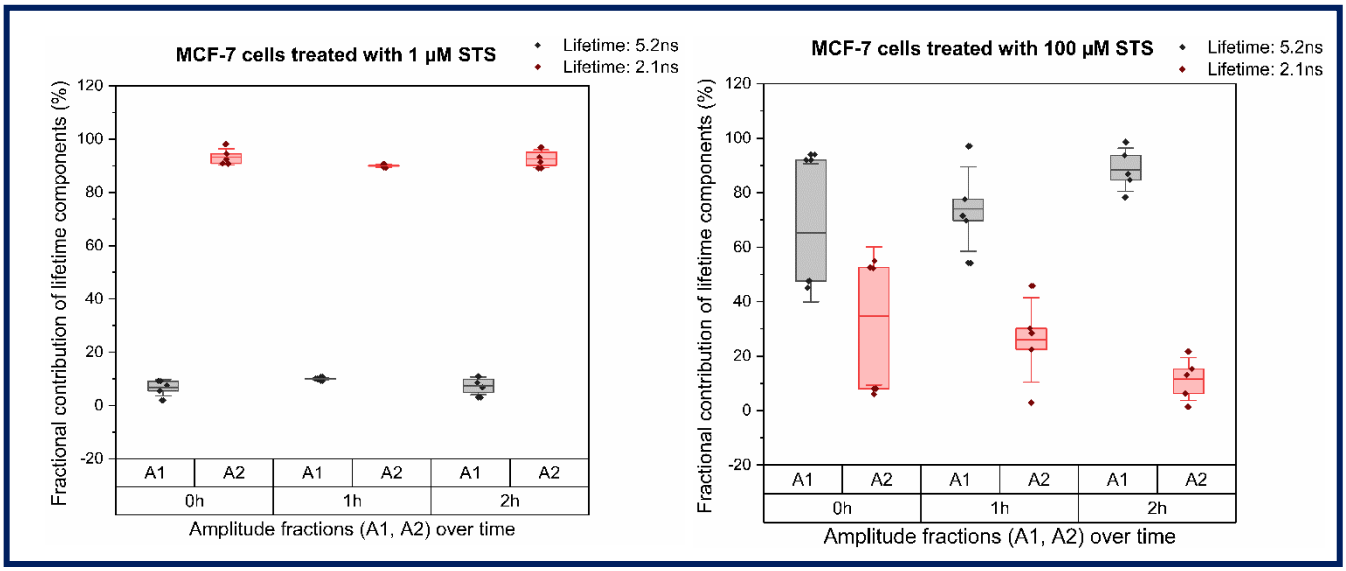

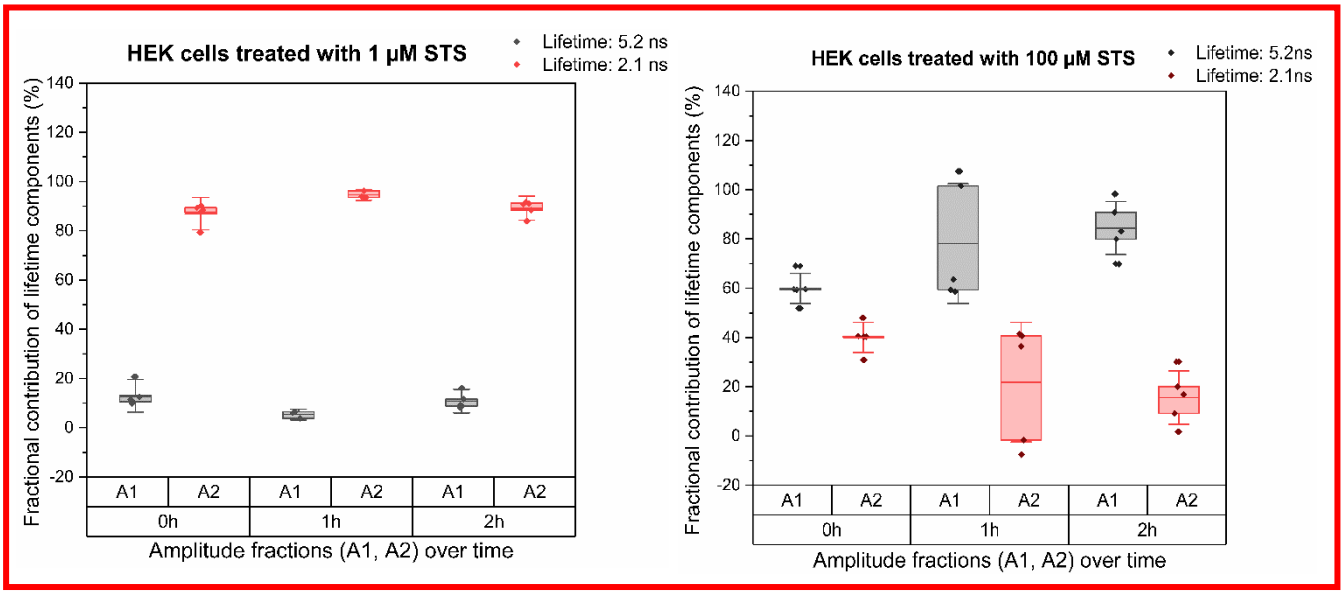

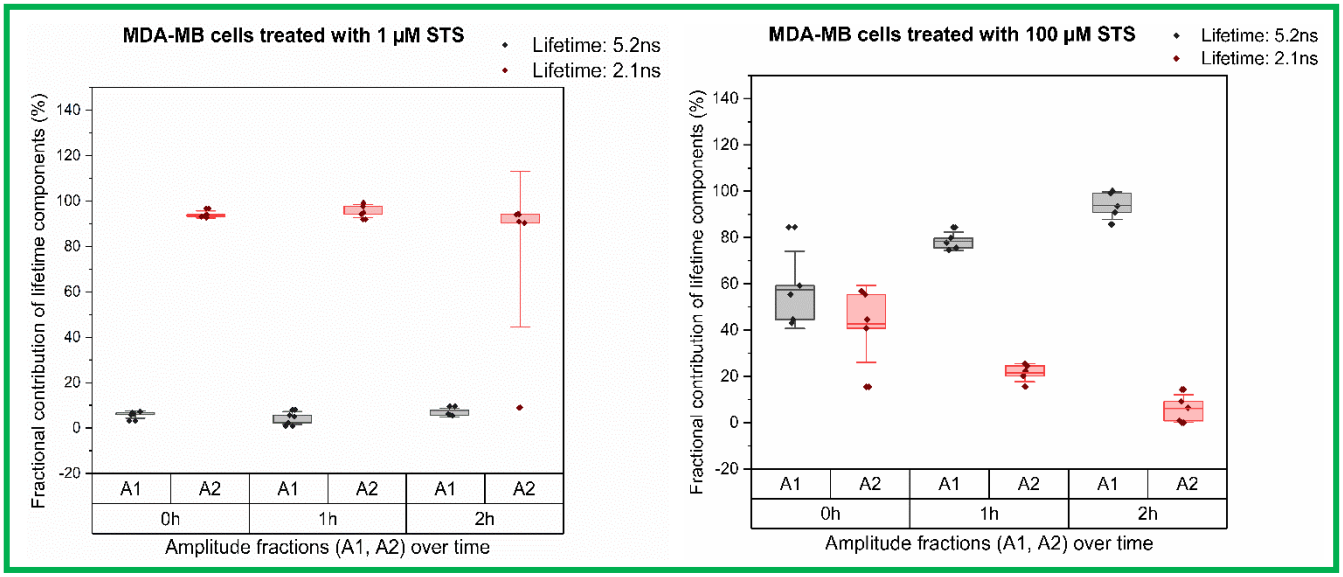

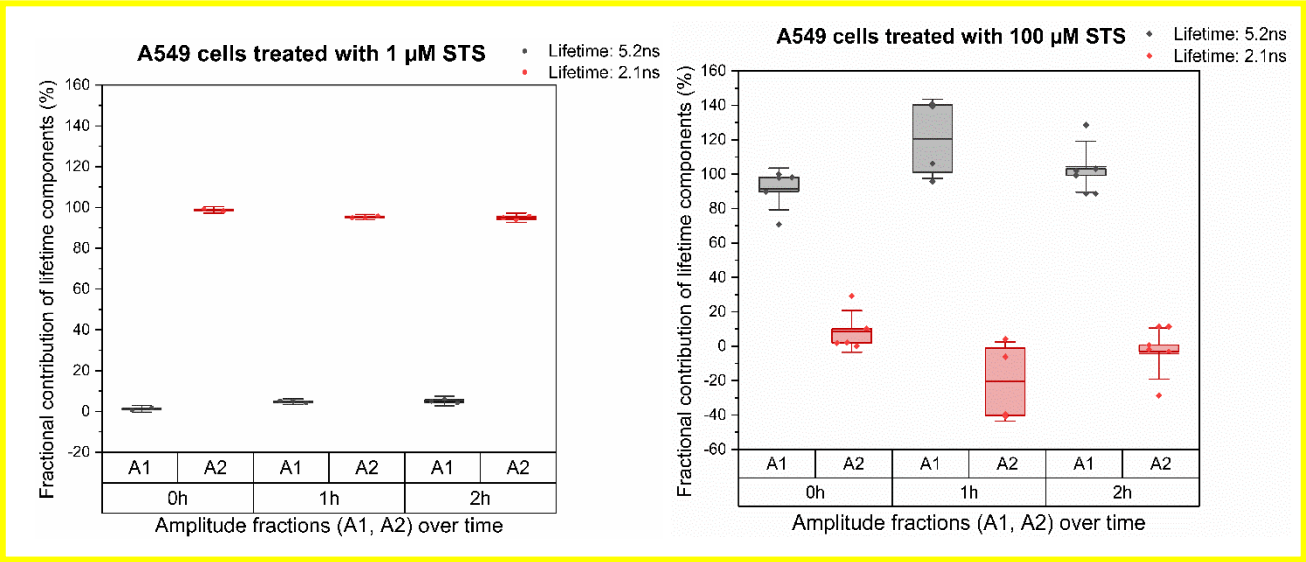

Figure 36: FLIM fitted FAD lifetimes in cancer cells – MCF (blue box), HEK (red box), A549 (yellow box) and MDA-MB (green box). The colour bar shows the corresponding lifetime fitting on each pixel in the image cells. Lifetime fitting also highlights coloured components in PBS (outside cells). Scale bar: 50 µm.

FAD is primarily located in the mitochondria, where it is bound and exhibits shorter fluorescence lifetimes. However, increased FAD autofluorescence in the cytoplasm indicates mitochondrial membrane damage. Previous studies have shown that increased cytoplasmic FAD is associated with mitochondrial damage in rat cardiac myocytes[151], a finding that is consistent with my data in cancer cells. The shift toward longer fluorescence lifetimes is linked with mitochondrial dysfunction and apoptosis, especially at higher STS concentrations. Shorter fluorescence lifetimes reflect FAD in its bound state within the mitochondria, while longer lifetimes correspond to free, unstacked FAD in the cytoplasm, which appears in early apoptosis[152]. Additionally, fluorescence lifetime between 2-4 ns is characteristic of the oxidised form of FAD called FAD_{ox}, whereas lifetimes in the range of a few picoseconds (5-9 ps) suggest the reduced form of FAD ($FADH_2$)[153]. Fig. 37 illustrates how FAD in mitochondria exhibits shorter lifetimes due to its bound state. In contrast, the unstacked, free FAD in the cytoplasm shows longer lifetimes, especially in STS-induced apoptosis.

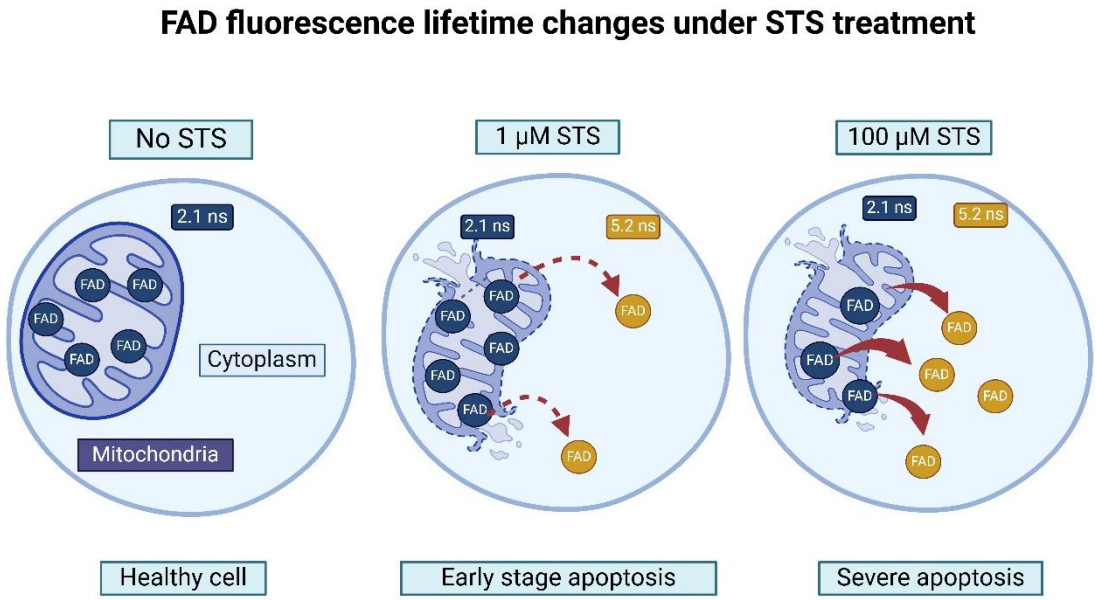

Figure 37: Schematic representation of FAD localization and fluorescence lifetime changes upon STS treatment. The figure illustrates the change in FAD fluorescence lifetimes in response to varying concentrations of STS, reflecting cellular changes. In healthy cells (control), FAD is predominantly bound to mitochondria, exhibiting a shorter lifetime of 2.1 ns, indicating stable mitochondrial function. Treatment with 1 µM STS results in a small proportion (25%) of FAD shifting to the cytoplasm (dotted red arrow), while most remain bound in mitochondria, suggesting early signs of cellular stress. Upon treatment with 100 µM STS, over 75% of FAD is released into the cytoplasm (shown by the increased number of solid red arrows), exhibiting a longer lifetime of 5.2 ns, indicative of mitochondrial dysfunction. No quantifiable change in FAD numbers is observed across conditions, as represented by consistent shape and size of FAD molecules in all three conditions.

2.5.9 Conclusion

Cells are continuously producing autofluorescent molecules. Under stress – however – these molecules change their conformation, thus changing their fluorescent properties. Staurosporine induced cell stress in four cancer cell lines within 2 hours of administration at 100 µM, increasing fluorescence intensity both inside and outside the cells. This was confirmed using confocal microscopy. Analysis of confocal images using Imaris was used to obtain the fluorescence intensities – inside and outside the cells. Treatment with staurosporine led to the formation of aggregate-like structures outside cells, which were fluorescent.

The autofluorescence observed in the cells upon excitation with a 488 nm laser was attributed to FAD, as its excitation falls within the same wavelength range. This was also tested with HPLC analysis. With FLIM, 2 characteristic lifetimes of FAD, i.e. 2.1 ns and 5.2 ns, were measured in the buffer. These lifetimes were then used to fit the FLIM data obtained from STS treatment in different cell lines for two concentrations. FAD exists in longer lifetimes (5.2 ns) in a free state (at 100 μM), whereas bound conformations of the molecules usually exhibit shorter lifetimes (2.1 ns) in cells (at 1 μM).

While the results from this study point to FAD as a significant contributor to the induced autofluorescence in response to STS, the precise mechanism remains unclear. For example, the identification and characterisation of extracellular species, their concentration, and the mechanism of STS interactions with intracellular environments in different cancer types remain to be studied. Further studies involving advanced spectroscopic techniques and molecular simulations could help understand the relationship between STS and increased cellular autofluorescence, providing deeper insights into changes in autofluorescence.

3 Summary and Conclusions

Understanding the response of cells to stress, whether at the macroscopic levels in humans or at the microscopic level within individual cells, is crucial for uncovering how cellular processes are altered in disease states, particularly in cancer. While traditional approaches focus on biological markers and pathways, this research underscores the importance of studying biophysical changes such as intracellular viscosity, diffusion coefficients and fluorescence lifetime to provide critical insight into mechanisms of cell adaptation, survival and death.

My thesis showed that analysis of stress-induced changes in the biophysical properties of cells during prolonged starvation or mitochondrial stress allows us to understand quantitatively how cells respond to stress at the nanoscale to survive. Key findings from this research include:

I. **Starvation-induced biophysical changes:**

   a. Increased diffusion hindrance: Starvation reduces GFP molecular diffusion by four-fold in the cytoplasm, indicating significant changes in the cellular environment that affect transport and molecular interactions.

   b. Compartmentalised stress response: During prolonged starvation, diffusion hindrance differs between the cytoplasm and nucleus. While no significant hindrance to GFP diffusion is observed in the nucleus, the cytoplasm experiences an increase in diffusion hindrance. This differential response highlights how cells specifically regulate stress across different cellular compartments, thereby safeguarding the nucleus, which is critical for cellular function.

   c. Cytoplasmic mesh structure shift: Starvation shifts the cytoplasmic mesh structure from liquid-like to gel-like, reducing pore size from 100 nm to 30 nm and causing cell shrinkage, which is linked to water efflux.

   d. Cytoplasmic restructuring during gene knockout: Gene knockout of a transmembrane protein involved in cell volume homeostasis alters the cytoplasmic nanostructure, resulting in changes to the diffusion patterns of GFP inside cells. This study demonstrates that diffusion becomes non-uniform, even at the small scale of a few hundred nanometres (~ size of the confocal volume).

II. **Mitochondrial stress and autofluorescence lifetimes:**

a. Increased autofluorescence during drug-induced mitochondrial stress: High STS concentrations lead to increased autofluorescence in four cancer cell lines. This enhanced autofluorescence following drug administration may serve as a potential marker of mitochondrial stress.

b. Fluorescence lifetime analysis of FAD: Mitochondrial stress and its effect on cellular autofluorescence were discussed by examining the fluorescence lifetimes of an abundantly present autofluorescent molecule – FAD. Shorter and longer lifetimes of FAD reflect different cellular states – Shorter lifetimes indicate bound FAD interacting with proteins or cellular compartments, while longer lifetimes reflect unbound, freely diffusing FAD available for downstream interactions during stress response.

c. Consistent lifetime patterns across cell types: FAD fluorescence lifetime patterns, characterized by 5.2 ns and 2.1 ns, remain consistent across various cell types. At lower STS concentrations (1 μM), FAD shows a shorter lifetime (2.1 ns), whereas at higher concentrations (100 μM), it exhibits a longer lifetime (5.2 ns). These lifetime changes were observed across all cell lines, suggesting that FAD lifetimes may serve as markers of mitochondrial stress during STS treatment.

Stress conditions like starvation and mitochondrial dysfunction alter intracellular diffusion, viscosity and autofluorescence, affecting cellular mechanical properties. For instance, higher viscosity results in stiffer, less compressible and shrunk cells (due to water efflux), which are more prone to movement in microfluidics chambers, offering potential applications in cell sorting based on biophysical traits rather than biological markers. This method can distinguish viable cells from dying or stressed cells and improve cell separation techniques. Additionally, autofluorescence lifetimes analysis during mitochondrial damage can track mitochondrial dysfunction and detect early cellular injury before irreversible damage occurs. This study highlights the importance of considering biophysical changes in cellular stress responses, paving the way for novel, efficient and non-invasive biomedical technologies.

References

1. Del Giudice, M. *et al.* What Is Stress? A Systems Perspective. *Integr Comp Biol*. 2018, **58**, 737-745.

2. Mohr, S.M., Bagriantsev, S.N. & Gracheva, E.O. Cellular, Molecular, and Physiological Adaptations of Hibernation: The Solution to Environmental Challenges. *Annu. Rev. Cell Dev. Biol. 2020,* **36**, 315-338.

3. Zelenka, J., Koncošová, M. & Ruml, T. Targeting of stress response pathways in the prevention and treatment of cancer. *Biotechnology Advances* 2018, vol. **36** 583–602.

4. Fulda, S., Gorman, A. M., Hori, O. & Samali, A. Cellular stress responses: Cell survival and cell death. *International Journal of Cell Biology,* 2010, vol **12**, issue 9, 2470.

5. Shi, H. *et al.* Starvation induces shrinkage of the bacterial cytoplasm. *Proceedings of the National Academy of Sciences* 2021, **118**, e2106638118.

6. Duveau, F. *et al.* Yeast cell responses and survival during periodic osmotic stress are controlled by glucose availability. *Elife* 2023, **12**, e72445.

7. Joyner, R. P. *et al.* A glucose-starvation response regulates the diffusion of macromolecules. *Elife* 2016, **3**, e02124.

8. Persson, L. B., Ambati, V. S. & Brandman, O. Cellular Control of Viscosity Counters Changes in Temperature and Energy Availability. *Cell* 2020, **183**, 1572-1585.e16.

9. Rabouille, C. & Alberti, S. Cell adaptation upon stress: the emerging role of membrane-less compartments. *Current Opinion in Cell Biology* 2017, vol. **47** 34–42.

10. Sekine, Y., Houston, R. & Sekine, S. Cellular metabolic stress responses via organelles. *Experimental Cell Research* 2021, vol. **400**, 112515.

11. Shen, M. & Kang, Y. Stresses in the metastatic cascade: Molecular mechanisms and therapeutic opportunities. *Genes Dev* 2020, **34**, 1577–1598.

12. Naveed, S., Aslam, M. & Ahmad, A. Starvation based differential chemotherapy: A novel approach for cancer treatment. *Oman Med J* 2014, **29**, 391–398.

13. Ganapathy-Kanniappan, S. & Geschwind, J.-F. H. *Tumor Glycolysis as a Target for Cancer Therapy: Progress and Prospects* 2013, **12**, 152.

14. Hankir, M. K., Hoffmann, A. & Seyfried, F. Starving cancer into submission by activating BAT. *Cell Metab* 2020, **34**, 1428–1430.

15. Vander Heiden, M. G. & DeBerardinis, R. J. Understanding the Intersections between Metabolism and Cancer Biology. *Cell* 2017, vol. 168 657–669.

16. Xu, T. *et al.* Oxidative Stress in Cell Death and Cardiovascular Diseases. *Oxid Med Cell Longev* 2019, 1–11.

17. Ulaganathan, T., Perales, S., Mani, S., Baskhairoun, B. A. & Rajasingh, J. Pathological implications of cellular stress in cardiovascular diseases. *Int J Biochem Cell Biol* 2023, **158**, 106397.

18. Zheng, Y., Nguyen, J., Wei, Y. & Sun, Y. Recent advances in microfluidic techniques for single-cell biophysical characterization. *Lab on a Chip* 2013, vol. **13** 2464–2483.

19. Morrow, C. S. *et al.* Autofluorescence is a biomarker of neural stem cell activation state. *BioRxiv,* 2022, preprint - 10.1101/2022.12.14.520430.

20. Black, D. *et al.* Characterization of autofluorescence and quantitative protoporphyrin IX biomarkers for optical spectroscopy-guided glioma surgery. *Sci Rep* 2021, **11**, 1.

21. García, M. J., Kamaid, A. & Malacrida, L. Label-free fluorescence microscopy: revisiting the opportunities with autofluorescent molecules and harmonic generations as biosensors and biomarkers for quantitative biology. *Biophysical Reviews* 2023, vol. **15** 709–719.

22. Sozański, K. *et al.* Small Crowders Slow Down Kinesin-1 Stepping by Hindering Motor Domain Diffusion. *Phys Rev Lett* 2015, **115**, 218102.

23. Li, B. *et al.* Intracellular transport is accelerated in early apoptotic cells. *Proc Natl Acad Sci U S A* 2018, **115**, 12118–12123.

24. Kwapiszewska, K. *et al.* Nanoscale Viscosity of Cytoplasm Is Conserved in Human Cell Lines. *Journal of Physical Chemistry Letters* 2020, **11**, 6914–6920.

25. Kwapiszewska, K. *et al.* Determination of oligomerization state of Drp1 protein in living cells at nanomolar concentrations. *Sci Rep* 2019, **9**, 1.

26. Étienne, J. *et al.* Cells as liquid motors: Mechanosensitivity emerges from collective dynamics of actomyosin cortex. *Proc Natl Acad Sci U S A* 2015, **112**, 2740–2745.

27. Bulthuis, E. P. *et al.* Stress-dependent macromolecular crowding in the mitochondrial matrix. *EMBO J* 2023, **42**, 1.

28. Kitamura, A. *et al.* Increased intracellular crowding during hyperosmotic stress. *Sci Rep* 2023, **13**.

29. Zacharioudaki, D. E., Fitilis, I. & Kotti, M. Review of Fluorescence Spectroscopy in Environmental Quality Applications. *Molecules* 2022, vol. **27**, 3390.

30. Covarrubias, A. J., Perrone, R., Grozio, A. & Verdin, E. NAD+ metabolism and its roles in cellular processes during ageing. *Nature Reviews Molecular Cell Biology* 2021, vol. **22** 119–141.

31. Theyel, B. B., Llano, D. A., Issa, N. P., Mallik, A. K. & Sherman, S. M. In vitroimaging using laser photostimulation with flavoprotein autofluorescence. *Nat Protoc* 2011, **6**, 502–508.

32. Galbán, J., Sanz-Vicente, I., Navarro, J. & De Marcos, S. The intrinsic fluorescence of FAD and its application in analytical chemistry: A review. *Methods and Applications in Fluorescence* 2016, vol. **4**, 1-18.

33. Cannon, T. M. *et al.* Characterization of NADH fluorescence properties under one-photon excitation with respect to temperature, pH, and binding to lactate dehydrogenase. *OSA Contin* 2021, **4**, 1610.

34. Kolenc, O. I. & Quinn, K. P. Evaluating cell metabolism through autofluorescence imaging of NAD(P)H and FAD. *Antioxidants and Redox Signaling* 2019, vol. **30** 875–889.

35. Chosrowjan, H., Taniguchi, S., Mataga, N., Tanaka, F. & Visser, A. J. W. G. The stacked flavin adenine dinucleotide conformation in water is fluorescent on picosecond timescale. *Chem Phys Lett* 2003, **378**, 354–358.

36. Gooz, M. & Maldonado, E. N. Fluorescence microscopy imaging of mitochondrial metabolism in cancer cells. *Front Oncol* 2023, **13**, 1.

37. Walsh, A. J. *et al.* Classification of T-cell activation via autofluorescence lifetime imaging. *Nat Biomed Eng* 2020, **5**, 77–88.

38. Wang, H.-W., Wei, Y.-H. & Guo, H.-W. *Anti-Cancer Agents in Medicinal Chemistry*. 2009, vol. 9, 1-10.

39. Xu, H. N., Tchou, J., Feng, M., Zhao, H. & Li, L. Z. Optical redox imaging indices discriminate human breast cancer from normal tissues. *J Biomed Opt* 2016, **21**, 114003.

40. Xu, H. N., Tchou, J. & Li, L. Z. Redox Imaging of Human Breast Cancer Core Biopsies. *Acad Radiol* 2013, **20**, 764–768.

41. White, A. T. & Schenk, S. Intracellular Signal for Skeletal Muscle Adaptation NAD /NADH and skeletal muscle mitochondrial adaptations to exercise. *Am J Physiol Endocrinol Metab* 2012, **303**, 308–321.

42. Giancaspero, T. A. *et al.* FAD synthesis and degradation in the nucleus create a local flavin cofactor pool. *Journal of Biological Chemistry* 2013, **288**, 29069–29080.

43. Datta, R., Heaster, T. M., Sharick, J. T., Gillette, A. A. & Skala, M. C. Fluorescence lifetime imaging microscopy: fundamentals and advances in instrumentation, analysis, and applications. *J Biomed Opt* 2020, **25**, 1.

44. Surre, J. *et al.* Strong increase in the autofluorescence of cells signals struggle for survival. *Sci Rep* 2018, **8**, (2018).

45. Surre, J. *et al.* Strong increase in the autofluorescence of cells signals struggle for survival. *Sci Rep* **8**, 12088.

46. Shirmanova, M. V. *et al.* Insight into redox regulation of apoptosis in cancer cells with multiparametric live-cell microscopy. *Sci Rep* 2022, **12**, 1, 20495.

47. Hibbs, A. R. Confocal Microscopy for Biologists. *Confocal Microscopy for Biologists Springer US*, 2004, chapter 3.

48. Shashkova, S. & Leake, M. C. Single-molecule fluorescence microscopy review: Shedding new light on old problems. *Bioscience Reports* 201, vol. **37**, BSR20170031.

49. Yu, L. *et al.* A Comprehensive Review of Fluorescence Correlation Spectroscopy. *Frontiers in Physics* 2021, vol. 9, 644450.

50. Berlin, S. *et al. Springer Series in* CHEMICAL PHYSICS Physics and Astronomy. http://www.springer.de/phys/.

51. Kim, S. A., Heinze, K. G. & Schwille, P. Fluorescence correlation spectroscopy in living cells. *Nat Methods* 2007, **4**, 963–973.

52. Joseph R. Lakowicz, Topics in Fluorescence Spectroscopy Volume 1 Techniques. Vol **1**.

53. Zinkernagel, M. & Dysli, C. Fluorescence Lifetime Imaging Ophthalmoscopy, *Progress in retinal and eye research* 2018, vol. 63, 1-20.

54. Datta, R., Heaster, T. M., Sharick, J. T., Gillette, A. A. & Skala, M. C. Fluorescence lifetime imaging microscopy: fundamentals and advances in instrumentation, analysis, and applications. *J Biomed Opt* 2020, **25**, 1.

55. Kolenc, O. I. & Quinn, K. P. Evaluating cell metabolism through autofluorescence imaging of NAD(P)H and FAD. *Antioxidants and Redox Signaling* 2019, vol. **30** 875–889.

56. Berezin, M. Y. & Achilefu, S. Fluorescence lifetime measurements and biological imaging. *Chem Rev* 2010, **110**, 2641–2684.

57. Imamura, H. *et al.* Visualization of ATP Levels inside Single Living Cells with Fluorescence Resonance Energy Transfer-Based Genetically Encoded Indicators. *PNAS* 2009, 106, 15651-15656.

58. Depaoli, M. R. *et al.* Real-Time Imaging of Mitochondrial ATP Dynamics Reveals the Metabolic Setting of Single Cells. *Cell Rep* 2018, **25**, 501-512.e3.

59. Greiner, J. V. & Glonek, T. Intracellular atp concentration and implication for cellular evolution. *Biology (Basel)* 2021, **10**, 1.

60. Zunica, E. R. M., Axelrod, C. L., Gilmore, L. A., Gnaiger, E. & Kirwan, J. P. The bioenergetic landscape of cancer. *Mol Metab* 20204, **86**, 101966.

61. Pan, W., Geng, X. & Zhang, C. Cancer Cells and Effects of Glucose Starvation. In *Handbook of Famine, Starvation, and Nutrient Deprivation, Springer* 2019, 2169–2184.

62. Kaloyianni, M. & Baker, G. F. The Effect of ATP-Depletion on the Inhibition of Glucose Exits from Human Red Cells. *Biochimica et Biophysica Acta* 1998, vol. 1369.

63. Fiorillo, M., Ózsvári, B., Sotgia, F. & Lisanti, M. P. High ATP Production Fuels Cancer Drug Resistance and Metastasis: Implications for Mitochondrial ATP Depletion Therapy. *Front Oncol* 2021, **11**, 634879.

64. Bhowmick, T., Biswas, S. & Mukherjee, A. Cellular response during cellular starvation: A battle for cellular survivability. *Cell Biochem Funct* 2024, **42**, 1.

65. Alimov, I. *et al.* Bile acid analogues are activators of pyrin inflammasome. *Journal of Biological Chemistry* 2019, **294**, 3359–3366.

66. Kopra, K. *et al.* Homogeneous luminescent quantitation of cellular guanosine and adenosine triphosphates (GTP and ATP) using QT-LucGTP & amp;ATP assay. *Anal Bioanal Chem* 2023, **415**, 6689–6700.

67. Imamura, H. *et al.* Visualization of ATP levels inside single living cells with fluorescence resonance energy transfer-based genetically encoded indicators. *Proceedings of the National Academy of Sciences* 2009, **106**, 15651–15656.

68. Liu, J. *et al.* CRL4ACRBN E3 ubiquitin ligase restricts BK channel activity and prevents epileptogenesis. *Nat Commun* 2014, **5**, 3924.

69. Mao, D., Lü, S., Zhang, X. & Long, M. Mechanically Regulated Outside-In Activation of an I-Domain-Containing Integrin. *Biophys J* 2020, **119**, 966–977.

70. Shen, Y. *et al.* Genetically encoded fluorescent indicators for imaging intracellular potassium ion concentration. *Commun Biol* 2019, **2**, 18.

71. Arai, S. *et al.* RGB-Color Intensiometric Indicators to Visualize Spatiotemporal Dynamics of ATP in Single Cells. *Angewandte Chemie International Edition* 2018, **57**, 10873–10878.

72. Liu, X. *et al.* Sensitive detection of superoxide anion released from living cells using silver nanoparticles and functionalized multiwalled carbon nanotube composite. *Sens Actuators B Chem* 2017, **252**, 503–510.

73. Singh, A., Sinha, S., Kaur, R., Kaur, N. & Singh, N. Rhodamine based organic nanoparticles for sensing of Fe3+ with high selectivity in aqueous medium: Application to iron supplement analysis. *Sens Actuators B Chem* 2014, **204**, 617–621.

74. Parra, M., Gil, S., Gaviña, P. & Costero, A. M. Mesoporous Silica Nanoparticles in Chemical Detection: From Small Species to Large Bio-Molecules. *Sensors* 2021, **22**, 261.

75. Lee, J., Kim, S., Kim, T. H. & Lee, S. H. A ratiometric fluorescence sensor based on enzymatically activatable micellization of TPE derivatives for quantitative detection of alkaline phosphatase activity in serum. *RSC Adv* 2020, **10**, 26888–26894.

76. Liu, J. & Lu, Y. Fast Colorimetric Sensing of Adenosine and Cocaine Based on a General Sensor Design Involving Aptamers and Nanoparticles. *Angewandte Chemie International Edition* 2006, **45**, 90–94.

77. Liu, J., Cao, Z. & Lu, Y. Functional Nucleic Acid Sensors. *Chem Rev* 2009, **109**, 1948–1998.

78. Li, T. *et al.* CRISPR/Cas9 therapeutics: progress and prospects. *Signal Transduct Target Ther* 2023, **8**, 36.

79. Mengstie, M. A. & Wondimu, B. Z. Mechanism and Applications of CRISPR/Cas-9-Mediated Genome Editing. *Biologics* 2021, vol. **15**, 353–361.

80. Aljabali, A. A. A., El-Tanani, M. & Tambuwala, M. M. Principles of CRISPR-Cas9 technology: Advancements in genome editing and emerging trends in drug delivery. *J Drug Deliv Sci Technol* 2024, **92**, 105338.

81. Abdelnour, S. A., Xie, L., Hassanin, A. A., Zuo, E. & Lu, Y. The Potential of CRISPR/Cas9 Gene Editing as a Treatment Strategy for Inherited Diseases. *Frontiers in Cell and Developmental Biology* 2021, vol. **9**, 699597.

82. Wang, S. W. *et al.* Current applications and future perspective of CRISPR/Cas9 gene editing in cancer. *Molecular Cancer* 2022, vol. 21, 12943-022-01518-8

83. Doudna, J. A. & Charpentier, E. The new frontier of genome engineering with CRISPR-Cas9. *Science* 2014, **346**, 6213, 1258096.

84. Urnov, F. D., Rebar, E. J., Holmes, M. C., Zhang, H. S. & Gregory, P. D. Genome editing with engineered zinc finger nucleases. *Nat Rev Genet* 2010, **11**, 636–646.

85. Christian, M. *et al.* Targeting DNA Double-Strand Breaks with TAL Effector Nucleases. *Genetics* 2010, **186**, 757–761.

86. Silva, G. *et al.* Meganucleases and Other Tools for Targeted Genome Engineering: Perspectives and Challenges for Gene Therapy. *Curr Gene Therapy* 2011, **11**, 11–27.

87. Komor, A. C., Kim, Y. B., Packer, M. S., Zuris, J. A. & Liu, D. R. Programmable editing of a target base in genomic DNA without double-stranded DNA cleavage. *Nature* 2016, **533**, 420–424.

88. Anzalone, A. V. *et al.* Search-and-replace genome editing without double-strand breaks or donor DNA. *Nature* 2019, **576**, 149–157.

89. Golkaram, M., Hellander, S., Drawert, B. & Petzold, L. R. Macromolecular Crowding Regulates the Gene Expression Profile by Limiting Diffusion. *PLoS Comput Biol* 2016, **12**, e1004685.

90. Gonzalez-Molina, J. *et al.* Extracellular fluid viscosity enhances liver cancer cell mechanosensing and migration. *Biomaterials* 2018, **177**, 113–124.

91. Rodríguez-Sevilla, P. *et al.* Upconverting Nanorockers for Intracellular Viscosity Measurements During Chemotherapy. *Adv Biosyst* 2019, **3**, 1–9.

92. Sohrabi Kashani, A. & Packirisamy, M. Cancer-nano-interaction: From cellular uptake to mechanobiological responses. *Int J Mol Sci* 2021, **22**, 191.

93. Baer, A. *et al.* The Stokes–Einstein–Sutherland Equation at the Nanoscale Revisited. *Small* 2024, **20**, 2303246.

94. Hink, M. A. *et al.* Structural dynamics of green fluorescent protein alone and fused with a single chain Fv protein. *Journal of Biological Chemistry* 2000, **275**, 17556–17560.

95. Biebricher, A. S. *et al.* The impact of DNA intercalators on DNA and DNA-processing enzymes elucidated through force-dependent binding kinetics. *Nat Commun* 2015, **6**, 7304.

96. Michalski, J. *et al.* Rotational and translational diffusion of biomolecules in complex liquids and HeLa cells. *Soft Matter* 2024, **20**, 5810–5821.

97. Aragón, S. R. & Pecora, R. Fluorescence correlation spectroscopy and Brownian rotational diffusion. *Biopolymers* 1975, **14**, 119–137.

98. Minchin, S. & Lodge, J. Understanding biochemistry: Structure and function of nucleic acids. *Essays in Biochemistry* 2019, vol. **63** 433–456.

99. Rietscher, K. & Magin, T. M. Mechanobiology: Border crosstalk protects the nucleus from stress. *Current Biology* 2023, vol. **33** R1002–R1004.

100. Bubak, G. *et al.* Quantifying Nanoscale Viscosity and Structures of Living Cells Nucleus from Mobility Measurements. *Journal of Physical Chemistry Letters* 2021, **12**, 294–301.

101. Levitt, J. A. *et al.* Membrane-bound molecular rotors measure viscosity in live cells via fluorescence lifetime imaging. *Journal of Physical Chemistry C* 2009, **113**, 11634–11642.

102. Yu, I. *et al.* Biomolecular interactions modulate macromolecular structure and dynamics in atomistic model of a bacterial cytoplasm. *Elife* 2017, e19274.

103. Lang, F., Vallon, V., Knipper, M. & Wangemann, P. Functional significance of channels and transporters expressed in the inner ear and kidney. *American Journal of Physiology-Cell Physiology* 2007, **293**, C1187–C1208.

104. Poroca, D. R., Pelis, R. M. & Chappe, V. M. ClC Channels and Transporters: Structure, Physiological Functions, and Implications in Human Chloride Channelopathies. *Front Pharmacol* 2017, **8**, 601.

105. Malekova, L. *et al.* Inhibitory effect of DIDS, NPPB, and phloretin on intracellular chloride channels. *Pflugers Arch* 2007, **455**, 349–357.

106. Benítez-Rangel, E., López-Méndez, M., García, L. & Guerrero-Hernández, A. DIDS (4,4'-Diisothiocyanatostilbene-2,2'-disulfonate) directly inhibits caspase activity in HeLa cell lysates. *Cell Death Discov* 2015, **1**, 15037.

107. Agasty, A., Wisniewska, A., Kalwarczyk, T., Koynov, K. & Holyst, R. Macroscopic Viscosity of Polymer Solutions from the Nanoscale Analysis. *ACS Appl Polym Mater* 2021, **3**, 2813–2822.

108. Sozański, K., Wiśniewska, A., Kalwarczyk, T. & Hołyst, R. Activation Energy for Mobility of Dyes and Proteins in Polymer Solutions: From Diffusion of Single Particles to Macroscale Flow. *Phys Rev Lett* 2013, **111**, 228301.

109. Zhou, L. *et al.* Fatty Acid Oxidation Mediated by Malonyl-CoA Decarboxylase Represses Renal Cell Carcinoma Progression. *Cancer Res* 2023, **83**, 3920–3939.

110. Schiliro, C. & Firestein, B. L. Mechanisms of Metabolic Reprogramming in Cancer Cells Supporting Enhanced Growth and Proliferation. *Cells* 2021, **10**, 1056.

111. Parlani, M., Jorgez, C. & Friedl, P. Plasticity of cancer invasion and energy metabolism. *Trends Cell Biol* 2023, **33**, 388–402 .

112. Parry, B. R. *et al.* The Bacterial Cytoplasm Has Glass-like Properties and Is Fluidized by Metabolic Activity. *Cell* 2014, **156**, 183–194.

113. Poroca, D. R., Pelis, R. M. & Chappe, V. M. ClC channels and transporters: Structure, physiological functions, and implications in human chloride channelopathies. *Frontiers in Pharmacology* 2017, vol. **8**, 151.

114. Barlassina, C. *et al.* Common genetic variants and haplotypes in renal CLCNKA gene are associated to salt-sensitive hypertension. *Hum Mol Genet* 2007, **16**, 1630–1638.

115. Imbrici, P. *et al.* Pharmacovigilance database search discloses ClC-K channels as a novel target of the AT1 receptor blockers valsartan and olmesartan. *Br J Pharmacol* 2017, **174**, 1972–1983.

116. Cappola, T. P. *et al.* Loss-of-function DNA sequence variant in the CLCNKA chloride channel implicates the cardio-renal axis in interindividual heart failure risk variation. *Proc Natl Acad Sci U S A* 2011, **108**, 2456–2461.

117. Boulos, I. *et al.* Exploring the World of Membrane Proteins: Techniques and Methods for Understanding Structure, Function, and Dynamics. *Molecules* 2023, vol. 28, 28207176

118. Sabri, A., Xu, X., Krapf, D. & Weiss, M. Elucidating the Origin of Heterogeneous Anomalous Diffusion in the Cytoplasm of Mammalian Cells. *Phys Rev Lett* 2020, **125**, 058101.

119. Speckner, K. & Weiss, M. Single-Particle Tracking Reveals Anti-Persistent Sub diffusion in Cell Extracts. *Entropy* 2021, **23**, 892.

120. Apoptotic pathways.

121. Arai, S. *et al.* RGB-Color Intensiometric Indicators to Visualize Spatiotemporal Dynamics of ATP in Single Cells. *Angewandte Chemie - International Edition* 2018, **57**, 10873–10878.

122. Tantama, M., Martínez-François, J. R., Mongeon, R. & Yellen, G. Imaging energy status in live cells with a fluorescent biosensor of the intracellular ATP-to-ADP ratio. *Nat Commun* 2013, **4**, 1.

123. Valdez, B. C. *et al. Synergism of the Anthracene-Derivative Anti-Cancer Agent Bisantrene with Nucleoside Analogs and A Bcl-2 Inhibitor in Acute Myeloid Leukemia Cells*. *Journal of Clinical & Experimental Oncology* 2021, vol. **10**.

124. Olsen, S. N. & Armstrong, S. A. It's Not What You Say But How You Say It: Targeting RNA Methylation in AML. *Mol Cell* 2020, **78**, 996–998.

125. Yap, H.-Y. *et al.* Bisantrene, an Active New Drug in the Treatment of Metastatic Breast Cancer. *Cancer Res.*1983, vol. 43, 1402-2415887.

126. Farshbaf, S. & Anzenbacher, P. Fluorimetric sensing of ATP in water by an imidazolium hydrazone based sensor. *Chemical Communications* 2019, **55**, 1770–1773.

127. Liu, E., Liu, X., Jin, Z. & Jian, F. Study on the relationship between structure and fluorescence properties of anthracene derivatives. *J Mol Struct* 2002, **1252**, 1.

128. Uejima, M. *et al.* A designed fluorescent anthracene derivative: Theory, calculation, synthesis, and characterization. *Chem Phys Lett* 2014, **602**, 80–83.

129. Huang, H. *et al.* Physiological levels of ATP negatively regulate proteasome function. *Cell Res* 2010, **20**, 1372–1385.

130. Matsson, P. & Kihlberg, J. How Big Is Too Big for Cell Permeability? *J Med Chem* 2017, **60**, 1662–1664.

131. Monici, M. Cell and tissue autofluorescence research and diagnostic applications. *In Essays Biochem*. 2005, **63**, 227–256.

132. Wang, H.-W. *et al.* Differentiation of apoptosis from necrosis by dynamic changes of reduced nicotinamide adenine dinucleotide fluorescence lifetime in live cells. *J Biomed Opt* 2008, **13**, 054011.

133. Surre, J. *et al.* Strong increase in the autofluorescence of cells signals struggle for survival. *Sci Rep* 2018, **8**, 12088.

134. Das Choudhury, S. *et al.* Stress phenotyping analysis leveraging autofluorescence image sequences with machine learning. *Front Plant Sci* 2024, **15**, 1.

135. Malsy, M., Bitzinger, D., Graf, B. & Bundscherer, A. Staurosporine induces apoptosis in pancreatic carcinoma cells PaTu 8988t and Panc-1 via the intrinsic signaling pathway. *Eur J Med Res* 2019, **24**, 28.

136. Kinnunen, P. C., Humphries, B. A., Luker, G. D., Luker, K. E. & Linderman, J. J. Characterizing heterogeneous single-cell dose responses computationally and experimentally using threshold inhibition surfaces and dose-titration assays. *NPJ Syst Biol Appl* 2024, **10**, 1.

137. Marcelli, M. *et al.* Heterogeneous apoptotic responses of prostate cancer cell lines identify an association between sensitivity to staurosporine-induced apoptosis, expression of Bcl-2 family members, and caspase activation. *Prostate* 2000, **42**, 260–273.

138. Woodward, R. B. Structure and the Absorption Spectra of α,β-Unsaturated Ketones. *J Am Chem Soc* 1941, **63**, 1123–1126.

139. STS structure.

140. Ostercamp, D. L. Vinylogous imides. II. Ultraviolet spectra and the application of Woodward's rules. *J Org Chem* 1970, **35**, 1632–1641.

141. Allinger, N. L. & Tai, J. C. Organic Quantum Chemistry. IX. The Ultraviolet Spectra of Unsaturated Hydrocarbons. Woodward's Rules [1,2]. *J Am Chem Soc* 1965, **87**, 2081–2087.

142. Lepock, J. R. Measurement of protein stability and protein denaturation in cells using differential scanning calorimetry. *Methods* 2005, **35**, 117–125.

143. Lepock, J. R. Cellular effects of hyperthermia: relevance to the minimum dose for thermal damage. *International Journal of Hyperthermia* 2003, **19**, 252–266.

144. Kozlova, A. A., Verkhovskii, R. A., Ermakov, A. V. & Bratashov, D. N. Changes in Autofluorescence Level of Live and Dead Cells for Mouse Cell Lines. *J Fluoresc* 2020, **30**, 1483–1489.

145. Gaitan, B. *et al.* Development of an Endoscopic Auto-Fluorescent Sensing Device to Aid in the Detection of Breast Cancer and Inform Photodynamic Therapy. *Metabolites* 2022, **12**, 1097.

146. Zeiri, L., Bronk, B. V., Shabtai, Y., Eichler, J. & Efrima, S. Surface-Enhanced Raman Spectroscopy as a Tool for Probing Specific Biochemical Components in Bacteria. *Appl Spectrosc* 2004, **58**, 33–40.

147. Hühner, J., Ingles-Prieto, Á., Neusüß, C., Lämmerhofer, M. & Janovjak, H. Quantification of riboflavin, flavin mononucleotide, and flavin adenine dinucleotide in mammalian model cells by CE with LED-induced fluorescence detection. *Electrophoresis* 2015, **36**, 518–525.

148. Sacchi, S., Caldinelli, L., Cappelletti, P., Pollegioni, L. & Molla, G. Structure-function relationships in human D-amino acid oxidase. *Amino Acids* 2012, vol. 43 1833–1850.

149. Vannelli, T. A., Dykman, A. & Ortiz De Montellano, P. R. The antituberculosis drug ethionamide is activated by a flavoprotein monooxygenase. *Journal of Biological Chemistry* 2002, **277**, 12824–12829.

150. Galbán, J., Sanz-Vicente, I., Navarro, J. & De Marcos, S. The intrinsic fluorescence of FAD and its application in analytical chemistry: A review. *Methods and Applications in Fluorescence* 2016, vol. **4**, 241-263.

151. Heikal, A. A. Intracellular coenzymes as natural biomarkers for metabolic activities and mitochondrial anomalies. *Biomarkers in Medicine* 2010, vol. **4** 241–263.

152. Bryanskaya, E. O. *et al.* High levels of FAD autofluorescence indicate pathology preceding cell death. *Biochim Biophys Acta Gen Subj* 2024, **1868**, 1.

153. Brennan, J. D. Preparation and Entrapment of Fluorescently Labeled Proteins for the Development of Reagentless Optical Biosensors. *J Fluoresc* 1999, **9**, 295–312.

154. **Aabiot.** Plasmid Midi AX Endotoxin-Free. Available online: https://www.aabiot.com/en/plasmid-midi-ax-endotoxin-free. Accessed : 18/02/2025.

155. **Thermo Fisher.** Product L3000001. Available online: https://www.thermofisher.com/order/catalog/product/L3000001. Accessed : 18/02/2025.

156. **Qiagen.** PCR purification kits. Available online: https://www.qiagen.com/us/resources/resourcedetail?id=a9de0fd4-e405-4bb7-b3a0-a74b336d613e&lang=en. Accessed : 18/02/2025.

157. **NEB.** NEBuilder HiFi DNA Assembly Reaction Protocol. Available online: https://www.neb.com/en/protocols/2014/11/26/nebuilder-hifi-dna-assembly-reaction-protocol. Accessed : 18/02/2025.

158. **Qiagen.** Plasmid isolation kit. Available online: https://www.qiagen.com/us/resources/resourcedetail?id=3da21fc3-a078-4665-aefe-06154db2b6d2&lang=en. Accessed : 18/02/2025.

APPENDIX A

List of abbreviations

ACC	Autocorrelation curve
ATP	Adenosine triphosphate
BSA	Bovine serum albumin
CAR	Chimeric antigen receptor
Cas	CRISPR associated protein
CLCNKA	Chloride channel-ka
CRISPR	Clustered regularly interspaced palindromic repeats
DIDS	4,4'-Diisothiocyanatostilbene-2,2'-disulfonic acid
DMEM	Dulbecco's modified eagle medium
DMSO	Dimethyl sulfoxide
DNA	Deoxyribose nucleic acid
DSB	Double stranded break
Ecoli	Escherichia coli
ER	Endoplasmic reticulum
FAD	Flavin adenine dinucleotide
FCS	Fluorescence correlation spectroscopy
FLIM	Fluorescence lifetime imaging
FMN	Flavin mononucleotide
GFP	Green fluorescent protein
HEK	Human embryonic kidney cells
HPLC	High performance liquid chromatography
HSP	Heat shock protein
LSDV	Length scale dependent viscosity

LSU Large subunit

MCF Michigan cancer foundation-7 cells

MDA Metastatic ductal adenocarcinoma of breast

MSD Mean square displacement

NA Numerical aperture

NADH Nicotinamide adenine dinucleotide

NGS NEXT generation sequencing

PAM Protospacer adjacent motif

PBS Phosphate saline buffer

RFU Relative fluorescence unit

RNA Ribose nucleic acid

ROI Region of interest

sgRNA Single guide RNA

SPAD Single photon avalanche diode

SSE Stoke-Sutherland equation

SSU Small subunit

STS Staurosporine

TCSPC Time correlated single photon counting

TRIS Tris(hydroxymethyl)aminomethane

tRNA Transfer RNA

Appendix B

Experimental procedure

B.1 Cell culture

Cells were cultured in a monolayer on the flat surface of culture flasks in complete growth media (Table B1). Cells were maintained at 5% CO_2 in an incubator (Biogenet) at 37˚C under humidified filter conditions. Cells were grown till passage five before seeding them on a 35 mm glass bottom cell culture dish for all experiments. Refer to the step-wise procedure of culturing cells below:

1. Cell culture media was removed, and cells were gently rinsed with phosphate saline buffer (2 ml in the T25 flask and 4 ml in the T75 flasks).
2. PBS was removed, and trypsin-EDTA was added to the flasks (2 ml in T25 and 4 ml in T75 flasks).
3. Cells were incubated for 3-5 min at 37 °C.
4. Cell detachment was confirmed under an inverted microscope.
5. Fresh whole media was added to cells in trypsin-EDTA (4 ml in T25 and 8 ml in T75 flasks).
6. Cells were centrifuged at 1600 g for 4-5 min to obtain a pellet, which was resuspended in fresh whole media.
7. Cell seeding for assays was performed after cell counting.
8. Approximated aliquots (30 µl – 50 µl) from the resuspended pellet were added to a new culture flask for the following passage.

Table B1: Cell culture growth media composition and respective vendors for reagen

Cell line	Media composition	Reagents	Source
Hela wild type, MCF-7, A549, MDA-MB, 769-P	DMEM (4.5 g/l) with 10% FBS, 1% L-glutamine and 1% Pen-strep.	FBS, DMEM, L-glutamine, PBS, NEAA, Penicillin, Streptomycin, cell culture dish, 8 mm culture dish	Sigma-Aldrich, Gibco, GBO, IBIDI
Hela knockout	DMEM (4.5 g/l) with 10% FBS, 1% L-glutamine and 1% Pen-strep and 1:20,000 puromycin	Staurosporine, T57, T25 flasks	Sigma-aldrich, Merck, Selleckchem(AM-2282), Sarstedt AG & Co.

B.2 FCS and confocal measurements

FCS measurements were conducted on a Nikon Eclipse TE2000U confocal microscope with a Pico Harp 300 TCSPC module from Pico Quant. A 485 nm pulsed diode laser (Pico Quant LDH-D-C) with a Sepia 11 module from Pico Quant served as the excitation source, while a 488 nm long-pass filter was placed in the detection path. The laser power ranged from 5-10 μW, thereby minimising the photobleaching of GFP molecules during 30-second measurement intervals. Fluorescence of GFP was visualized through a 60x (N.A. 1.2) water-immersion objective, and a single photon avalanche diodes (MPD and PerkinElmer) were used to collect the emission signals for subsequent FCS analysis. All cell-based experiments were performed inside a climate chamber (Okolab) that maintained a stable temperature of 36±0.5°C and a controlled atmosphere with appropriate humidity.

All experiments were preceded with a calibration step to define the confocal volume. For this purpose, Rhodamine 110 (sigma Aldrich) in 2.5% (w/v) glucose in PBS was used, alongside correction collar adjustments. Under these calibration conditions, the dye exhibited a diffusion coefficient of 560 $\mu m^2/s$, which served as the reference for calculating confocal volume dimensions. On average, the short axis (w_z) of the confocal volume was 0.196±0.009 μm, the structure parameter (κ) ranged between 5-6, and the effective volume (v_{eff}) was between 0.95-1.11 (fL). Cell positioning was performed via confocal microscopy, while SymphoTime 64 software (Pico Quant) facilitated the collection of time-trace data and the generation of autocorrelation curves. Fluorescence intensity I(t) was recorded from v_{eff} and the corresponding autocorrelation function was computed for FCS measurements.

Data were obtained from 5-10 cells per experiment, with five 30-second measurements per cell. Details on the cell culture protocol can be found in Appendix B.1. FCS analysis proceeded in 2 stages: (a) calculating the autocorrelation function G(t) from fluorescence intensity and (b) deriving the diffusion coefficient using appropriate models. Each cell's mean diffusion coefficient was determined from 5-10 consecutive measurements. Confocal images were collected on a Nikon A1 system using a 488 nm Melles Griot laser (model 35-IMA-410-019. For starvation experiments, measurements were taken on days 0,1,2,3 and 4, with cells in PBS containing calcium and magnesium ions.

B.3 Isolating plasmid F_0-F_1 ATPase (MALIONR) from *E.coli.*

2 sets of plasmids were isolated using a midi prep kit[154]. MALIONR or the test plasmid (negMALIONR) of size 6549 bp: A red ATP sensor with an insert size of 1100 bp was isolated along with a negMALIONR plasmid as a negative control. The plasmid yield measured using nano drop is shown in Table B2 below.

Table B2: Genetically encoded ATP sensor isolation from *E.coli*

Samples	Fluorescence (λ_{ex}/ λ_{em})	Concentration	$A_{260/280}$	$A_{260/230}$
MALIONR (test)	565/585 nm	1575.4 ng/µl	1.89	2
Neg MALIONR (control)	none	2630 ng/µl	1.9	2.03

B.4 Gel electrophoresis and MalionR transfection in 769-p cells

Restriction digests were prepared by mixing 2 µl of uncut plasmid DNA (1 µg/µl) with 1 µl HindIII, 1 µl ExoR1 or both enzymes (1 µl each) and incubated at 37°C overnight. A 1.5% agarose gel was prepared using 1x TAE buffer, and 1 µl of Sybr Green was added when the gel cooled to 50°C after boiling. The gel was poured into a casting tray with combs and allowed to solidify. After solidification, combs were removed, and samples premixed with 1 µl loading dye were loaded into wells. The gel was run for 30 minutes at 450 A, 230 V and analysed under UV light.

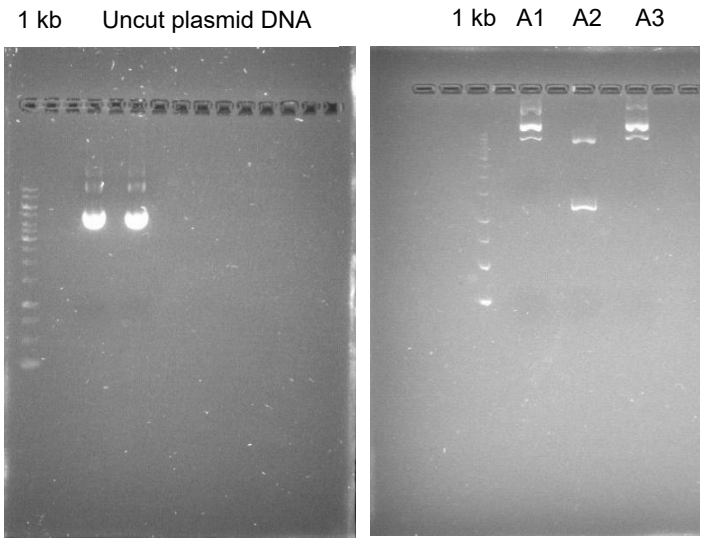

Figure B3: Confirmation of isolated MalionR plasmid from E. coli. The gel picture on the left shows controls: uncut plasmid DNA (both the sensors, MalionR and negMalionR). The gel picture on right - A1 contains only HindIII enzyme, which will not cut; same goes for A3, which contains EcoR1, which won't cut. Therefore, a supercoiled band of plasmid, along with a linearized, plasmid is present. A2 contains both enzymes, making the cuts at desired locations.

Overnight seeded 769-p cells were transfected with the isolated plasmid - MalionR using lipofectamine transfection kit[155]. A and B solutions were mixed in a 1:1 ratio and incubated for 10-15 minutes. 50 µl of the mix was added per well with the plasmid vector. After 5 hours incubation, media was changed and cells were incubated for 48 hours before measurements.

Table B.3: Transfection reagents for introducing ATP sensor in 769-p cells

MIX A	MIX B
Lipofectamine - 1.5 µl	DNA - 1 µg/ µl
P3000 - 2 µl	Opti MEM – 50 µl
Opti MEM - 25 µl	

B.5 CRISPR-CAS9 gene editing for creating cellular knockout

I. Tol2 transfection for creating HeLa GFP cells

8*10^4 cells/ well were plated in duplicates (including control), and a separate set was kept aside for FACS analysis. On days 1 – 3, wells were transfected using standard lipofectamine protocol, keeping one well aside as transfection control (without plasmid). On day 2, media was changed to DMEM containing 1:2000 blastocidine and cells were transferred to a new 6-well plate. Till day 4, the selection was maintained until all control cells died. After one week, surviving cells were analysed using FACS to assess GFP transfection efficiency and sorted into high and low-GFP-expressing cells.

II.Designing gRNAs

- A curated genome-wide library called Brunello (for humans) was used. Four gRNAs per target gene (CLCNKA), yielding the highest fraction of frameshifts, were chosen from the indelphi software website. The four gRNAs were then searched in the library.
- Custom sgRNAs were ordered on the IDT website.
- 59-60 bp gRNA oligos were ordered in the following format: GGAAAGGACGAAACACC (20-21 bp protospacer starting with G—add a G to any 20-bp protospacer without one natively) GTTTAAGAGCTATGCTGGAAAC. Refer to the custom-made gRNA sequence below.
- 04192023_sgCLCNKA_RS GGAAAGGACGAAACACCG ACCTCGGACCACACACCCGA GTTTAAGAGCTATGCTGGAAAC
- The primer selection was done using http://bioinfo.ut.ee/primer3/. Refer to primer length specifications below (in bp).

Min 19, Opt 22, Max 27

Min 59, Opt 62, Max 67

150-250-bp

Q5, Ta = 69, 232bp

III. Molecular Cloning

- **Restriction Digest**
  .1. A master mix was prepared to cut the vector backbone and insert the gRNA.
  .2. For 60 µL of total volume, vector (6000 ng), 1.5 µL each restriction enzyme (RE) (no more than 5% of total volume), and 6 µL Cut smart buffer was added.
  .3. Water was added to make up the remaining volume to 60 µL.
  .4. Incubated at 37°C overnight.
- **PCR Insert**
  .1. Plasmids and primers were thawed on ice.
  .2. For a 50 µL reaction, 25 µL NEBNext Q5 UltraII mastermix, 1.25 µL each primer (final concentration 500 nM), 0.3 µL plasmid (~25 ng DNA/µL), and water were added to the final volume.
  .3. PCR was run using the NEBNext protocol, adjusting cycle number, annealing temperature, and extension time as needed.
- **Gel Purification**
  .1. For gel purification, an official Qiagen protocol was followed[156]
- **NEBuilder/Gibson Assembly**
  .1. For NEBuilder HiFi DNA assembly, New England Biolabs protocol was followed[157].
- **Transformation into Competent Cells**
  .1. Competent *E.coli* cells were thawed on ice.
  .2. 25 µL of competent cells were mixed with 2 µL of NEBuilder product.
  .3. Incubated on ice for 30 minutes, heat shocked at 42°C for 30 seconds, then placed on ice for 5 minutes.
  .4. 200 µL recovery media was added and incubated at 37°C for 30 minutes.
- **Plating E. coli**
  .1. *E.coli* liquid culture on pre-warmed Ampicillin-resistant plates using plating beads.
  .2. Incubate at the appropriate temperature (30°C for NEB Stable cells, 37°C for NEB10beta cells).
- **Colony Picking and Overnight Culture**
  .1. Round bottom tubes were labelled.
  .2. Distinct colonies were picked into tubes with 4 mL LB + Ampicillin.
  .3. Incubated at 21°C in a shaker.
- **Mini/Maxi Prep**
  .1. For plasmid isolation using mini/midi prep , the Qiagen protocol was followed[158].
- **Test Digest**
  .1. Master mix was prepared with restriction enzymes, Cut smart buffer, and vector DNA.

.2. Incubated at 37°C for 1 hour.

.3. A gel was run to verify fragment sizes.

- **Sanger Sequencing**

.1. Samples were prepared with 5 µL of 5 µM primer and 8 µL plasmid (100-200 ng/µL).

.2. Samples were sent to Eton Bioscience for sequencing.

Once the plasmid was made, a restriction digest was set up to isolate the segment containing the inserted gRNA. This segment of DNA was amplified using PCR, and the PCR product was further sent for Sanger sequencing to confirm the presence of gRNA in the plasmid. Post sequence confirmation, the plasmid was used to perform lentiviral transductions in HeLa cells. HeLa cells were taken from the cell bank and transfected with a GFP reporter before transductions. These transfected cells were then sorted into a high and low GFP expression using flow cytometry. Low GFP-expressing HeLa cells were then transduced with the plasmid containing the gRNA. Post transduction, cells were selected for gRNA expression by culturing them in the selection marker – puromycin (1:20,000). Bulk gDNA isolation was performed and sent for Sanger sequencing to confirm indel/mutations created by the introduction of gRNA into the HeLa cell genome. Sanger sequencing showed no deletion/insertion from the PCR products obtained from bulk genomic DNA isolation after transductions. Single cells were sorted into 96 well plates to select cells with mutations. Single-cell clones were cultured in DMEM media containing the selection marker until the colonies formed. HeLa cells divide every 36 hours – thus, it took 2 weeks for single clones to form colonies. gDNA isolation was performed on 200 clones from 2 different 96 well plates. After Sanger sequencing the bulk genomic DNA, the spectrum analysis revealed the presence of 1/4th knockout clones.

Four of the 1/4th knockout clones were selected from the restriction digest assay and sent forward for further confirmation in Sanger sequencing. Referring to the Sanger sequencing results in Fig B4, the bottom panel sequence is from the control cells, and the top panel consists of sequences from the knockout clones. The indels are highlighted in the red boxes around the single base pair in the gRNA_CLC region of the construct in the top panel, depicting the mutations created in the target region. After confirming the clone sequencing through Sanger sequencing for the 2 clones mentioned above, NGS was also performed for final confirmation.

Figure B4: Sanger sequencing from the G4 clones (positive clone with indels), confirming the presence of indel formation downstream PAM sequence in the gRNA_CLC region. The red boxes show the incorrect base pair or an indel inserted due to CRISPR editing.

PCR products from three clones were taken forward for NSG prep and analysed using the Agilent bioanalyzer system. The gel image represents the samples along with the controls. The ladder l in lane A1, serves as a reference for fragment sizes. Lane C1, D1 and E1 correspond to clones A8, B2, and G4. All the clones show a conc peak obtained between 200-300 bp, confirming the presence of a knockout. The conc of DNA obtained for clone G4 was 8.94 ng/µl.

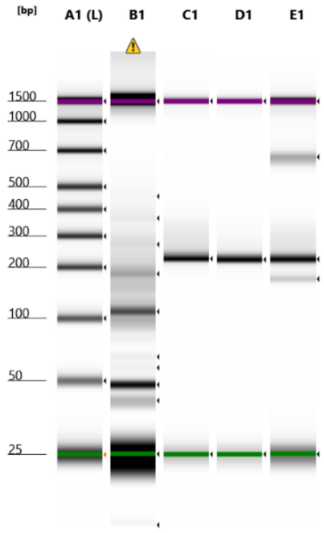

Figure B5: Gel contains 3 clones chosen from sanger sequencing to confirm the presence of the gRNA band from the genomic DNA of HeLa GFP cells. Lane C1, D1 and E1 corresponds to clones A8, B2, G4.

B.6 Bisantrene-ATP concentrations in TCSPC experimental set up

Table B4: Experimental design summary for bisantrene experiments

Parameters	Value
Stock Concentration of Bisantrene	25 mg
Buffer Types	TRIS (90:10), PBS, Water
Form of Bisantrene Used	Dihydrochloride salt (10 mg stock)
Molecular Weight of Bisantrene Dihydrochloride	471.39 g/mol
Solubility of Bisantrene	8 mg/mL
Molecules in 0.2 mg of Bisantrene	2.93×10^{17} molecules
Molecular Weight of ATP	507.18 g/mol
ATP Stock Concentration	100 mM
Estimated ATP in HEK Cells (Volume ~ 4000 cm^3)	3×10^{10} molecules
Bisantrene and ATP Mixture Volume	1 µL Bisantrene + 1 µL ATP in 200 µL of buffer
Experimental Conditions	Bisantrene + TRIS+ ATP, Bisantrene + PBS + ATP, Bisantrene + TRIS+ cells, bisantrene + PBS

B.7 HPLC experimental set up

Methanol with ammonium acetate buffer (pH 6.8 -7) was used. Columns of 3 µm with higher S.A. or lower silica gel were used as stationary phase. These columns are used to increase the efficiency of the process, reducing the need to use a lot of solvents. 2 solvents, A (10%) and B (90%), were used. The temperature of the columns was set at 35°C. This is usually set at higher than room temperature to increase the resolutions of the peaks obtained. The solvent was flown from bottom to top to remove the air bubbles. Samples were transferred to the transfer vials, and the experiment was performed.

Table B5 : Samples and standards for HPLC analysis

Parameters	Values
Samples for HPLC analysis	PBS collected from cells after treatment with 100 µM STS
Standards for HPLC analysis	FAD in PBS buffer (19 M), STS in DMSO (12 mM)
Experimental duration and condition	37°C for 2 hours
λ_{ex} of laser	488 nm

B.8 FLIM experimental set up for data acquisition

Table B6: Experimental set up for FLIM image acquisition

Parameters	Values
Pixel dwell time	57.2 µs
Number of frames/measurement	10
Per measurement duration	30 sec
Pinhole size	1.2 AU (26.8 µm)
Laser power	6 µW